Ion Diagnostics for Extreme Ultraviolet Nanolithography

Ph.D. thesis, Vrije Universiteit Amsterdam, 2023
Ion diagnostics for extreme ultraviolet nanolithography
Lucas Poirier

ISBN 978-94-6483-312-6
An electronic version of this dissertation is available at: research.vu.nl

VRIJE UNIVERSITEIT

Ion Diagnostics for Extreme Ultraviolet Nanolithography

ACADEMISCH PROEFSCHRIFT

ter verkrijging van de graad van Doctor of Philosophy
aan de Vrije Universiteit Amsterdam,
op gezag van de rector magnificus
prof.dr. J. J. G. Geurts,
in het openbaar te verdedigen
ten overstaan van de promotiecommissie
van de Faculteit der Bètawetenschappen
op vrijdag 6 oktober 2023 om 13.45 uur
in een bijeenkomst van de universiteit,
De Boelelaan 1105

door

Lucas Raphaël Poirier

geboren te Parijs, Frankrijk

promotoren:	dr. O.O. Versolato prof.dr.ir. R. Hoekstra
copromotor:	dr. J. Sheil
promotiecomissie	prof.dr. H.L. Bethlem prof.dr. E. Sokell prof.dr. N. Lopes Cardozo dr. J. Beckers dr. S. Brussaard

The work described in this thesis was carried out at the Advanced Research Center for Nanolithography (ARCNL), a public-private partnership between the University of Amsterdam (UvA), the Vrije Universiteit Amsterdam (VU), the University of Groningen (RUG), the Netherlands Organisation for Scientific Research (NWO), and the semiconductor equipment manufacturer ASML.

contents

introduction

Lithography

The process of inscribing patterns and characters onto substrates is intimately connected to the ability to communicate ideas and to tell stories — from prehistoric rock and bone carving, to state-of-the-art silicon-based electronics.

This connection is best exemplified by the late 15th-century invention of the printing press by goldsmith Johannes Gutenberg in Germany. The improvement in quality and quantity of communication imparted by the printing press allowed for the rapid spread of ideas starting in the late 15th, early 16th centuries. The newborn technology assisted the escalation of religious and societal turmoil after the famous incident of 1517, when Augustine monk Martin Luther vehemently opposed 95 theological stances held by the Catholic church.

Countless pamphlets (*Flugschriften*) and artworks (*e.g.*, woodcuts, see Fig. 1) supporting the reformed ideas of Luther were produced by the detractors of the Catholic Church. The pamphlets were printed and distributed throughout the Holy Roman Empire; they contributed to the great popularity of the Reformation in the Empire. Such a pamphlet is shown in figure 1; the pamphlet depicts the pope Adrian VI being carried into flames by chimerical demons, where a few individuals — namely a monk-like figure — are being consumed by the inferno. Such representations, loaded with symbolism, turned out to be a very effective means of propaganda; the larger part of the intended audience could not read nor write but

Figure 1: "Descent of the pope into hell" (woodcut print), Lucas Chranach the Elder, printed in the *Passional of Christ and Antichrist*, written by P. Melanchthon and J. Schwertfeger, in Wittenberg in 1521. Pamphlet distributed in the Holy Roman Empire as propaganda against the papacy (see Ref. [1] for more detail on the woodcut and on the Passional).

could certainly recognize the pope, bearing his tiara and chasuble. By the end of the 16th century, new ideological and political aspirations had transformed a large part of central Europe thanks to the rapid development of the printing press.

A parallel can be drawn with the late 20th century Digital Age revolution, which also brought about profound societal and lifestyle transformations. This new technological paradigm was instigated by developments in photolithography — the process of carving microelectronic components from silicon, using light as a chisel — which enabled the progress of microelectronics, with the invention of the transistor in 1947. From the multitude of free, instantaneous, and user-friendly communication channels, to the explosion of social media and hand-held electronic devices, silicon-based lithography has set its ubiquitous footprint on the modern world.

EUV nanolithography

In a manner of speaking, nanolithography is the modern-day counterpart of the printing press. In essence, light is used to carve integrated circuits (ICs) with nanometer precision on high-purity silicon substrates. Integrated circuits are the building blocks of modern electronics. Further development and optimization in nanolithography are extremely expensive and technologically demanding, and access to the technology even plays a major role in worldwide diplomatic relations.

The wavelength of the light used for patterning determines the smallest achievable feature size, known as the critical dimension (CD): CD $\propto \lambda/\mathrm{NA}$, where λ is the wavelength of the light used for patterning and NA is the numerical aperture of the optical system used to transport the light to the silicon substrate. CD is currently smaller than 7 nm. The ever-growing hunger for faster and smaller electronics motivates the search for light sources with ever-smaller wavelengths. State-of-the-art integrated chips include on the order of one hundred billion transistors. For more than two decades, the industry has been developing EUV nanolithography machines that rely on tin laser-produced plasmas (LPP) for producing very short, 13.5 nm EUV light. In an LPP light source, a laser is used to rapidly heat up a liquid tin target. The target material is transformed into a plasma made up of positively charged ions and negatively charged electrons. The ions are electronically excited primarily by the impact of plasma electrons. In turn, they release the excitation energy by emitting light on a broad wavelength spectrum. Many parameters can be tuned to change the characteristics of the EUV-producing plasma: drive laser pulse wavelength and intensity, multi-laser pulse schemes, target volume, *etc*. The nanolithography research community is very dynamic and puts great effort into developing formulas for efficient EUV production and roadmaps for the future of nanolithography. A standard metric is employed in the industry to characterize the efficiency of the conversion of laser light to in-band EUV: CE $= E_{\mathrm{in-band}}/E_{\mathrm{L}}$, where E_{L} is the total drive laser pulse energy, and $E_{\mathrm{in-band}}$ the so-called "in-band" energy carried by all photons with wavelength comprised in a $13.5 \pm 1\%$ nm bandwidth. Only the in-band light emitted towards a large parabolic 2π sr collector multi-layer mirror (MLM) is used in the inscribing process further down the line. The rest of the emitted spectrum, the so-called "out-of-band" light, is discarded.

Both the wavelength of the light and the efficiency associated with its generation are of great importance for further developments in nanolithographic technology. Aside from the production of EUV light in the EUV source and its transport to the silicon wafer using multi-layer mirrors, other challenges are to be addressed by the nanolithography research community. Notably, the cleanliness and long-term fidelity of the EUV source are jeopardized by the emission of energetic ions from the tin plasma.

Ion emission from laser-produced plasma

Tin laser-produced plasmas can produce EUV radiation with great efficiency (above 5% CE for current state-of-the-art EUV sources, using a 10 μm CO_2 laser light for driving the LPP). However, producing hot and dense plasma comes at the cost of generating particles with high kinetic energy and charge. Typically, tin ions can reach velocities up to 10^4 or 10^5 m/s; particles flying around a nanolithography machine source vessel at such speeds are detrimental to the lithographic process. Sputtering and implantation are the main vectors of lifetime reduction of EUV optics, namely the MLMs that carry the EUV light from the source to the wafer, and with it the source performance. EUV source performance is contingent on the preservation of the finely tuned optical properties of the collector mirror. Relevant to the sputtering and implantation processes are the energy, the ionic charge state, and the spatial dependence of the ion emission. These properties determine the nature of the possible damage they may cause. It is therefore crucial to identify the main experimental parameters that determine the ion spectra. In industrial EUV sources, different strategies are used to alleviate the damage caused by ions and neutrals. One strategy relies on a buffer gas flow around the tin LPP to reduce the kinetic energy carried by the drifting particles, in a process called stopping. Other strategies used in the industry involve magnetic deflection of the ion flow. Designing schemes through which damages are minimized requires a comprehensive understanding of particle emission.

In this Thesis, we aim to answer open questions related to ion emission in EUV sources, and its significance for the optimization of light source performance:

> *What physical processes and what experimental parameters give structure to the kinetic energy and charge state distributions of the emitted ions?*
> *Corollary to this question, how can the ion emission be tailored for optimal EUV source performance and long-term fidelity?*

Ion detection and characterization is no easy task, involving careful calibration of the detectors to elucidate the measured signals. Besides, complementary analytical and numerical studies are challenging both numerically and on the fundamental level. Ion emission from tin LPP constitutes a challenge for EUV source manufacturers and for plasma physicists.

Experimental investigation

At the Advanced Research Center for Nanolithography (ARCNL), EUV source physics is investigated experimentally, and in complementary ways. A complete diagnostic toolkit is

employed to characterize the plasma. In-band and out-of-band light are measured using photodiodes and spectrometers. Liquid tin deformation upon laser impact is also studied, with the goal of designing the optimal target pre-formation scheme for EUV production. Lastly, tin ions emitted from the plasma are carefully investigated. This Thesis focuses on ionic emission, which is shown in this Thesis to carry the dominant fraction of mass, momentum, and kinetic energy over the emission of neutral tin atoms.

It is very challenging to detect ions directly in the plasma; instead, they are detected far (around 1 m) from the plasma. Ion trajectories are assumed to be radial and ballistic. Knowing the distance between the LPP and a detector, the velocity (and kinetic energy) of ions can be conveniently derived from their measured several 10 microseconds-long time of flight TOF (that is, the duration of their flight from the plasma to the detector). In addition, ions with different charge state react differently to electrostatic fields; this principle is utilized to resolve ion charge.

At ARCNL, we use various types of detectors: (i) Faraday cups (FCs), which detect ion currents, integrating all different ion charge states, and therefore losing information on charge state distribution; (ii) an electrostatic analyzer (ESA), which detects ions and is able to resolve the charge of detected ions; and (iii) retarding field analyzers (RFAs), which are modified FCs, also able to resolve ion charge. A significant portion of the work presented in this Thesis tackles the meticulous calibration of the detectors used at ARCNL. We next apply the calibration and methods developed to experimentally study the angular and charge-state resolved ion kinetic energy distributions under a broad range of EUV source conditions in the experimental setups at ARCNL.

Analytical and numerical investigation

Analytical solutions to the problem of the expanding plasma give important insight into the ion kinetics. However, such solutions are typically only available for strongly simplified representations of the entire physical problem given the interaction of many complex physical processes. Important contributions to this topic include those of Murakami [2] and Mora [3] building on earlier work of Zel'dovich [4] and many others.

Numerical calculations constitute the main tool for making accurate, fully quantitative predictions. A standard approach to modelling plasma and its expansion is the particle-in-cell method, which can treat individual interactions at the single or aggregate particle level. At high density, where collisions are very frequent, the standard approach involves modelling the collective behavior of the plasma, in effect treating it as a radiating fluid – this so-called *radiation hydrodynamics* approach is crucial for ensuring computational tractability. Radiation hydrodynamics modelling to date has primarily been used to understand the radiative properties of the hot and dense plasma, but not for studying the plasma expansion. In

this Thesis we demonstrate that the single-fluid hydrodynamic approach to plasma expansion accurately reproduces the experimental observations of the ion kinetic energy distributions.

Thesis outline and summary

Chapter 1 presents the cross-calibration of an electrostatic analyzer for the diagnosis of LPP ions with a charge-integrated Faraday cup detector. The electrostatic energy analyzer and the channeltron detector are thoroughly calibrated. The effect of counting-mode count rate saturation is also taken into account. Charge-resolved and charge-integrated ion spectra are presented for a tin droplet LPP experiment.

In **Chapter 2**, we compare ion energy distributions obtained with our electrostatic analyzer with those obtained using the 2D radiation hydrodynamic code RALEF-2D. A single observation angle of 60° is considered. The numerical code manages to reproduce the relevant spectral features, namely a prominent peak feature observed at high-energy (about 2 keV). The origin of the peak is unraveled through the inspection of density and velocity lineouts captured along the 60° direction. The peak is attributed to the formation of a high-speed density shell. This shell forms due to the high-speed material plowing into slower material.

Chapter 3 presents the absolute calibration of a retarding field analyzer. The operating principle of the instrument, namely the retarding field method, is described as well as the so-called "bottom-up" post-processing scheme. Charge-resolved and charge-integrated spectra are produced and are found to be in good agreement with previous observations. The energy resolution of the device is also obtained from the recorded data.

Chapter 4 builds on the preceding RFA calibration by investigating charge-integrated ion emission from tin droplet LPPs at seven different angles around the plasma. A prominent peak in charge-integrated ion energy spectra is observed most prominently in the frontward direction (opposite of the direction of laser propagation). A more complete description of the high-energy expansion front is presented, highlighting the strong angular dependence of the expansion front. RALEF-2D simulations provide insight into the anisotropy of the ion emission: the expansion is produced upon absorption of the laser pulse peak intensity by the front side of the plasma, while the back side of the plasma remains colder and denser, despite some hot material flow from the front to the back of the plasma.

Chapter 5 investigates the scaling of LPP ion emission properties with laser pulse intensity (in the range of $0.4 - 40 \times 10^{10}$ W/cm^2) by studying individual charge states 1+ to 8+. At

small angles with respect to the direction of the incoming laser pulse, high-energy bunching is observed in ion energy spectra of high charge states (charge above $+4e$), giving a double-peak structure to the spectra. For a given observation angle, ions bunch up at the same energy: we link this bunching phenomenon with the high-energy bunching observed in charge-integrated spectra that was associated with a fast, forward-facing expansion front (*cf.* Chapter 4). We report a power-law dependence of the positions of the two peaks with varying laser intensity; this empirical dependence is in line with expectations from analytical considerations. Surprisingly, we find isotropic scaling of spectral feature positions with laser intensity, whereas the ion energy spectra themselves exhibit strong anisotropy. Lastly, we also report a universal power-law scaling of the average energy-dependent charge state $\overline{z}(E)$.

Chapter 6 explores the use of buffer hydrogen gas for ion damage mitigation in EUV sources. Specifically, the effect of charge exchange between tin ions and hydrogen gas is studied experimentally using an RFA. At low hydrogen pressures (10^{-6} – 10^{-4} mbar), ion energy spectra show a rapid decrease in overall charge, while the total number and energy of ions are mostly conserved. At higher pressures, the number of ions slowly decreases, with all ions eventually becoming either singly or doubly ionized. Interestingly, the electron capture from the buffer gas by Sn^{2+} ions to produce Sn^{+} is endothermic, if considering only the electronic ground states of the ions. However, we observe a significant number of 1+ ions produced at intermediate hydrogen gas pressure. To explain the production of Sn^{+} ions, we propose that their generation is due to electron capture by metastable $Sn^{\mathbf{2+*}}$ ions. Our proposal is supported by model simulations using atomic collision cross sections to track the charge states of Sn ions while traversing the $H_{\mathbf{2}}$ buffer gas.

In the **Conclusion**, we summarize the key findings of this Thesis and present an outlook for future measurements. We expand our studies on the universal scaling of the energy-dependent average charge state $\overline{z}(E)$ and apply it to accurately predict the propulsion speed of pre-deformed droplets directly from charge-integrated Faraday Cup data and provide further examples of the universality of the scaling relation.

chapter 1

Absolute cross-calibration of a combined electrostatic and time-of-flight analyzer for energy- and charge-state-resolved spectrometry of tin laser-produced plasma

Lucas Poirier, Alex Bayerle, Adam Lassise, Francesco Torretti, Ruben Schupp, Lars Behnke, Yahia Mostafa, Wim Ubachs, Oscar O. Versolato, and Ronnie Hoekstra
Applied Physics B **128**(39), 1432-0649 (2022).

We present the results of the calibration of a channeltron-based electrostatic analyzer operating in time-of-flight mode (ESA-ToF) using tin ions resulting from laser-produced plasma, over a wide range of charge states and energies. Specifically, the channeltron electron multiplier detection efficiency and the spectrometer resolution are calibrated, and count rate effects are characterized. With the obtained overall response function, the ESA-ToF is shown to accurately reproduce charge-integrated measurements separately and simultaneously obtained from a Faraday cup (FC), up to a constant factor the finding of which enables absolute cross-calibration of the ESA-ToF using the FC as an absolute benchmark. Absolute charge-state-resolved ion energy distributions are obtained from ns-pulse Nd:YAG-laser-produced microdroplet tin plasmas in a setting relevant for state-of-the-art extreme ultraviolet nanolithography.

1.1 Introduction

Laser-produced plasma (LPP) has found its way to a variety of applications in science and technology ranging from laser-induced breakdown spectroscopy [5] and plasma accelerators [6], to sources of extreme-ultraviolet (EUV) light for nanolithography [7]. Sources of EUV light rely on the efficient production of highly-charged ions in the hot ($\sim 100\,\mathrm{eV}$) and dense ($\sim 10^{19-21}\,\mathrm{e^-/cm^3}$) plasma generated by pulsed laser light with intensities spanning from 10^9 to $10^{11}\,\mathrm{W/cm^2}$ [8]. For nanolithographic tools the wavelength of choice is 13.5 nm, as for that EUV wavelength multilayer optics exist [9, 10]. For LPP based generation of 13.5 nm EUV light the species of choice is Sn, for which, due to its particular electronic structure [11], a wide range of charge states (9+ to 15+) emit in a narrow band around 13.5 nm. Besides the desired EUV light, the violently expanding Sn plasma generates ionic "debris" that may affect the lifetime of the light-collecting multilayer optics by, *e.g.*, coating, implantation or sputtering depending on the energy and charge state of the ions coming from the plasma. Measurements of the energy and charge state distributions of Sn ions coming from the LPP also give access to the expansion dynamics of the plasma itself [12–14]. Moreover, accurate data on the energy distributions facilitate the determination of the fraction of the total energy that is carried by the plasma ions [15].

A whole arsenal of techniques and instrumentation [12, 16–21] has been used to gather information on the ions coming from an LPP plasma. Ion charge-energy spectra from tin LPP have been obtained using electrostatic probes [22], Faraday cups (FCs) without [13, 14] or with retarding fields applied (RFA) [18, 19], electrostatic analyzers (ESA) [20, 21, 23, 24], or Thomson Parabolas (TP) [12]. The simplest measurement tool is the FC with which one can measure the plasma ion current. In combination with time-of-flight (ToF) measurements which become possible for pulsed operation of the LPP source, one obtains access to the energy of the ions. Placing retarding field grids in front of the FC turns the FC into an RFA, though unraveling charge state and energy is challenging. For high-resolution energy measurements, electrostatic analyzers (ESA) are optimal. However, since ESA spectrometers resolve on energy-over-charge-state (equal E/z values are transmitted), charge-state-dependent energy spectra require the incorporation of ToF techniques. The absolute detection efficiency calibration of the whole system is complicated, in particular for low-energy heavy ions such as Sn ions, since detection efficiencies of channeltron electron multipliers (CEM) or microchannel plates (MCP) are very low at energies below about 2 keV and are strongly dependent on ion energy [25, 26].

In this work, we detail the absolute calibration of the ARCNL ESA operated in a combined energy and ToF mode to extract the kinetic energy distributions for the different charge states of Sn ions coming from a Sn LPP EUV source. Typically the Sn ions coming from the plasma are in charge states of 1+ to 8+ and have energies ranging up to several keV. After

the description of the experimental setup, the following three aspects of the operation and calibration of our ESA-ToF spectrometer will be discussed in greater detail: i - particle detection and counting procedures; ii - the resolution of the ESA; iii - the detection efficiency of the channeltron used for ion counting. These topics lay the basis of the energy-dependent calibration of the ESA-ToF system. Finally the independent calibration of the system will be compared to the result of a FC measurement. By means of this cross-calibration relative to the FC, the absolute calibration of the ESA-ToF analyzer is achieved. This calibration is conducted on a microdroplet tin plasma driven by a 1-μm wavelength ns-pulsed laser under conditions relevant for producing EUV light.

1.2 Experimental setup and methods

1.2.1 Laser-produced plasma

Our LPP EUV source and auxiliary equipment has been described in detail before [27]. The components most relevant to this work are briefly recalled here, see also figure 1.1. A tin reservoir is mounted on top of a vacuum chamber (10^{-7} mbar) and is kept at a constant temperature of 260 °C. From the reservoir, a nozzle produces a 31.5 kHz droplet train of pure, molten tin droplets traveling along the vertical axis of the vacuum chamber. The microdroplets, which have a diameter of 28 μm, first traverse a horizontal light sheet produced from a helium-neon laser. The light scattered off of the Sn droplets is detected by a photo-multiplier tube. The detected signal is frequency down-converted to 10 Hz to enable triggering of the laser system that creates the plasma. This Nd:YAG laser system produces pulses at 1064 nm wavelength of 10 ns time duration at full-width at half-maximum (FWHM). The beam is focused to a Gaussian spot (63 μm FWHM) onto the droplets in the center of the chamber. By using a half-wave plate and a thin-film polarizer, the laser pulse energy can be adjusted without affecting the spatial beam profile. In the following, the laser pulse energy was set to 112 mJ unless otherwise specified.

1.2.2 The ESA-ToF energy analyzer

After a 1.12-m flight path from the LPP, ions originating from the plasma enter the ESA through an input aperture A_{in} with a diameter of about 60 μm. The ESA is positioned at an angle of 60° with respect to the incoming laser beam, in mirror symmetry with a FC. The radii of the inner and outer deflection electrodes of the ESA are respectively $r_1 = 190$ mm and $r_2 = 210$ mm. Symmetrical bias voltages of $\pm U_{ESA}/2$ generate a radial electric field which forces positively charged ions of a specific energy-over-charge ratio onto a circular trajectory in between the cylindrical electrodes (85° in arclength). Thereafter selected ions

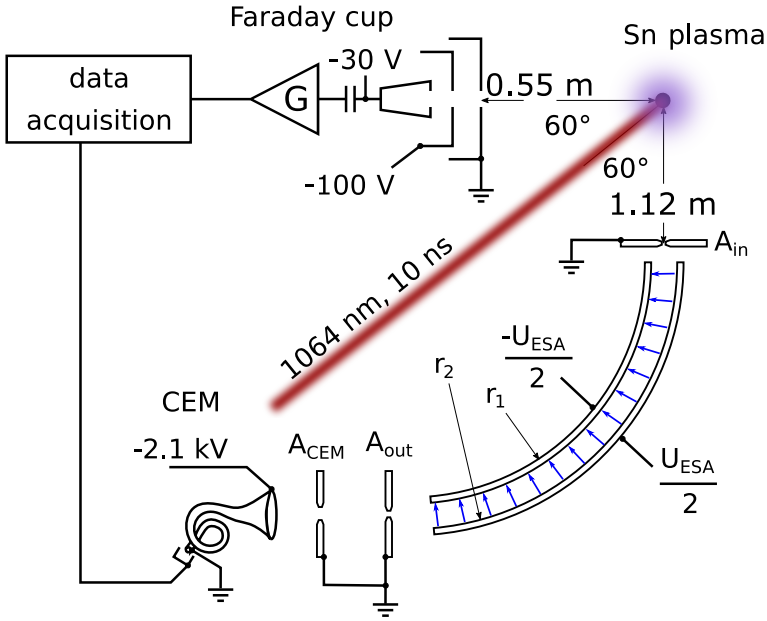

Figure 1.1: Diagnosing ion emission from Nd:YAG-produced plasma: an amplified (G), biased Faraday cup (FC) and the electrostatic analyzer (ESA-ToF) are positioned at the same angle with respect to the Nd:YAG beam direction (see main text).

pass through two grounded apertures A_{out} (inner diameter 2.5 mm) and A_{CEM} (inner diameter 3.4 mm), which are 5.5 mm apart. Because A_{in} is much smaller than A_{out}, the geometrical transmission of the ESA is close to unity as long as space-charge-driven beam expansion is not significant. The output apertures shield the electric fields from the ESA plates from the field of the channeltron electron multiplier detector and vice versa. This allows for changing the voltages on the CEM without affecting the ESA, which is important to determine the detection efficiency of the CEM for Sn ions of different energy and charge state (see below).

The pass energy E_0, the energy at which ions in charge state z can traverse the ESA without being intercepted, is related to the voltage difference between the electrodes U_{ESA} via [28]

$$\frac{E_0}{z} = \frac{e\,U_{ESA}}{2\ln(r_2/r_1)}, \tag{1.1}$$

where e is the elementary charge. For our ESA, E_0/z [in eV] is $5.0 \times U_{ESA}$, with U_{ESA} in V. The ESA filters ions by their energy-to-charge ratio, consequently 1 keV Sn^+ ions cannot be distinguished from 2 keV Sn^{2+} ions, 3 keV Sn^{3+} ions, and so on. For ions with the same

energy-over-charge ratio, the higher charged ions have higher energy and thus have a shorter ToF from LPP to ESA. Therefore, by measuring the ToF of the ions passing through the ESA, one can resolve the ions of different charge states. A 600-MHz Keysight Infiniium oscilloscope with an input impedance of 50 Ω is used to record the time of their individual arrival.

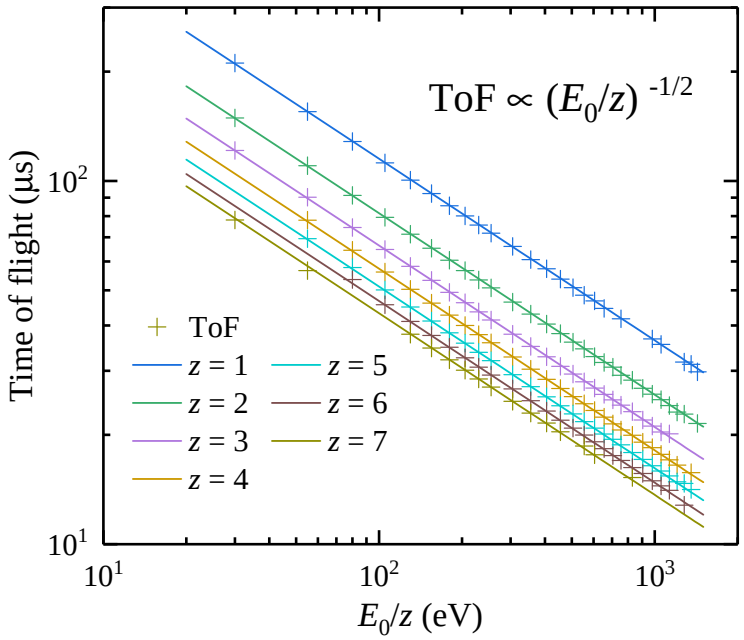

Figure 1.2: Measured average time of flight of Sn^{z+} ions in charge states of $z = 1 - 7$ (colored crosses) for 30 values of the z-scaled pass energy, E_0/z. The lines represent fits to the data with the flight path L as a common fit parameter. The fit yields an ion path $L = 1.470(2)$ m.

To obtain a charge-state-resolved ion energy spectrum, the pass energy E_0 of the ESA is scanned over the interval of interest by changing the voltage U_{ESA}. For each U_{ESA} value, ToF detector traces are typically acquired for 200 laser shots. Each ToF trace shows distinct current transients grouped in several ToF intervals. The center-of-mass of such a charge state cluster arrives at a ToF given by $t = L\sqrt{M/2E_0}$, with L being the total distance between LPP and the CEM detector and M the average mass of the Sn particles. Sn has 10 stable isotopes with natural abundances of a couple of percent or more. The most abundant isotopes are ^{118}Sn (24.2%) and ^{120}Sn (32.6%), see table 1.1. The average mass of Sn based on its natural abundances is 118.71 amu.

Table 1.1: Masses and natural abundances of stable Sn isotopes.

isotope	mass (amu)	abundance ($\times 10^{-3}$)
112	111.9	9.7
114	113.9	6.6
115	114.9	3.4
116	115.9	145.4
117	116.9	76.8
118	117.9	242.2
119	118.9	85.9
120	119.9	325.8
122	121.9	46.3
124	123.9	57.9

Using this average mass of Sn, figure 1.2 shows the ToF of ion bunches for different pass energies and charge states. In the figure, the lines are $L\sqrt{M/2E_0}$ fits, with L as a global fit parameter. The fits yield a common L value of 1.470(2) m, which is is in close agreement with the actual measured distance of 1.476 m. The fact that for all energies and charge states the data are almost perfectly fitted indicates that effects of stray electric and magnetic fields can be neglected, since they would affect different charges and energies differently.

The charge state resolution is limited by the width of the isotope distribution. For Sn^{z+} with the same pass energy [Eq. (1.1)], at a specific charge state z_{max} the lightest isotopes of that charge state have the same ToF as the heaviest isotopes with charge $z_{max}+1$. The isotope distributions of adjacent charge states start to overlap. For Sn ions this happens in our analyzer at 9+.

The individual ToF traces are post-processed via software for an optimal registration of particle counts. Corrections for count rate or dead time effects can subsequently be applied (see below). After sectioning the ToF traces into different charge state clusters, an algorithm looks for individual transients with amplitudes larger than a given threshold, separated by a minimal time τ set by the dead time of the channeltron. In case of high count rates, a correction factor for pile-up effects η_{CR} is determined by considering the yields of the Sn isotopes separately, see section 1.3.1.

After the count rate corrections, two more instrumental correction factors need to be considered for the conversion of the numbers of detected ions per each charge per pass energy into a charge-state-dependent energy distribution, $dN_z(E)/dE$. Namely, those corrections are the pass-energy-dependent energy-bin width $\Delta E\,(E)$, and the energy- and charge-state-dependent detection efficiency η_{det}.

Our type of ESA operates in a fixed $\Delta E\,(E)\,/E$ mode [28], implying that the energy interval within which ions can pass the ESA increases linearly with pass energy. Based on its

mechanical properties one expects a $\Delta E\,(E)\,/\,E$ ratio close to 1% following Ref. [28].

In section 1.3.3 the energy- and charge-state-dependent detection efficiency η_{det} of the channeltron (a gridded Photonis 4502 extended dynamic range channeltron) mounted to the ESA-ToF system is determined. The impact energy (E_{imp}) of the Sn ions impinging on the channeltron determines the detection efficiency η_{det} and is equal to $(E_0 + zU_{\mathrm{head}})$ with E_0 the pass energy of a Sn^{z+} ion and U_{head} the voltage on the head of the channeltron. By scanning the voltage on the head of the channeltron while keeping the pass energy fixed, the energy dependence of η_{det} is established. For a complete mapping of the dependence of the detection efficiency on charge state and energy, the procedure is repeated for a series of pass energies and charge states.

Finally, to assess the overall calibration of our ESA-ToF analyzer, a cross-calibration with Faraday cup data is conducted. This requires the solid angle $\Delta\Omega$ of the ESA-ToF to also be taken into account. The comparison with the charge-integrated FC data is carried out by summing the contributions from different charge-state-dependent ion energy distributions $d^2N_z(E)/dEd\Omega$:

$$\frac{d^2Q}{dEd\Omega} = \sum_z ez\frac{d^2N_z}{dEd\Omega} \approx \sum_z \frac{ezN_z^{\mathrm{m}}(E)}{\eta_{\mathrm{CR}}\,\eta_{\mathrm{det}}\,\Delta E\,(E)\,\Delta\Omega}, \tag{1.2}$$

with the last equality true up to a common prefactor of order unity value, related to the definition of the resolving power ΔE (see section 1.3.2). $N_z^{\mathrm{m}}(E)$, the single-shot measured number of ions with energy in the interval $E \pm (\Delta E(E)/2)$, is corrected by η_{CR} and η_{det}. Converting these distributions [Eq. (2.3)] into an integral ion current enables a straightforward comparison to the FC measurements.

1.2.3 Faraday cup

At an angle of 60° with respect to the incoming laser beam (see figure 1.1), a Faraday cup is mounted onto the LPP chamber to ensure comparability with the ESA-ToF measurements. The FC (FC-73 of Kimball Physics) with an entrance aperture diameter of 5 mm collects charge-integrated ion current at a distance of 55 cm from the LPP. The FC consists of a grounded shield, a suppressor grid negatively biased at −100 V, and a collector cup biased at -30 V (refer to the sketch of figure 1.1). The negative bias on the suppressor grid and cup blocks electrons emanating from the plasma, and suppresses the escape of secondary electrons from the cup.

For its potential use as a Retarding Field Analyzer, the FC contains four grids, each with a given optical transmission of 80% per grid reducing the overall transmission to 41%. The signal measured by the FC-73 was compared to that measured by an open (grid-less), in-house

built FC, placed at the same angle with respect to the laser direction. Figure 1.3 shows the two ToF traces, corrected to account for small differences in distance to the plasma and for detection solid angle. For both FCs, the signal was not amplified but instead measured across a 10 kΩ shunt resistor. The two measured ion currents are in very good agreement. The remaining small difference at $t = 0$ ns is indicative of the fact that the gridded FC provides for better suppression. In the subsequent comparison with electrostatic analyzer data, the signal of the gridded FC (FC-73 of Kimball Physics) is used, corrected for the here validated 41% transmission factor.

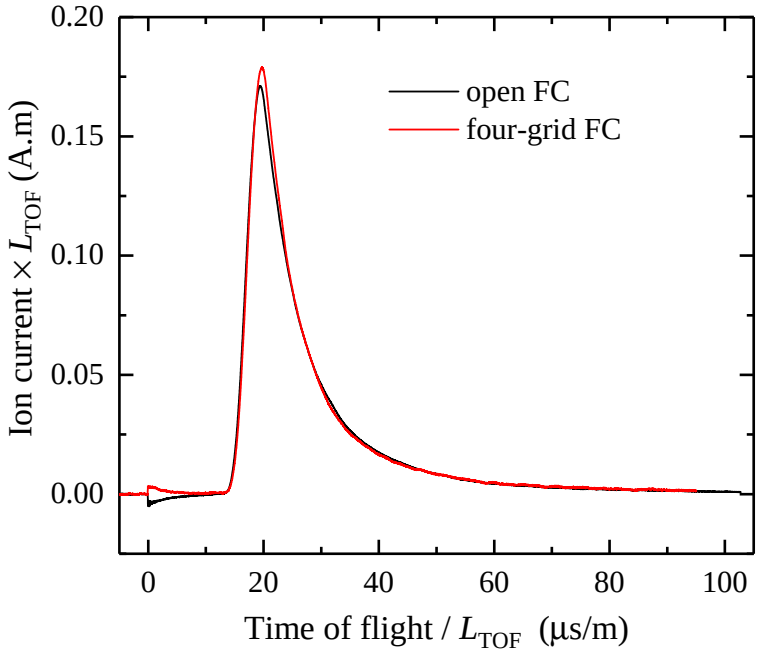

Figure 1.3: Examples of ion currents as measured by the grid-less, open FC (black line) and by the four-grid FC (red line) corrected for a transmission of 41%. Signals were not amplified. The time of flight and the ion current axes are corrected for the slight difference in distance to the plasma (here 0.62 m for the open FC and 0.67 m for the gridded FC).

In the following measurements, with the aim to facilitate a comparison of FC and ESA-ToF, we buffer the gridded FC with a trans-impedance amplifier with a gain of 25 kV/A and a bandwidth of 25 MHz. The amplifier consists of two stages. The first, a trans-impedance stage with 5 kV/A gain, is based on a high speed operational amplifier (OPA847 of Texas Instruments) with a low input current noise of 2.5 pA/$\sqrt{\text{Hz}}$ and a gain bandwidth product of 3 GHz. This stage is followed by a non-inverting output stage (OPA691) with tenfold

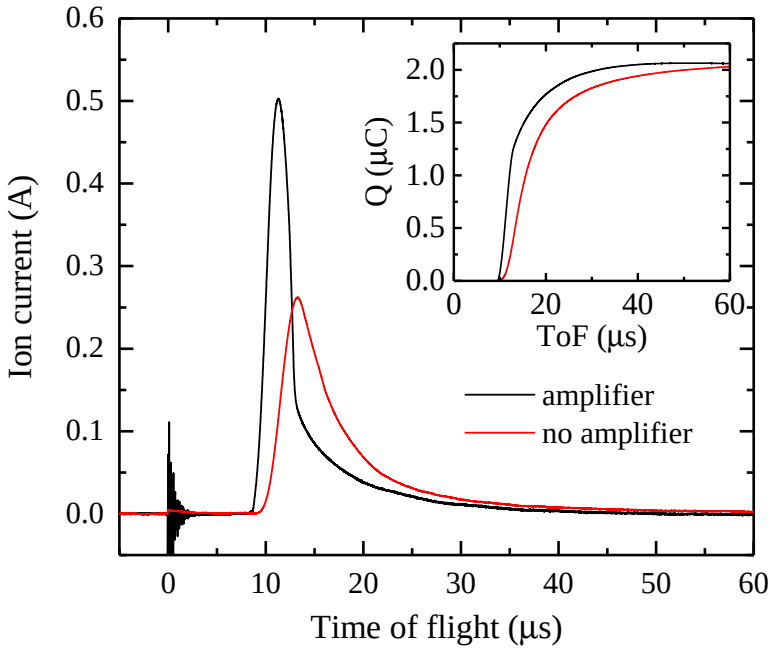

Figure 1.4: The amplified signal of the gridded FC (black line) vs raw signal (red line). The total collected charge (inset) is very similar for the two readout methods, with an accumulated charge of 2.0 μC some 60 μs after the generation of plasma.

amplification. The output impedance of the amplifier is 50 Ω. Due to the fast response of the amplifier, deconvolution of the measured signal from the measurement electronics is not necessary in order to accurately reflect the ion current impinging upon the collector.

An additional experiment was conducted to confirm the gain of the trans-impedance amplifier. Using a stable tin droplet plasma source for generating ions, the ion current was assessed twice with the same FC: with and without amplification. The ToF traces are presented in figure 1.4. The fast response time of the amplifier is apparent in the amplified signal (black line), whereas the raw signal (red line) suffers from a large RC time, on the order of several microseconds (consistent with an expected RC time of RC $\approx 10\,\mathrm{k\Omega} \times 400\,\mathrm{pF} = 4.0\,\mu\mathrm{s}$). Both time-integrated currents (*i.e.*, the time-dependent collected charge) converge to a common value of $\sim 2.0\,\mu\mathrm{C}$, as illustrated in the inset. The amplifier gain is therefore established to be equal to its expected value of 25 kV/A. Measured ion transients have a typical duration on the order of several 10 μs. Our amplifier, providing an amplified capacitive readout of the FC, was designed accordingly to have a fast current ramp-up (ns) and a particularly slow (negative) charge re-flow (tens of ms).

1.3 Characterization of the ESA-ToF energy analyzer

1.3.1 Count rate effects

Averaged over the full duration of a ToF spectrum taken at a specific scaled pass energy (E_0/z), the count rates are not very high, but as shown in subsection 1.2.2 the ions arrive at the detector in single charge state batches. Typical bunch lengths are on the order of 1 µs, therefore a batch of just 100 Sn^{z+} ions corresponds to a rate of no less than 100 MHz. Even for instrumental dead times of the order of nanoseconds, such high count rates imply that the different types of detector dead time need to be considered.

When a single Sn ion impinges onto the head of the channeltron and releases an electron from the channeltron's surface, it triggers an avalanche of electrons, which is sustained by a large bias voltage (typically in the 2 to 3 kV range) across the channeltron. The avalanche of electrons is collected by an anode at the tail of the channeltron, producing a current transient. This transient charge current associated with the avalanche of electrons is a few ns long and can be picked up by standard data acquisition electronics (we use a 600 MHz Keysight Infiniium oscilloscope). Such an electron avalanche temporally lowers the potential over the channeltron. Subsequent ion impacts on the channeltron may thus produce signals with a smaller amplitude until the gain of the detector is fully recovered. This phenomenon is exemplified in figure 1.5.a where a height distribution of channeltron pulses is shown for Sn^{5+} ions at a scaled pass energy E_0/z of 355 eV which corresponds to a kinetic energy of 1775 eV for Sn^{5+} ions. Time of flight traces accumulated over five laser-shot produced LPP plasmas are shown. As expected, a decrease in the signal amplitude is observed at high count rates. While at the start of the batch a −25 mV detection threshold would be appropriate to distinguish real counts from background and noise, later on in the batch such a threshold would rule out some real counts. By making use of a dynamic threshold equal to half of the local average amplitude of the signal peaks, an unnecessary loss of counts is prevented. The ion detection peak signals are several ns wide, and often extended with a shoulder feature and low-amplitude ringing signals. By setting a 10 ns-wide software dead time, it is ensured that these features are not counted separately. This software dead time of 10 ns is taken as the (non-extending) dead time τ_{np} of the ESA-ToF detector.

Depending on the properties of the detector system, two basic types of dead time can be identified, *e.g.* [29], i - non-extending (or non-paralyzed) or ii - extending (or paralyzed) ones. Basically, after the registration of a first particle on the detector, if a second one hits the detector within the dead time (τ) of the system, depending on the detector properties, the system's dead time will not (type i) or will (type ii) be extended. Being able to judge what is the leading type of deadtime requires an accurate knowledge of the types and numerical values of all relevant dead times. In a wide variety of fields, from nuclear and high-energy detector

research, via photon science at synchrotrons, to biomedical imaging *e.g.* [30–33] further extensions are made, for instance by introducing longer software dead times, determining time distributions between recorded events, or using hybrid dual dead time descriptions to cope with high count rates.

Given the 10-ns software deadtime, which is relatively long compared to the transient pulse width, we can effectively view our detector as having a constant, non-extending dead time. For a detector with such a constant dead time, τ_{np}, to first order the measured count rate (R_{m}) connects to the actual incoming particle rate on the detector (R) as

$$R_{\mathrm{m}} = \frac{R}{1 + R\tau_{\mathrm{np}}}. \tag{1.3}$$

For the ESA-ToF system used to diagnose Sn ions coming from the Sn droplet LPP, the natural isotope distribution of Sn enables us to assess the validity of count rate corrections based on Eq. (1.3).

Figure 1.5.b illustrates the need for isotope-specific count rate corrections. The figure presents a histogram of detected ion transients resulting from the acquisition from 200 laser shots on droplets (the results of five acquisitions are shown in figure 1.5.a for clarity). The blue line is a least-square fit to the histogram of a sum of Gaussian functions with equal width, and with amplitudes following the natural isotope abundance of Sn. The three free fit parameters are i - Gaussian width σ, ii - amplitude and iii - centroid time of flight position.

The fit underestimates the amplitudes corresponding to the heavier and the lighter isotopes. These count rate effects may be highlighted by restricting the fitting range of the histogram to those sections of the histograms where ion counting is not dead-time-limited, *i.e.* the low-abundance isotopes. The yellow line represents the result of such a fit that excludes the area (shaded yellow in figure 1.5.b) where count rate effects will be most pronounced. The result clearly demonstrates the under-counting of in particular the most abundant isotopes. The true number of impinging ions could be obtained from the integral of such range-restricted fitting. This approach would however eliminate most of the counts from the fitting procedure, thereby deteriorating the statistical confidence in the fit. Therefore, in the following, we employ Eq. (1.3) to obtain the true count rates using all detected hits.

In figure 1.6, the ToF histogram of the measured number of ions (S_{m}) for $U_{\mathrm{ESA}} = 71$ V and $z = 5$ is fitted with the non-paralyzed model (green line) using Eq. (1.3) in tandem with a spectral distribution function based on the natural isotope abundances (F_i, see Table 1.1) of Sn and Gaussian ToF distributions $G_i(t, t_i, \sigma)$ for each of the isotopes, with t the time of flight, t_i the centroid ToF of isotope i, and σ the the preset Gaussian width common to

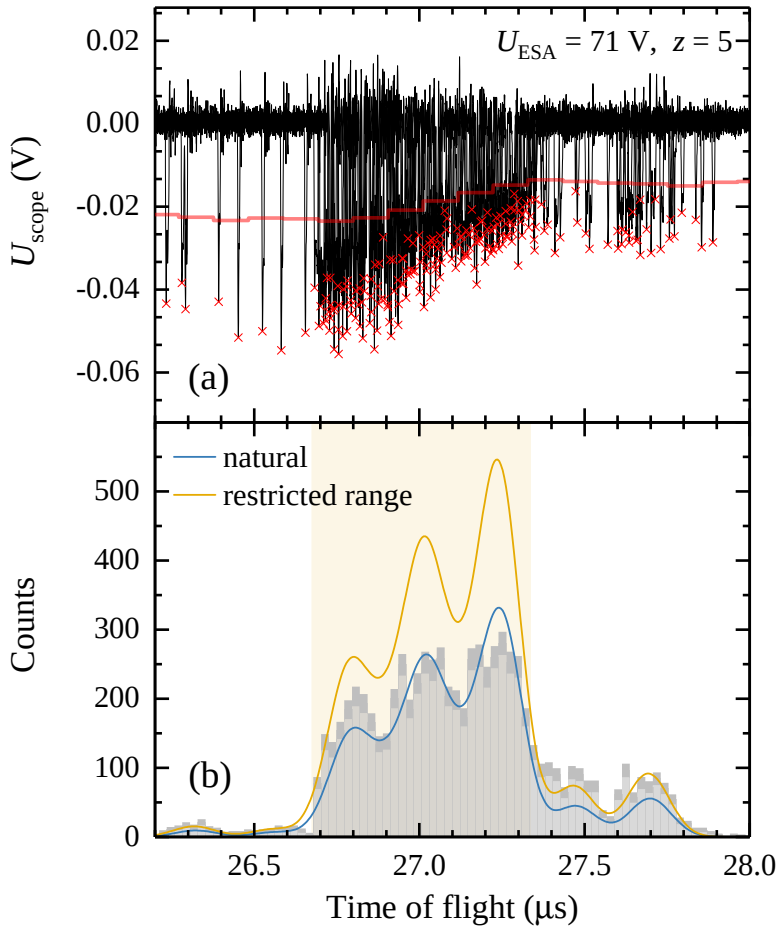

Figure 1.5: Panel (a) shows examples of ESA-ToF transients built up out of five traces of 1775 eV Sn^{5+} (scaled pass energy $E_0/z = 355$ eV). For all traces the ions stem from a LPP plasma produced by 10-ns, 60 mJ laser pulses. The red line indicates the threshold level used to discriminate counts, which are represented by the red crosses. (b) The corresponding ToF histogram (200 laser shots included) is fitted assuming a natural Sn isotope distribution (blue line). A similar fit (yellow line) is performed while using only the low-abundance, lightest and heaviest isotopes (ranges outside the shaded yellow area), which have the lowest count rate and are the least likely to be affected by high count rates. The statistical error in the number counts per bin is shown in dark gray.

all isotopes (see below section 1.3.2). The spectral distribution function is thus defined as $\sum_i F_i G_i(t, t_i, \sigma)$. This yields the following description of the measured number of counts:

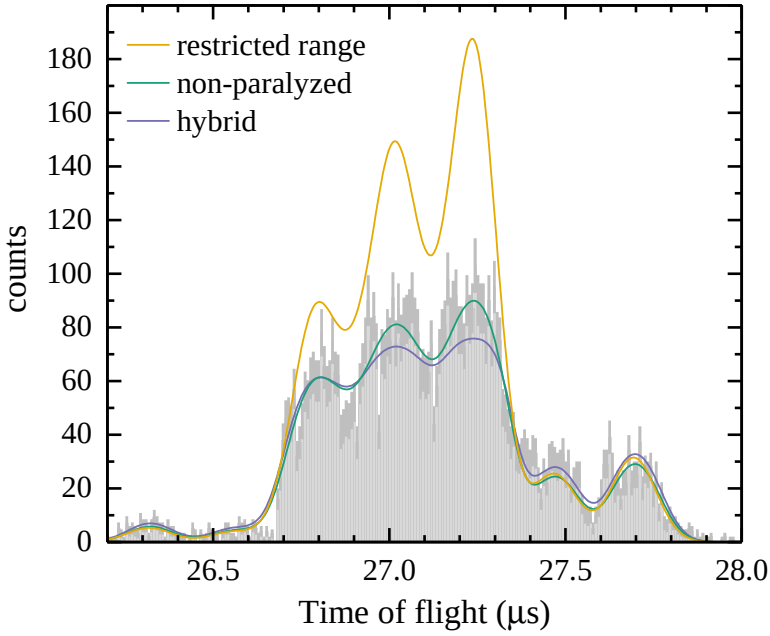

Figure 1.6: ToF histogram of Sn^{5+} ions of 1775 eV. Fits of the non-paralyzed (green line) and the hybrid (purple line) models to the data are shown. The range-restricted model from figure 1.5 is also presented. Statistical errors of the bin heights are shown in dark gray. The data are identical to those shown in figure 1.5 but with thrice the number of bins (see main text). The detected number of ions in the histogram $N_z^{\mathrm{m}}(E)$ is 7375, and the real number of ions N as recovered from the model fits is 12603 and 15455 for the non-paralyzed and hybrid models respectively.

$$S_{\mathrm{m}}(t) = R_{\mathrm{m}} T_{\mathrm{m}} = \frac{N \sum_i F_i G_i(t, t_i, \sigma)}{1 + \sum_i F_i G_i(t, t_i, \sigma) N \tau_{\mathrm{np}} / T_{\mathrm{m}}}. \tag{1.4}$$

T_{m} is the time over which the counts per bin are accumulated and is equal to number of acquisitions N_{tr} times the bin width Δt. A common way to estimate the number of bins needed to sample a Gaussian function is the square root of the number of counts. Here we deal with 10 isotopes with partly overlapping peaks, therefore the number of bins is taken as three times the square root of the number of hits. The histogram bins are distributed over a time window defined by the time of flight of virtual tin isotopes with 1 mass unit less than the lightest stable isotope and 1 mass unit heavier than the heaviest one. Note that the sum of $S_{\mathrm{m}}(t)$ over the bins within the time window equals the total measured number of ions in charge state z evaluated at kinetic energy E, $N_z^{\mathrm{m}}(E)$. In addition it should be realized that

the width of the time window scales inversely with the ToF of the ions. The higher the energy of the particles, the narrower the time window.

The fit parameter of prime interest is N, the total number of ions triggering the detector. For comparison purposes, the range-restricted fit (yellow line) is shown in figure 1.6 along with a hybrid count rate model fit [34] (purple line), in which an additional paralyzed dead time of 1.5 ns is included. A good agreement between the histogram and the non-paralyzed and hybrid models is observed and the heights of all peaks are properly reproduced, in particular by the non-paralyzed model. Even for this maximum count rate case, a relatively small $\sim 20\%$ difference in true number of hits (N) was obtained comparing the non-paralyzed and hybrid models (for most data this difference is much lower, at the percentage level, see below). Therefore in the following the simpler non-paralyzed model is used. The ratio between $N_z^{\mathrm{m}}(E)$ and N is the correction factor η_{CR} introduced in section 1.2.2. The model-related uncertainty can be gauged by comparing the non-paralyzed and range-restricted fits, which differ 7% on average, a number that can be considered as being representative for the model uncertainty. The average difference between hybrid and non-paralyzed outcomes is a similar 6%.

Figure 1.7 summarizes the count rate correction factor results obtained from fitting Eq. (1.4) to a large set of ToF spectra covering many charge states, energies (which correspond to different ToF ranges) and count rates. The inverse count rate correction factor $1/\eta_{\mathrm{CR}}$ is shown as a function of a scaled effective count rate, which allows for the use of a single set of η_{CR} values for high count rate correction independent of the ToF range in which the ions are detected. Here, the average scaled count rate R^* is defined as $N_z^{\mathrm{m}}(E)/\mathrm{ToF}_z(E)$, with $\mathrm{ToF}_z(E)$ the average ToF of all Sn isotopes in charge state z and with energy E, which corresponds to the ToF of a Sn particle of average mass of 118.7 amu. R^* takes out the fact that the width of the ToF window in which all isotopes of a specific charge state z and energy E arrive at the detector scales linearly with the ToF. Given that the number of sampling bins is taken proportional to the square root of the number of detected ions $N_z^{\mathrm{m}}(E)$, for the same number of detected ions, the sampling bin widths and thus the count rate scale with $1/\mathrm{ToF}_z(E)$. The excellent agreement between model and data shows that with R^* as parameter, a common set of correction factor η_{CR} can be used to correct the detected number of ions for possible high count rate effects. Another benefit is that one does not need to fit every spectrum to obtain the true number of ions; it suffices to count the number of detected hits in the validated range (*cf.* Fig. 1.7) of count rate values and the corresponding pass energies.

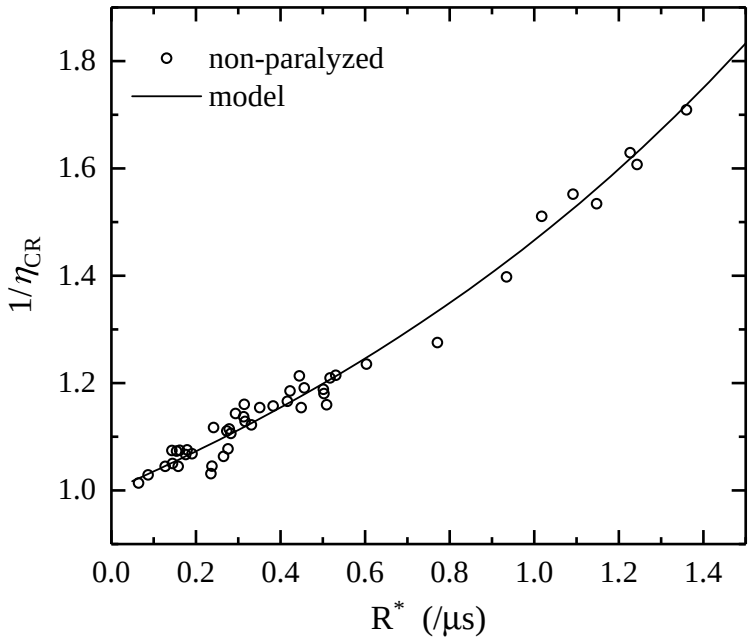

Figure 1.7: The inverse count rate correction factor $1/\eta_{CR}$ versus scaled count rate, R^*. The data are obtained by fitting Eq. (1.4) to the measured spectra. The analytical trend (black line) is calculated on basis of Eq. (1.4), using a width of the Gaussian functions corresponding to an energy resolution of α_E of 1.1% (see section 1.3.2).

1.3.2 Energy resolution

As explained in section 1.2.2, the energy resolution of the ESA-ToF is required to derive absolute ion energy distributions [*cf.* Eq. (2.3)]. A cylindrical ESA has a constant $\alpha_E \equiv \Delta E/E$ energy resolution. Experimental data feature smooth Gaussian-like distributions around each isotopic peak, whereas an ideal ESA would present a discrete and sharp "block" acceptance interval determined by the geometry of the ESA. The absolute resolution ΔE is chosen to be equal to w_E, the FWHM of the Gaussian distributions following [28]. The time domain resolution is translated to the energy domain using $\Delta E\,(E)\,/E = 2\Delta t\,(t)\,/t$. A common value for α_E was seen to be in good agreement with all data, in line with expectations. An average relative energy resolution $\alpha_E \equiv w_E/E_0 = 1.1\,\%$ was extracted by fitting all ToF histograms.

1.3.3 Detection efficiency

The detection efficiency of a CEM depends on the probability for the impinging particles to produce secondary electrons by their impact on the CEM surface. For ions in low charge states the generation of secondary electrons is determined by kinetic electron emission, *i.e.*, electrons are produced by the interaction of the projectile particle with electrons on the CEM surface. The average yield of secondary electrons stemming from kinetic electron emission increases with impact velocity [35, 36].

Typically, ions that carry more potential energy than twice the work function of the target material can also generate secondary electrons by means of potential-energy-driven Auger electron emission [37]. The yield of secondary electrons produced by potential energy emission is only weakly dependent on impact energy [38].

To accurately reconstruct the number of ions of different energies and charge states passing through the ESA-ToF, a careful calibration of the channeltron detection efficiency is required. Such a calibration can be performed by post-accelerating the ions that passed through the ESA by applying a suitable bias potential to the detector head. The bias voltage at the head of the CEM is stepped from zero to $-3.5\,\mathrm{kV}$ in steps of $-100\,\mathrm{V}$ while keeping the voltage across the CEM, and thus the gain, constant at 2145 V. For each CEM head voltage setting we scan U_{ESA} through a small array of voltages (12 for this calibration) to obtain a range of ion E_0/z ratios. The total kinetic energy of the impinging ions is $E_0 + zU_{\mathrm{head}}$, with U_{head} the voltage on the head of the channeltron. To obtain sufficient data for the low-energy, low-charge state ions, a hydrogen buffer gas was added (in between the LPP and the ESA-ToF) in part of the measurements. The addition of this tenuous buffer gas increased significantly the number of singly and doubly charged Sn ions as Sn ions in higher charge states are driven into lower charge states by means of electron capture from the H_2 gas.

Figure 1.8 shows the relative detection efficiency of the ESA-ToF channeltron obtained from our calibration measurements. For all charge states of the Sn ions a monotonically increasing detection efficiency with impact velocity (deduced from the total kinetic energy) is observed. The data obtained for each charge state have an arbitrary relative scale, given that the incoming number of Sn ions of a particular charge state and energy is not known. The individual, smooth data curves can however be overlapped by minimizing the respective differences in the common impact velocity ranges. A smooth generic curve is obtained, which describes the energy-dependent calibration of the detection efficiency after setting a $\eta_\infty = 70\%$ (following Krems *et al.* [26]) asymptotic value for the maximally obtainable detection efficiency. The thus obtained data can be compared to the measurements (red line) by Krems *et al.* [26] using Xe ions, being of very similar mass. There is a good agreement between their and our data. It is of note that the Xe ions have a higher potential energy which may lead to a small additional contribution to the detection efficiency of Xe ions.

For C_{60} ions where secondary electron emission is solely induced by kinetic energy, Schlathölter *et al.* [39] used a semi-empirical description of the detection efficiency curve, which incorporates the velocity dependence of kinetic, secondary electron emission [35]:

$$\eta_{\mathrm{det}}(v) = a_1 \left(a_2 + \tanh\left(\frac{v - v_0}{a_3} \right) \right), \tag{1.5}$$

where $a_1 \left(a_2 + 1\right) = \eta_\infty = 70\%$ is the maximum detection efficiency and v the impact velocity. According to the ion potential energy considerations raised above, only $z = 1$, $z = 2$ and the high-energy $z = 3$ data were used for fitting. The resulting calibration curve (black dashed line) is shown in figure 1.8, and is in very good agreement with the Krems curve. The resulting fit parameters are $a_1 = 0.41$, $a_2 = 0.70$, $a_3 = 0.024$ a.u., $v_0 = 0.034$ a.u. Sn ions with higher charge states $z > 2$ have higher detection efficiencies due to their additional potential energies; this effect is clearly observed at impact energies below 2 keV.

In the following, the CEM bias is set to -2050 V at which point potential emission of the higher charge states are negligible compared to the respective kinetic emission and all charge states can be well described by the single calibration curve shown in figure 1.8.

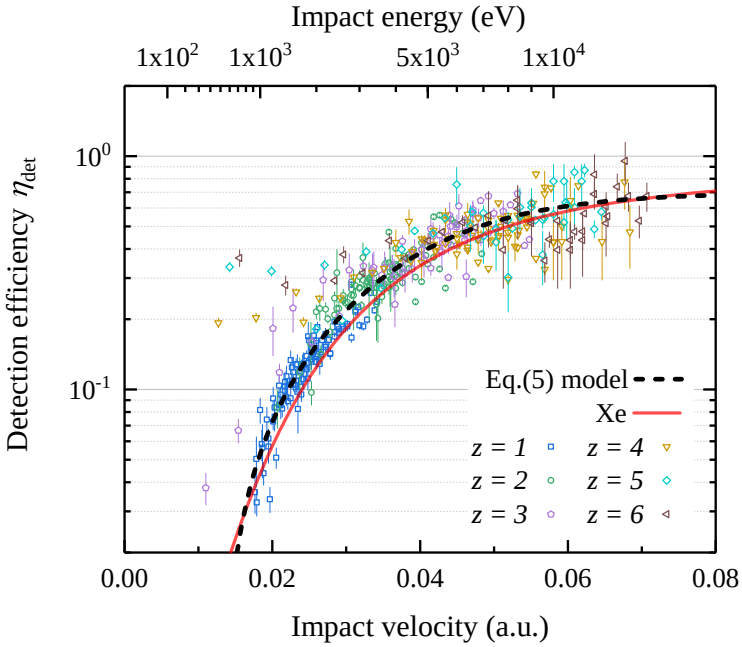

Figure 1.8: Absolute CEM detection efficiency of tin ions as function of impact velocity and energy $E + zU_{\mathrm{head}}$. The fit of Eq. (1.5) to the data (see main text) is shown as a black dashed line. The red line presents data from Krems *et al.* [26] for the detection of Xe ions.

The calibrated ESA-ToF can now be employed to accurately characterize ion energy distributions from the laser-driven plasma. In the following an ESA-ToF spectrum is presented and critically compared with the charge-integrated FC trace obtained simultaneously.

1.4 ESA-ToF and FC cross-calibration

Figure 1.9 presents the absolute ion charge energy distribution and current as measured by the ESA-ToF and a FC (see figure 1.1), after applying the corrections outlined previously. The data were obtained under experimental conditions similar to those of the calibration but at a different laser pulse energy of 60 mJ.

Following Deuzeman *et al.* [13], the conversion from a charge current in time- to energy-domain is performed using

$$\frac{dQ}{dE} = \frac{dQ}{dt}\frac{dt}{dE} = I\frac{t}{2E}, \tag{1.6}$$

where dQ/dE and $dQ/dt = I$ are the signals in the energy domain (*cf.* figure 1.9.a) and the time domain (*cf.* figure 1.9.b), respectively. The contributions from the individual charge states measured with the ESA-ToF (colored lines, see legend) are multiplied with their respective charge z to portray the energy distribution of the collected electric charge:

$$\frac{d^2Q_z}{dEd\Omega} = ez\frac{d^2N_z}{dEd\Omega}. \tag{1.7}$$

The data indicate the presence of a large range of ion charge states, up to $z = 8$. Higher charge states may in fact be present in exponentially low quantities, but here cannot be reliably detected given their rarity and the maximum resolvable charge state of the ESA-ToF (see section 1.2). The charge-state-resolved energy distributions have similar, peaked shapes. The positions of the peaks appear to be a smooth function of charge z. Between 2 and 3 kV the charge-state-resolved spectra exhibit a common peak, which in turn produces a peak in the charge-integrated distribution. The peak is followed by a sharp drop-off; no ions are detected above 5 – 6 keV.

The overall energy distribution (black dotted line) is the sum of contributions from the individual charge states:

$$\frac{d^2Q}{dEd\Omega} = \sum_z \frac{d^2Q_z}{dEd\Omega} = \sum_z ez\frac{d^2N_z}{dEd\Omega}. \tag{1.8}$$

It can be compared to the charge-integrated data acquired with the FC. Figure 1.9.b shows the ion current detected by both instruments, and processed as described above. To facilitate

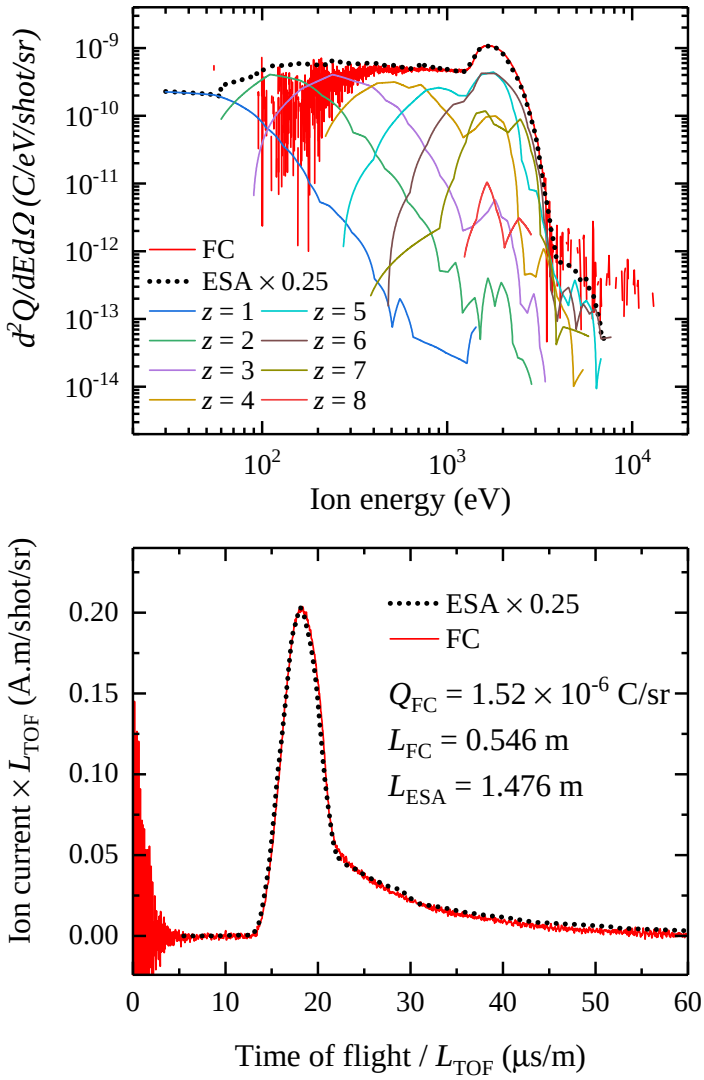

Figure 1.9: (a) Charge-state-resolved ion energy distribution of a Nd:YAG-driven tin droplet plasma for a laser energy of 60 mJ and a pulse duration FWHM of 10 ns. The charge-state-integrated energy distribution (black dotted line) as measured by the ESA-ToF is shown along with the measurement from a Faraday cup (red line). (b) Reconstructed ESA-ToF ion current transient (black dotted line) and the ion current from the Faraday cup (red line). In panels (a) and (b), the ESA-ToF data are multiplied by an overall scale factor of 0.25 (see main text).

a direct comparison of the measured ion currents, the time axis has been stretched by a factor $1/L_{\mathrm{ESA}}$ and $1/L_{\mathrm{FC}}$, and the current axis was multiplied by L_{ESA} and L_{FC} respectively for the FC and for the ESA-ToF. All data were corrected for solid angle. Ion current traces of 1000 laser shots were averaged for the FC and 200 laser shots for the ESA-ToF. The resulting current is corrected for the 41% transmission of the four grids. Using Eq. (1.6), the averaged time of flight trace (red line in figure 1.9.b) is converted to the energy distribution of the total charge collected by the FC (red in figure 1.9.a). Lastly, using the FC as an absolute benchmark, an overall scale factor of 0.25 was applied to the ESA-ToF's $dQdEdOm$ data and corresponding ion current amplitude for optimum agreement between FC and ESA-ToF. This scale factor is related to the fact that Eq. (2.3) gives the total count rate up to a common pre-factor associated with the interpretation of the energy resolution ΔE. We attribute the difference factor to the fact that the ESA does not exhibit the ideal rectangular pass band [28] and the practical assumption that the transmission function (resolution) is of Gaussian shape width, following Granneman [28], its full-width-half-maximum proportional to the true resolution by an instrument-specific multiplication factor. It is the relative calibration to the FC that enables obtaining this missing factor. The overall $\sim 20\%$ calibration uncertainty is dominated by the uncertainty in establishing the resolution ($\sim 10\%$), in the count rate model ($\sim 7\%$), and the asymptotic value of the CEM calibration curve ($\sim 10\%$). The now fully corrected ESA-ToF data are in excellent agreement with the FC data both in energy and ToF representation.

1.5 Conclusion

We present a charge- and energy-resolved spectrum of Sn ions produced by laser-driven microdroplet-tin plasma relevant for the production of extreme ultraviolet (EUV) light. For this purpose, we calibrated an electrostatic analyzer used in time-of-flight mode (ESA-ToF). The calibration procedure included the characterization of the channeltron detection efficiency, the energy resolution, and the influence of (high) count rate effects - facilitated by the wide isotope distribution of tin. Charge-summed distributions obtained from the calibrated ESA-ToF are shown, after multiplication with a global constant factor, to be in excellent agreement with Faraday cup measurements (using two distinct types of FCs, with and without amplifier circuitry) further validating the calibration procedure, enabling absolute measurements of charge-state-resolved spectra to characterize and optimize future sources of EUV light.

Acknowledgements

The authors thank Duncan Verheijde for his support in understanding and improving the ESA-ToF electronics. They also thank Jorijn Kuster for designing efficient and user-friendly software interfaces for our experimental setups. This work has been carried out at the Advanced Research Center for Nanolithography (ARCNL), a public-private partnership of the University of Amsterdam (UvA), the Vrije Universiteit Amsterdam, the Dutch Research Council (NWO) and the semiconductor equipment manufacturer ASML. This project has received funding from European Research Council (ERC) Starting Grant number 802648. This publication is part of the project New Light for Nanolithography (with project number 15697) of the research programme VIDI which is (partly) financed by the Dutch Research Council.

chapter 2

High-energy ions from Nd:YAG laser ablation of tin microdroplets: comparison between experiment and a single-fluid hydrodynamic model

Diko J. Hemminga, Lucas Poirier*, Mikhail Basko, Wim Ubachs, Ronnie Hoekstra, Oscar O. Versolato, and John sheil

Plasma Sources Science and Technology **30**, 105006 (2021).

We present the results of a joint experimental and theoretical study of plasma expansion arising from Nd:YAG laser ablation (laser wavelength $\lambda = 1.064\,\mu m$) of tin microdroplets in the context of EUV lithography. Measurements of the ion energy distribution reveal a near-plateau in the distribution for kinetic energies in the range 0.03 – 1 keV and a peak near 2 keV followed by a sharp fall-off in the distribution for energies above 2 keV. Charge-state resolved measurements attribute this peak to the existence of peaks centered near 2 keV in the Sn^{3+} – Sn^{8+} ion energy distributions. To better understand the physical processes governing the shape of the ion energy distribution, we have modelled the laser-droplet interaction and subsequent plasma expansion using two-dimensional radiation hydrodynamic simulations. We find excellent agreement between the simulated ion energy distribution and the measurements both in terms of the shape of the distribution and the absolute number of detected ions. We attribute a peak in the distribution near 2 keV to a quasi-spherical expanding shell formed at early times in the expansion.

* LP conducted the electrostatic analyzer measurements and their analysis, and took part in discussions.

2.1 Introduction

Laser-produced plasmas (LPPs) formed on tin microdroplets are now established as the light source of choice in new-generation lithography machines for high-volume manufacturing of integrated circuits below the 10 nm node [15, 40, 41]. Their incorporation in modern-day lithography machines relies on their ability to provide sufficiently high fluxes of short-wavelength radiation to enable the patterning of nanometer-scale features on integrated circuits.

Under optimum conditions, spectra recorded from tin LPPs exhibit an intense, narrow band emission feature centered near an extreme ultraviolet (EUV) wavelength of 13.5 nm [7, 8, 42–44]. The superposition of millions of lines arising from transitions between complex configurations in $n = 4$ shell Sn^{11+} – Sn^{15+} ions are the atomic origins of this light [11, 45–48]. Importantly, this feature overlaps with the 2% reflective bandwidth (13.5 ± 0.135 nm — the so-called "in-band" region) of molybdenum/silicon multilayer mirrors (MLMs) [9]. Such mirrors are an integral component of EUV lithography (EUVL) tools, transporting EUV photons from the light source to their final destination at the wafer stage.

One key aspect of industrial EUV light source development has focused on optimising the photon output of LPP EUV light sources. To-date, efforts have concentrated on increasing (i) EUV power and (ii) the so-called conversion efficiency (CE — the ratio of in-band EUV energy emitted into the half sphere back towards the laser to input laser energy) of the light source [40, 44]. To meet the high power levels required for industrial applications, a dual-pulse irradiation scheme is employed [49]. First, a low-intensity pre-pulse is used to deform the droplet into an elongated disk-like target. This target is then irradiated by a second, high-energy CO_2 laser pulse ($\lambda = 10.6\,\mu$m) which generates a hot, EUV-emitting plasma. This EUV light is then focused by an MLM (the collector mirror) to an exit port of the light source vessel whereupon it enters the scanner tool for use in the lithographic process. A second and no-less crucial aspect of EUV light source development has focused on the design and implementation of so-called debris mitigation schemes. In the context of the current application, plasma expansion will lead to the bombardment by tin ions on the plasma-facing collector mirror. The combined effects of sputtering and ion implantation will, over time, degrade the performance of the collector mirror and reduce EUV throughput. In an industrial setting, the light source vessel is typically filled with a background hydrogen gas to stop energetic ions from reaching the collector mirror [40, 50, 51]. One can also introduce a strong magnetic field in the region surrounding the droplet to deflect plasma ions away from the collector mirror [52–54].

A comprehensive understanding of the characteristics of the plasma expansion (distribution of ions over kinetic energy, angular distribution of ions, *etc*.) can greatly assist the design of effective debris mitigation schemes.

A number of studies examining tin plasma expansion have been performed over the past two decades. In the mid-2000s, Murakami *et al.* [2] and Fujioka *et al.* [12] demonstrated that ion energy distributions recorded from minimum-mass plasmas driven by 10 ns-long Nd:YAG ($\lambda = 1.064\,\mu$m) pulses can be described using a model of isothermal plasma expansion. In this model, the distribution of the number of ions N as a function of kinetic energy E is written

$$\frac{dN}{dE} = \frac{N_0}{E_0}\frac{1}{\Gamma(\alpha/2)}\left(\frac{E}{E_0}\right)^{(\alpha-2)/2}\exp\left(-\frac{E}{E_0}\right), \tag{2.1}$$

where $E_0 = 2zk_\mathrm{B}T_\mathrm{e}\ln(R(t)/R_0)$ is a characteristic energy scale dependent on the charge state z, electron temperature T_e, initial plasma size R_0 and a time-dependent characteristic system size $R(t)$ (k_B denotes the Boltzmann constant). In the above equation α is the dimensionality of the expansion ($\alpha = 1, 2$ and 3 correspond to planar, cylindrical and spherical geometries, respectively), Γ is the gamma function, $N_0 = (\sqrt{\pi}R_0)^\alpha n_{\mathrm{i}00}$ is the total number of ions and $n_{\mathrm{i}00}$ is the initial ion number density at the origin of the model, *i.e.*, $n_{\mathrm{i}00} = n_\mathrm{i}(r = 0, t = 0)$. Experiments performed by Bayerle *et al.* [14] also qualitatively demonstrate the applicability of Murakami's model (Eq. (2.1)) to Nd:YAG-irradiated (6 ns pulse duration) planar tin targets.

Plasmas driven by shorter, ps-duration pulses [14, 55] exhibit ion energy distributions whose shapes are better described by the planar isothermal expansion model of Mora [3]. In this case the ion energy distribution reads

$$\frac{dN}{dE} = \frac{N_0^*}{E_0^*}\sqrt{\frac{E_0^*}{2E}}\exp\left(-\sqrt{\frac{2E}{E_0^*}}\right), \tag{2.2}$$

where N_0^* is the total number of ions and the characteristic energy scale $E_0^* = zk_\mathrm{B}T_\mathrm{e}$. The main difference between the two models lies in the choice of the plasma density profile. The model of Murakami *et al.* [2] employs a Gaussian profile for the plasma density $\rho \propto \exp(-[r/R(t)]^2)$ whereas an exponential density profile is used in the work of Mora [3]. As noted by Murakami *et al.* [2], this latter form for the density profile is better suited for plasmas generated by short pulse lasers or those formed on thick targets.

Other work on the topic of tin plasma expansion has explored, for example, the role of laser pulse duration and laser wavelength on the ion energy distribution [56–58], the angular distribution of ion kinetic energies [21, 59–62], the suppression of fast ions using a low-energy pre-pulse [63, 64], and the role of electron-ion recombination during the expanding phase of the plasma [65]. It is important to note that the vast majority of these studies have investigated plasma expansion from laser-irradiated planar tin targets rather than from industrially relevant droplet targets. Much work still remains to be done on this latter topic.

The goal of the present study is to investigate plasma expansion in the form of emission of energetic charged particles from Nd:YAG-irradiated tin microdroplet targets. This study serves to complement recent work on photon emission from solid-state laser-driven EUV light source plasmas [44, 66, 67]. In contrast to the current industrial implementation, solid-state laser-driven plasmas may not require the use of a pre-pulse for efficient EUV production [44]. As such, they are a promising candidate for future laser-driven EUV light source plasmas. First we present measurements of the ion energy distributions using an electrostatic analyser (ESA). These measurements reveal the existence of peaks near 2 keV in the high-energy tails of the Sn^{3+} – Sn^{8+} ion energy distributions. These features combine to yield a peak near 2 keV in the charge-state integrated ion energy distribution. To elucidate the origin of this peak, we have performed two-dimensional radiation-hydrodynamic simulations of the plasma formation and its subsequent expansion using the RALEF-2D code. The ion energy distribution obtained from the simulations compares favourably to the measurements both in terms of the shape of the distribution and the absolute number of detected ions. We attribute the peak in the ion energy distribution to a high-velocity, quasi-spherical expanding shell formed at early times in the plasma expansion. The current work advances on the work presented in Refs. [7, 14] to provide a quantitative understanding of absolutely-calibrated measurements via radiation-hydrodynamic modelling of the expanding plasma, beyond the aforementioned idealized plasma expansion models.

The layout of this paper is as follows: In section 2.2 we discuss the experimental setup and provide details of the ion energy distribution measurements. This is followed by a description of the single-fluid, single-temperature model implemented in the RALEF-2D code and a brief discussion of the simulation parameters. In section 2.4 we discuss the results of the simulations, focusing on the temporal and spatial evolution of the speed and ion number density profiles in the expansion. In section 2.5 we compare the ion energy distribution obtained from the simulations with our experimental measurements. Comparisons are drawn with the predictions of well-known analytical models of plasma expansion into vacuum. Finally, we summarise this work in section 2.6.

2.2 Experimental setup, method and results

In the experiments, tin droplets were dispensed from a droplet generator mounted at the top of a vacuum chamber (backing pressure $\sim 10^{-7}$ mbar). The droplet generator consists of a heated (260 °C) molten tin reservoir connected to a nozzle. The diameter of the tin droplets used in the experiment was 28 µm. Upon crossing the centre of the chamber, the droplets pass through a light sheet created by a He-Ne laser. Light scattered by the droplets was detected by a photo-multiplier tube which triggered the plasma-generating laser pulse and the acquisition

apparatus. Plasmas were generated by focusing the output of a commercial Nd:YAG laser system onto the tin droplets. The laser pulses exhibited Gaussian-like temporal and (focused) spatial laser profiles. The temporal full-width at half-maximum (FWHM) was 10 ns and the FWHM of the focused pulses was approximately 60 μm. Employing a laser pulse energy of 60 mJ resulted in a laser power density on the targets of $I_{\mathrm{L}} \approx 2 \times 10^{11}\,\mathrm{W\,cm^{-2}}$. This choice of power density is known to yield optimum CE's for Nd:YAG-driven tin plasmas [44]. We note that this particular choice of laser parameters, combined with the given droplet diameter, will not lead to the full ablation of the tin droplet.

Charge-state resolved ion energy distributions were measured using an electrostatic analyzer (ESA). The opening aperture of this device was located 1.12 m away from the droplet targets and was positioned at 60° with respect to the incident laser axis. The ESA consists of a radial electric field deflection region followed by a calibrated channeltron detector. The radial electric field between the two electrodes of the ESA selects charge states based on the ratio of their kinetic energy E to charge state z according to $E/z = 5 \times U_{\mathrm{ESA}}$ where U_{ESA} is the voltage across the ESA electrodes (measured in volts). A time-of-flight (TOF) analysis is used to obtain charge-state resolved ion counts for a given E/z. By scanning the ESA voltage U_{ESA} over a desired range, one can obtain charge-state resolved ion energy distributions. The ESA-TOF measurements have been benchmarked against charge-state integrated measurements made using a Faraday cup (FC) which was positioned at an angle of −60° with respect to the incident laser axis.

The total ion energy distribution $d^2N/dEd\Omega$ was derived from the measurements via

$$\frac{d^2N}{dEd\Omega} = \sum_z \frac{N_z^{\mathrm{m}}(E)}{\eta_{\mathrm{det}}\,\eta_{\mathrm{CR}}\,\Delta E\,(E)\;\Delta\Omega}, \tag{2.3}$$

where $\Delta E\,(E)$ is the energy-dependent absolute energy resolution, $N_z^{\mathrm{m}}(E)$ is the number of tin ions of charge state z having kinetic energy in the range $E \pm (\Delta E(E)/2)$ detected by the channeltron, η_{det} is the detection efficiency of the channeltron, η_{CR} (≤ 1) is a correction for undetected counts due to high count-rate effects and $\Delta\Omega$ is the solid angle of the input aperture of the ESA device. The absolute energy resolution scales linearly with E according to $\Delta E/E \simeq 10^{-2}$. Further details regarding the ESA calibration can be found in [68].

In Fig. 2.1 we present the results of our charge-state resolved ion energy distribution measurements. Examining this figure, we first note that the distributions associated with Sn^+ and Sn^{2+} ions are rather broad, spanning energies in the range 0.05 – 2 keV. The kinetic energy for which the ion energy distribution peaks, E_{peak}, clearly increases with increasing charge state. Both distributions also exhibit a near-exponential fall-off for $E > E_{\mathrm{peak}}$. While the aforementioned trend in E_{peak} continues for Sn^{3+} and Sn^{4+}, we note the emergence of a second, high-energy peak located just below 2 keV (this peak is also present in the Sn^{2+}

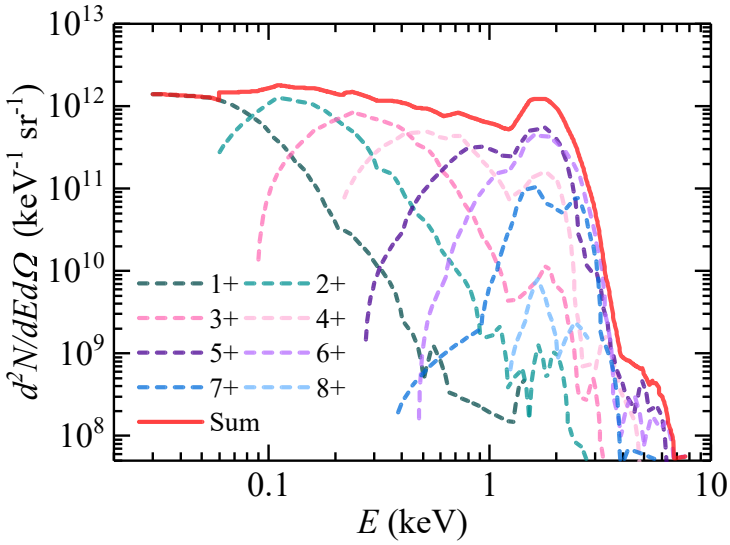

Figure 2.1: Experimental measurements of the distribution of the number of ions over ion kinetic energy is shown. Charge-state resolved ion kinetic energy distributions for Sn^{+} – Sn^{8+} are shown as dashed colored lines. The total ion energy distribution, shown in red, is obtained by summing the distributions of the individual charge states.

distribution although it is less pronounced than in the Sn^{3+} and Sn^{4+} distributions). With increasing charge state this peak grows in intensity until $E_{peak} \approx 2$ keV in the Sn^{5+} and Sn^{6+} ion energy distributions (we also make a tentative observation of two peaked features in the Sn^{7+} ion energy distribution near 1.6 and 2.5 keV, respectively). While we do detect Sn^{8+} ions in the experiments, the amplitude of ion energy distribution is an order-of-magnitude lower than the Sn^{7+} distribution. No traces of higher charge states could be reliably detected. Importantly, the kinetic energy associated with this high-energy feature is independent of charge state. Shown in red in Fig. 2.1 is the total ion energy distribution obtained by summing the individual Sn^{+} – Sn^{8+} ion energy distributions. Three distinct regions emerge: (i) a near-plateau in the ion energy distribution between 0.03 – 1 keV (ii) a peak near 2 keV followed by (iii) a sharp fall-off for $E > 2$ keV. Finally, we note that the EUV-generating tin charge states Sn^{11+} – Sn^{15+}, whilst generated in the hot, dense region of the plasma, are not detected in the measurements. The absence of Sn^{11+} – Sn^{15+} charge states may in part be attributed to the process of recombination, whereby free electrons in the expanding plasma recombine with these ions through processes such as three-body or radiative recombination [65].

2.3 Radiation Hydrodynamic simulations and the RALEF-2D code

In order to elucidate the dynamics of the plasma expansion and its influence on the ion energy distribution, we have undertaken numerical modelling of the plasma formation, growth and subsequent expansion using radiation-hydrodynamic simulations. In the following, we discuss the underlying assumptions of the single-fluid, single-temperature approach adopted in the present work and we provide details of the simulations we have performed with the RALEF-2D code.

2.3.1 Single-fluid single-temperature radiation hydrodynamics

We have chosen to model the plasma formation and its subsequent expansion using a single-fluid, single-temperature hydrodynamic model including the effects of radiation transport and thermal conduction.

In this approach, the free electrons and ions are treated as a single fluid having a single temperature $T_e = T_{ion} = T$. Although more complex approaches such as the two-fluid, two-temperature [69] or single-fluid, two-temperature models [70–73] have been pursued, the single-fluid, single-temperature description should be adequate for the current purposes. For one, simulations of Nd:YAG-irradiated lithium, plastic and gold targets performed by Sunahara *et al.* [70] indicate a rather small difference (less than 20%) between T_e and T_{ion} in the plasma. This behaviour has also been observed in simulations of laser-driven tin plasmas [74]. Second, the moderate ionisation degrees ($z \approx 11 - 15$) found in EUV source plasmas implies that the free-electron contribution to the pressure $p_e = z n_{ion} k T_e$ (in the ideal gas approximation) far outweighs the ion contribution to the pressure $p_i = n_{ion} k T_e$ (n_{ion} is the ion number density). As such, the ion temperature will play a near-negligible role in the context of the current study.

The equations of single-fluid, single-temperature hydrodynamics take the form

$$\frac{\partial \rho}{\partial t} + \nabla \cdot (\rho \mathbf{v}) = 0 \tag{2.4}$$

$$\frac{\partial (\rho \mathbf{v})}{\partial t} + \nabla \cdot (\rho \mathbf{v} \otimes \mathbf{v}) + \nabla p = 0 \tag{2.5}$$

$$\frac{\partial (\rho E)}{\partial t} + \nabla \cdot ((\rho E + p)\mathbf{v}) - (S_T + S_R + S_{ext}) = 0. \tag{2.6}$$

In the above equations, ρ is the fluid mass density, $\mathbf{v}$ is the fluid velocity, $p = p_e + p_i$ is the pressure, $E = e_{int} + |\mathbf{v}|^2/2$ is the mass-specific total energy (sum of the internal and kinetic energy contributions), S_T represents thermal conduction, S_R is the volume-specific

heating rate provided by thermal radiation and S_{ext} represents any external energy sources, *e.g.*, energy deposition from a laser beam, ion beam, *etc*.

In the single-fluid approach, the plasma is treated as a quasi-neutral fluid, *i.e.*, the electron number density n_e is related to the ion number density n_{ion} through $n_e = zn_{ion}$. It is gradients in the plasma pressure which drives plasma expansion in a quasi-neutral hydrodynamic framework. The principal criterion justifying this approach is that the local Debye length $\lambda_D = [T_e/(4\pi n_e e^2)]^{1/2}$ must be significantly smaller than the scale length of the flow variation $L = n_{ion}/ \mid \nabla n_{ion} \mid$. While this condition is typically met in the hot, dense region of the plasma ($\lambda_D < 10\,\text{nm}$), departures from it may exist as the plasma expands and rarefies. In such situations, a kinetic description of the plasma is often employed, where particle-in-cell methods are used to evolve the ion and electron particle distribution functions [49, 75–77]. We will discuss the validity of using the hydrodynamic description of a plasma in the current work in section 2.4.

2.3.2 RALEF-2D

We have performed radiation-hydrodynamic simulations using the Radiative Arbitrary Lagrange-Eulerian Fluid dynamics in two dimensions (RALEF-2D) code. This code was originally developed to provide theoretical support for laser-plasma experiments at GSI Darmstadt under moderate laser intensities $\lesssim 10^{13} - 10^{14}\,\text{W cm}^{-2}$ [78, 79]. More recently, the code has found application in modelling laser-driven plasma sources of EUV light [11, 80–83]. The hydrodynamic component of the code is based on an upgraded version of the fully-explicit CAVEAT code for ideal hydrodynamics [84, 85]. RALEF-2D solves the single-fluid, single-temperature hydrodynamic equations (Eq. (5–7)) in two spatial dimensions on a structured quadrilateral mesh in either Cartesian (x, y) or axisymmetric (z, r) coordinates using a second-order Godunov-type method [85]. The axisymmetric coordinate system has been used in the present simulations.

In the RALEF-2D code, radiation transfer and heat conduction are coupled into the fluid energy equation using a symmetric semi-implicit method with respect to time discretization [86]. The code solves the LTE radiation transfer equation in the quasi-static approximation using pre-tabulated absorption coefficients generated with the THERMOS code [87, 88]. The equation of state (EOS) of tin was built using the Frankfurt equation of state (FEOS) model which can treat both low-temperature liquid-gas phase coexistence regions as well as high-temperature plasma states [89]. The FEOS model supplies the RALEF-2D code with key thermodynamic quantities such as the pressure, mass-specific internal energy as well as the average charge state of the plasma.

The simulations were performed on a computational mesh shaped in a half-disk consisting of multiple blocks with initially distinct properties. A simplified representation of the mesh

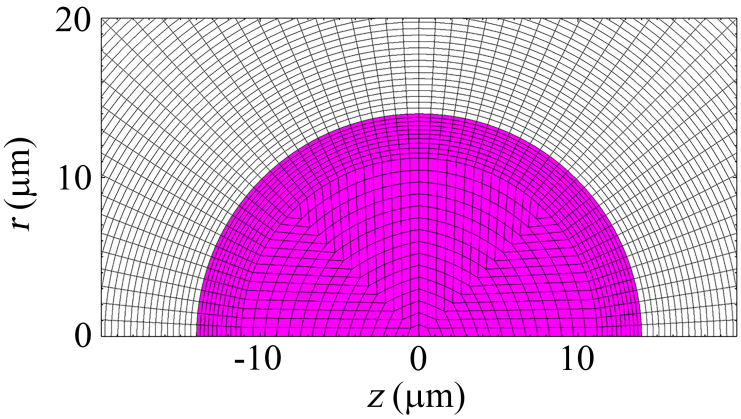

Figure 2.2: A simplified representation of the mesh structure employed in the RALEF-2D simulations. The liquid droplet, shown in purple, is assigned an initial mass density of 6.9 g cm^{-3} and a temperature of 592 K (0.051 eV). The region outside the droplet is filled with a tin vapour having a mass density of 10^{-12} g cm^{-3}.

is shown in Fig. 2.2. Centered in the origin of the (z, r) coordinate system we define a tin "droplet" having a mass density of 6.9 g cm^{-3} and a temperature of 592 K (0.051 eV). As in the experiments, the droplet diameter is set to 28 μm. The bulk of the droplet is defined in a mesh section constructed as a rectangle stretched to a half-disk with dimensions of 45×90 mesh cells. As shown in Fig. 2.2, the outer region of the droplet exhibits a more refined mesh structure. Here, the length of each successive mesh cell along the radial direction decreases with increasing r. The mesh cell length on the outer droplet boundary is approximately 10 nm. Outside the droplet the mesh is filled with a tin vapour having a mass density of 10^{-12} g cm^{-3}. This section is divided into quadrilateral cells by approximate concentric and radial edges and extends to a radial distance of 10 mm.

In essence, the experimental laser parameters have been replicated in the simulations. The laser beam is circular and coaxial to the positive z-axis. The simulations have employed unpolarized laser light. Laser energy deposition was modelled using the process of inverse bremsstrahlung.

The ion energy distribution is extracted from the fluid simulation by considering mass flow through the computational mesh. The main fluid variables density and velocity are assigned to each mesh cell throughout the simulation and are converted to the quantities mass and speed (velocity magnitude). These variables are cell-centered and form the basis of keeping track of the fluid throughout the simulation. As the curved boundary of the computational mesh is defined as a free-outflow boundary, matter flowing out of the mesh leaves the computational domain; it leaves the simulated area in space. This is closely related

to the treatment of the ion energy distribution by RALEF-2D. Mass flowing out of the mesh is recorded (*i.e.* binned) in the (i) energy bin corresponding to its speed and (ii) the angular bin corresponding to the angle between the laser axis and the escape velocity vector. This module is called at every hydrodynamic time step, summing the number of particles equivalent to the out-flowing mass. This procedure explicitly constructs the distribution of the number of particles into 360 predefined discrete energy bins in the range $[1, 20 \times 10^3]$ eV. The bin width increases exponentially with increasing energy. The angular domain is divided into 36 bins (over 180°). In the current simulation we consider mass flow into two angular bins extending over the range [55°, 65°]. The duration of the simulation is 1 μs which allows accounting for ions with energies down to about 70 eV leaving the computational domain in this time window.

2.4 Plasma formation and expansion

In Fig. 2.3 we present the evolution of the plasma expansion through the variables speed and ion number density, where the pseudocolor indicates the magnitude of these variables. At distances larger than 0.5 mm the velocity vector effectively points radially outwards. The ion number density n_{ion} is obtained from $n_{\text{ion}} = \rho N_{\text{A}}/A$, where ρ is the fluid density, N_{A} is the constant of Avogadro and A is the atomic weight of tin. For visibility, we reflect the ion number density information into the lower plane (this is possible as the simulations were performed using the axisymmetric (z, r) coordinate system). We define $t = 0$ ns as the time that the laser pulse is switched on in the simulations. The left column shows times $t = \{11, 15\}$ ns, the middle column $t = \{25, 35\}$ ns and the right column the late times $t = \{60, 120\}$ ns. The laser propagates along the positive z axis (laser axis) and its (local) intensity is represented by the black shading seen in the $t = \{11, 15\}$ ns frames.

Frames grouped in the same column, *e.g.*, $t = \{11, 15\}$ ns share the same axial and radial domains. In order to follow the plasma expansion in space, we increase the axial and radial coordinate domains in the $t = \{25, 35\}$ and $\{60, 120\}$ ns frames.

The overall dynamics of plasma formation and expansions, as displayed in Fig. 2.3, can be qualitatively described as a succession of two distinct bursts of laser-induced ablation from the droplet surface. These two bursts are clearly identified in the $t = 15$ ns and $t = 25$ ns frames as two concentric red regions exhibiting high velocity magnitude. In the following two subsections we describe the formation and evolution of these two ablation bursts.

2.4.1 Initial burst of laser-induced ablation

The initial burst of laser-induced ablation forms in the first 2 – 3 ns after the laser pulse is turned on. Initially, the laser pulse has an intensity $I \approx 3 \times 10^8$ W cm^{-2} which lies only

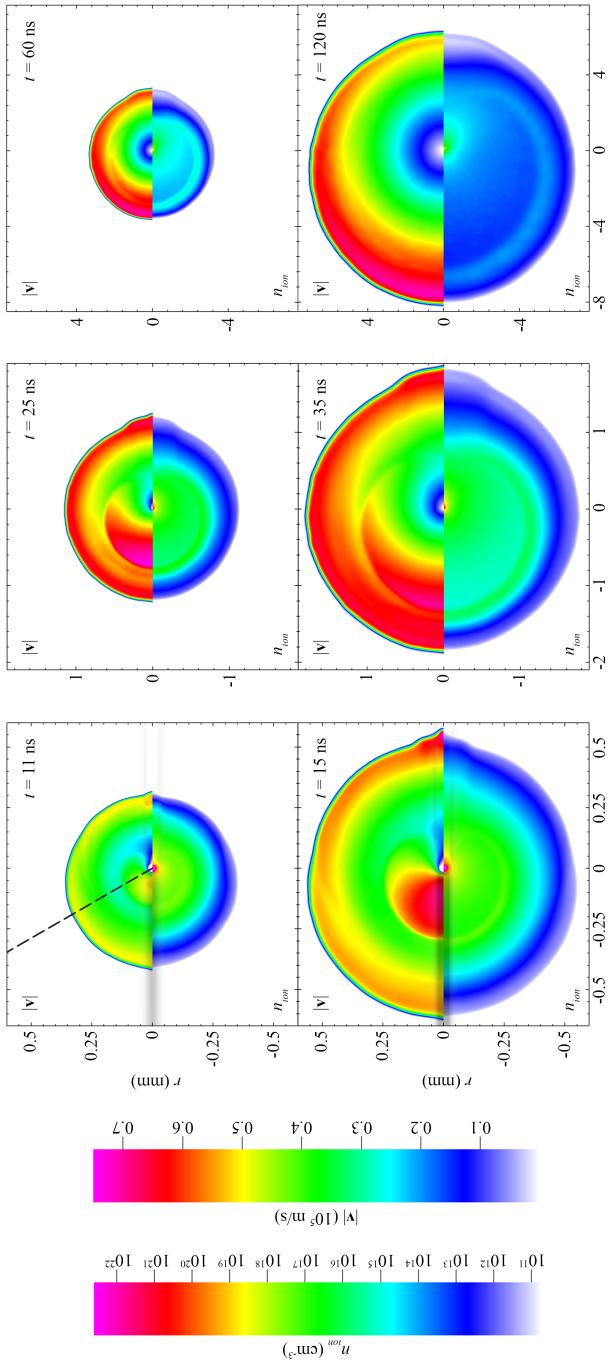

Figure 2.3: Two-dimensional profiles of the speed |**v**| and ion number density n_{ion} during laser ablation and subsequent plasma expansion are shown. The color scale represents the size of the variable. The laser illuminates from the left along the z axis, illustrated in the $t = 11/15$ ns frames by the black shaded band. The black dashed line in the $t = 11$ ns frame corresponds to the "lineout" (see main text for description) along which the speed and ion number density profiles shown in Fig. 2.5 and 2.6 are taken.

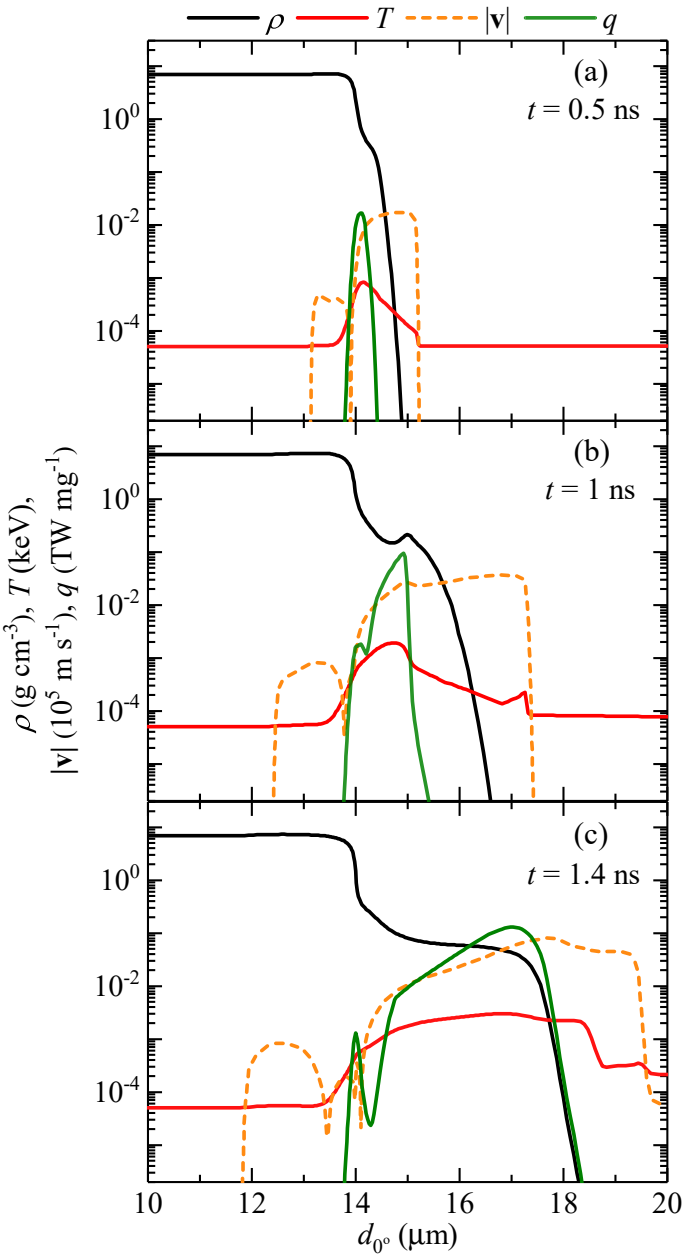

Figure 2.4: One-dimensional profiles of the mass density ρ (black), temperature T (red), speed $|\mathbf{v}|$ (orange dashed curve) and mass-specific laser heating rate q (green) along the negative axial coordinate axis for times t = (a) 0.5, (b) 1 and (c) 1.4 ns.

moderately above the ablation threshold of liquid tin. In Fig. 2.4 we plot one-dimensional (1D) profiles of the mass density ρ (black), temperature T (red), fluid speed $|\mathbf{v}|$ (orange dashed curve) and mass-specific heating rate of the laser q (green) along the negative laser axis (starting from the droplet center) at times $t =$ (a) 0.5, (b) 1 and (c) 1.4 ns, respectively. These data are extracted along a so-called "lineout" taken at $\theta = 0°$ with respect to the axial coordinate (laser) axis.

As is evident from Fig. 2.4 (b), the temperature of the ablated plasma $T \approx 1 - 2\,\mathrm{eV}$ exceeds the critical temperature of tin ($T_{\mathrm{critical}} \approx 0.5\,\mathrm{eV}$) by only a moderate factor. In addition, we notice the emergence of a hump in the speed profile at $d_{0°} \approx 15\,\mu\mathrm{m}$ which is coincident with the location of the peak value of q, the mass-specific laser heating rate. Material associated with this hump accelerates and eventually "catches up" with the initially-ablated material. By $t \approx 2.5\,\mathrm{ns}$, the speed profile exhibits a near-linear dependence on distance d, *i.e.*, $|\mathbf{v}| \propto d$ and the speed of the front edge of the plasma cloud stabilizes to $|\mathbf{v}_{\mathbf{front}}| \approx 33\,\mathrm{km\,s^{-1}}$. This expanding plasma cloud drives a shock into the low-density ($\rho = 10^{-12}\,\mathrm{g\,cm^{-3}}$) ambient gas which, however, has a negligible effect on the overall expansion dynamics.

2.4.2 Second burst of laser-induced ablation

The increase in laser intensity (and subsequent increase in the mass-specific laser-heating rate q) as $t \rightarrow 15\,\mathrm{ns}$ generates a second burst of ablation visible in the upper halves of the $t = 11$, 15 and 25 ns frames in Fig. 2.3. This second burst is characterized by a significantly higher ablation rate, density and temperature ($T > 30\,\mathrm{eV}$) of the ejected plasma whose leading edge quickly reaches a speed $|\mathbf{v}_{\mathbf{front}}| \approx 60\,\mathrm{km\,s^{-1}}$.

To better understand the dynamics of this ablation burst along the line-of-sight of the ESA and FC devices, we show in Fig. 2.5 the (a) speed and (b) ion number density profiles along a lineout taken at $\theta = 60°$ with respect to the laser axis at times $t = 5$ (black), 10 (red), 15 (blue), and 20 ns (green), respectively. This lineout is shown as a black dashed line in the $t = 11$ ns frame in Fig. 2.3. The shaded vertical bars indicate the location of local maxima in the number density lineouts and serve to guide the eye between both variables. From Fig. 2.5 we see that as the second and more powerful ablation burst rams into the background plasma (left behind by the initial ablation burst), it rakes up material into a quasi-spherical expanding shell. This shell is evident as a hump in the $t = 15$ and 20 ns n_{ion} profiles in Fig. 2.5(b). The deposition of energy (via laser absorption) and the expansion that follows can be likened to the effects of a fast piston pushing a gas; the shockwave launched by the piston effectively sweeps up material in front of it, driving a compression wave.

In Fig. 2.6 (a) and (b) we plot the speed and ion number density profiles along the $\theta = 60°$ lineout at times $t = 30$ (orange), 50 (light blue), 80 (purple) and 120 ns (dark green). As the

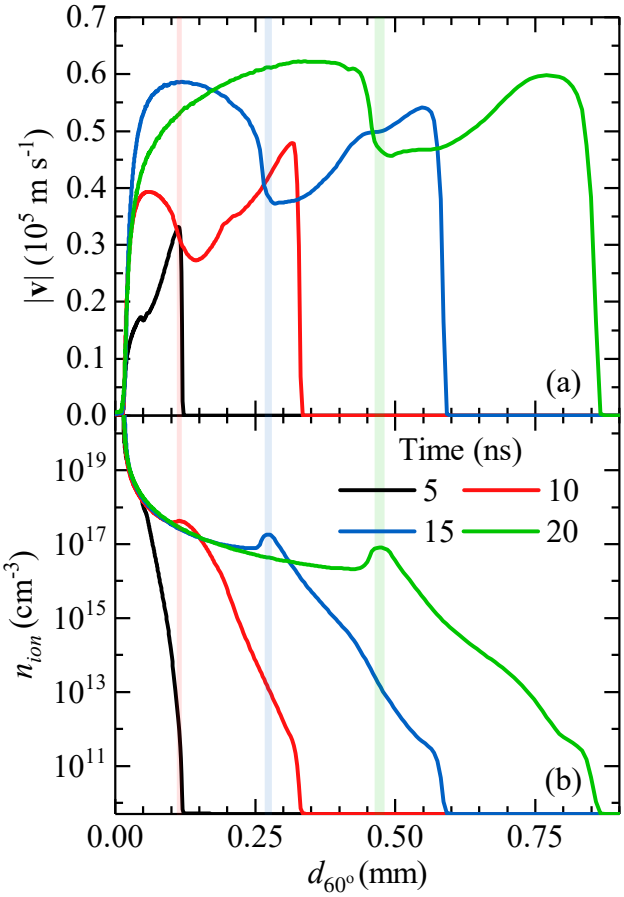

Figure 2.5: One-dimensional profiles of the (a) speed and (b) ion number density along the lineout shown in Fig. 2.3 at $t = 5$ (black), 10 (red), 15 (blue) and 20 ns (green).

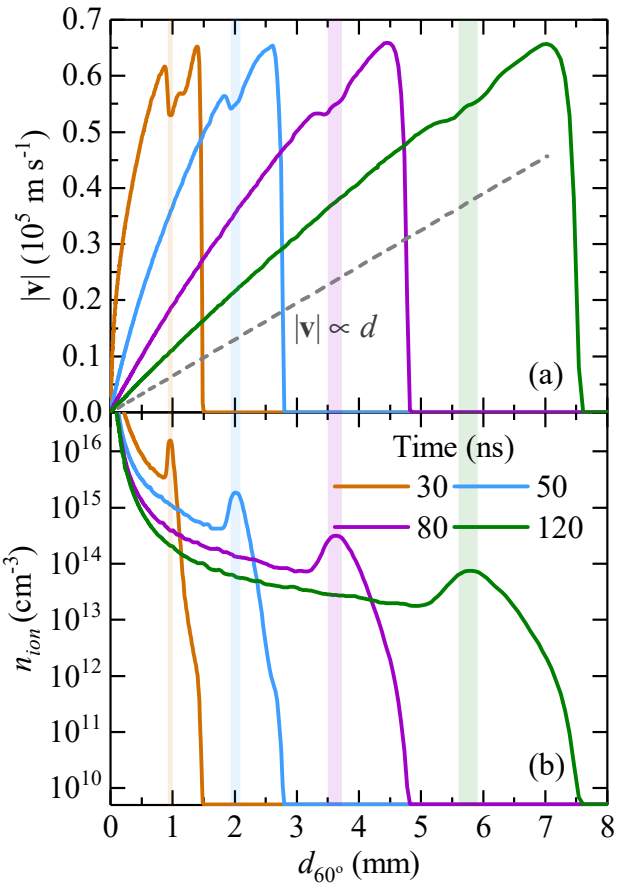

Figure 2.6: One-dimensional profiles of the (a) speed and (b) ion number density along the lineout shown in Fig. 2.3 at $t = 30$ (orange), 50 (light blue), 80 (purple) and 120 ns (dark green). The gray dashed line illustrates an analytic form for the speed $|\mathbf{v}| \propto d$.

plasma expands, we note that the two speed profiles merge to form a single profile exhibiting a near-linear dependence of the on distance. A linear dependence of speed on distance, *i.e.*, $|\mathbf{v}| = d/t$ is exactly the asymptotic $t \to \infty$ behaviour of any explosion-like expansion [4]. Our simulations therefore recover the late-time behaviour expected from such an expansion. The evolution of the ion number density profiles over time and space is less dramatic. First, we note that the quasi-spherical expanding shell observed in Fig. 2.5 (b) persists throughout the expansion. As time evolves the shell is observed to broaden, a direct consequence of the non-constant speed profile across the shell. It is interesting to note that the spatial variation of the ion number density up to the quasi-spherical shell appears to follow a power law of the form $n_{\text{ion}} \sim d^{-n}$ where $2 < n < 3$. Unlike the speed profile, a universal analytic form for n_{ion} as $t \to \infty$ does not exist for an explosion-like expansion. As discussed by Zel'dovich and Raizer [4], the asymptotic solution $|\mathbf{v}| = d/t$ is satisfied for $n_{\text{ion}} = \phi(d/t)/t^3$ where $\phi(d/t)$ is an arbitrary function of d/t. This function can only be evaluated through numerical simulations of the system and is case-specific.

Before proceeding with the comparison of experimental and simulated ion kinetic energy distribution, we wish to make two remarks. First, recall that the validity of the single-fluid description of a plasma relies on the condition $\lambda_{\text{D}} \ll L$ where λ_{D} is the Debye length and L is the characteristic flow length. We have calculated λ_{D} and L for the late time case $t = 120\,\text{ns}$ and have found that $\lambda_{\text{D}} \approx 1 - 10\,\mu\text{m}$ and $L \approx 500\,\mu\text{m}$ in the vicinity of the density hump. These results validate the use of the quasi-neutral hydrodynamic approach in the current context. It is important to mention that the mechanism of ion acceleration in the other extreme case, *i.e.*, plasmas in which $\lambda_{\text{D}} \gg L$ is often referred to as Coulomb explosion [69]. Second, recall that in the simulations the region outside the droplet is filled with a low-density tin vapour having $\rho = 10^{-12}\,\text{g cm}^{-3}$. The experiments, on the other hand, have been performed in a near-vacuum environment. This choice of density is sufficiently low as not to distort the vacuum-like expansion we wish to emulate in our simulations. This is evident in Fig. 2.6 where we do not observe a slowing-down of the peak velocity/shock front as the fluid propagates through the low-density background gas.

2.5 Ion Kinetic Energy Distributions: Experiment and Simulation

We now wish to compare our measured ion energy distribution with that obtained from the simulations. These two quantities are compared in Fig. 2.7. The experimental data, shown in red, corresponds to the total ion energy distribution (also shown in red in Fig. 2.1) and the solid black curve is the ion energy distribution obtained from the RALEF-2D simulations. As described in section 2.3.2, the RALEF-2D ion energy distribution is obtained by recording mass flow into two angular bins subtending an angle $55° < \theta < 65°$ with respect to the

laser axis. From the two-dimensional computational mesh we have calculated the three-dimensional solid angle $\Omega_S \approx 0.95$ sr by revolving the arc length in the mesh around the laser axis. The RALEF-2D ion energy distribution, once corrected for this solid angle, is then convolved with bin-specific Gaussian functions having full width at half-maxima equal to 5% of the lower boundary of the energy bin. The purpose of this convolution is to account for processes which may broaden the distribution, *e.g.*, mass distribution of tin isotopes.

It is clear from Fig. 2.7 that the RALEF-2D ion energy distribution closely resembles the experimental measurements. First, the simulation reproduces the high-energy peak observed in the experimental data near 2 keV. This high-energy feature originates from fast-moving material associated with the quasi-spherical expanding shell (a tin ion with $|\mathbf{v}| = 57\,\mathrm{km\,s^{-1}}$ has a kinetic energy $E \approx 2$ keV).

Second, the simulations reproduce the near-constant behaviour of the experimental ion energy distribution in the $0.03 - 1$ keV range. Fluctuations observed in the RALEF-2D ion energy distribution most likely arise from spatial fluctuations in the density and speed during the expansion (visible in Fig. 2.6 for $t = 120$ ns). Above 2 keV, both the simulations and experimental data exhibit a sharp fall-off with increasing kinetic energy. This fall-off is sharper in the case of the simulations, which does not predict any ions having kinetic energies above 3 keV. It is also interesting to note that, within the limits of the experimental uncertainties, the simulations provide a reliable prediction for the absolute number of ions detected in the experiments.

We show in Fig. 2.7 the predictions of the models of Murakami (Eq. (1)) and Mora (Eq. (2)). Guided by the work of Torretti *et al.* [11], we have taken $z = 12$, $k_B T = 35$ eV and $N_0 = 2 \times 10^{12}$. For the model of Murakami we have chosen a spherical expansion ($\alpha = 3$) and a value $\ln(R(t)/R_0) = 4$. We also provide in Fig. 2.7 the ion energy distribution arising from a planar isentropic expansion, better known as the Riemann wave [4]:

$$\frac{dN}{dE} = \frac{N_0}{zk_B T_e} \frac{\gamma^2 - 1}{4\gamma} \sqrt{\frac{E_{max}}{E}} \left(1 - \sqrt{\frac{E}{E_{max}}}\right)^{2/(\gamma-1)} . \tag{2.7}$$

Here γ is the adiabatic index (we select $\gamma = 4/3$ [90]) and $E_{max} = 2zk_B T_e \gamma/(\gamma - 1)^2$ is the maximum ion kinetic energy. Both the planar isothermal expansion model of Mora and the Riemann wave solution predict a similar monotonic decrease in dN/dE with increasing E which is not observed in the experimental measurements. The shape of the experimental data is qualitatively better described by the spherical isothermal expansion model of Murakami, which exhibits a slow rise in dN/dE up to a peak at $E_{peak} = E_0/2 \approx 1.7$ keV. The fall-off in dN/dE at energies above E_{peak} is far less steep compared to the experimental data.

The reason why the models of Murakami, Mora and the Riemann wave solution cannot be expected to reproduce the current experimental distribution ultimately lies in the plasma

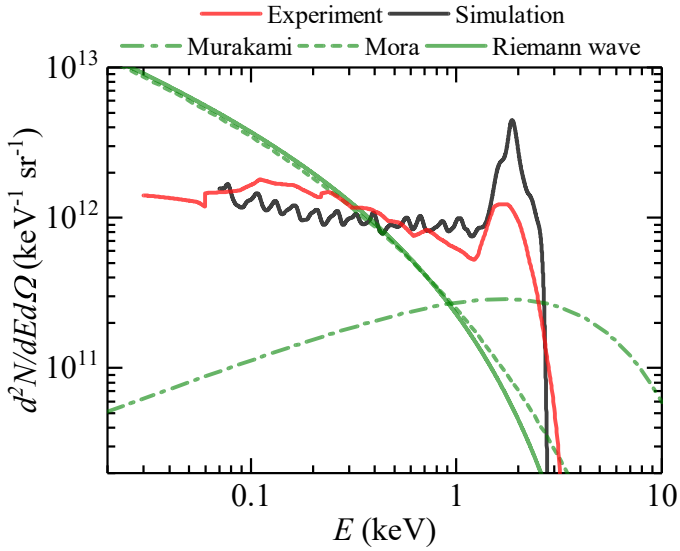

Figure 2.7: The distribution of the number of ions over ion kinetic energy. The experimental ion energy distribution is shown in red (solid curve) and the RALEF-2D ion energy distribution is shown in black (solid curve). Also illustrated are the predictions of the analytic models of Murakami (green dash-dot) [2], Mora (green dash) [3] and the Riemann wave (green solid) [4].

density profiles adopted in these analytic models.

The function $\phi(d,t)$ obtained with the RALEF-2D simulation is significantly more complex than the Gaussian or exponential density profiles assumed in the models of Murakami and Mora, respectively. It is the interaction of many complex processes (2D expansion of a non-uniformly heated, non-planar (radiating) plasma) that ultimately determines the function $\phi(d,t)$.

Four possible causes have been identified which may contribute to the observed differences between the experimental and simulated ion energy distributions. The first cause is the effect of numerical diffusion in the large mesh cells at larger mesh radii. This has been partly tackled by increasing the radial detail in the mesh at larger distances. The three other causes are inherent to the ansatz of the simulation code. As mentioned in section 2.3.2, RALEF-2D uses Godunov's method for the Lagrangian phase of each hydrodynamic cycle. As the internal energy component of the total energy determines the pressure, rounding errors can propagate especially if the internal energy is small. A third possible cause is related to the EOS model employed by RALEF-2D. The EOS model adopted in this work assumes LTE ionization throughout the entire simulation. This assumption breaks down at late times in the expansion when ionization and recombination processes cease to exist, leading to the

well-known "freezing" of charge states [65].

We note that the simulated domain (10 mm) is much smaller than the experimental flight path (∼1 m) and the assumption is made that neither the experimental or simulated ion energy distributions change significantly between the two distances. This assumption is supported by two arguments: (1) Within the simulated spatial scale the velocity profile attains its asymptotic, triangular shape before leaving the mesh, having converged to the late-time behaviour; (2) On the experimental side the aforementioned freezing of charge states will occur on a length scale similar to that of the simulation spatial scale [65] and, thus, that in our high-vacuum environment no significant changes over the remaining flight path will occur.

Keeping these remarks in mind, the results presented in this paper demonstrate that the single-fluid single-temperature approach implemented in RALEF-2D can (i) reproduce the general shape of the experimental ion energy distribution and (ii) provide a reliable prediction for absolute number of ions detected in the experiments.

2.6 Conclusion

We have undertaken a joint experimental and theoretical study of plasma expansion arising from Nd:YAG laser irradiation of tin microdroplets. The experimentally-recorded ion energy distribution is found to exhibit a complex, non-monotonic dependence on ion kinetic energy. Charge-state resolved measurements of the ion energy spectra reveal the existence of peaks centered near 2 keV in the Sn^{3+} – Sn^{8+} distributions. Two-dimensional radiation-hydrodynamic simulations performed using a single-fluid single-temperature approach are shown to reproduce the overall shape of the experimentally-recorded ion energy distributions and provide a reliable prediction for the absolute number of ions detected in the experiments. The existence of a peak in the experimental ion energy distribution near 2 keV is attributed to the formation of a quasi-spherical expanding shell at early times in the plasma expansion. Our interpretation of the plasma dynamics in terms of two distinct bursts of laser-induced ablation indicates that the observed ion energy distribution would in general be sensitive to the temporal profile of the laser pulse. The results of the present work are therefore specific for a Gaussian temporal profile with a laser intensity varying on the timescale of about 10 ns.

Acknowledgements

J. Sheil would like to thank A. Sunahara for sharing his simulation results and for useful discussions. We would also like to thank W. van der Zande for useful discussions. This project has received funding from European Research Council (ERC) Starting Grant number 802648. Part of this work has been carried out at the Advanced Research Center for Nanolithography (ARCNL), a public-private partnership of the University of Amsterdam (UvA), the Vrije Universiteit Amsterdam (VU), NWO and the semi-conductor equipment manufacturer ASML. Part of this work was carried out on the Dutch national e-infrastructure with the support of SURF Cooperative.

chapter 3

Energy- and charge-state-resolved spectrometry of tin laser-produced plasma using a retarding field energy analyzer

Lucas Poirier, Adam Lassise, Yahia Mostafa, Lars Behnke, Niels Braaksma, Luc Assink, Ronnie Hoekstra, and Oscar O. Versolato
Applied Physics B **128**, 053302 (2021).

We present a method to obtain the individual charge-state-dependent kinetic-energy distributions of tin ions emanating from a laser-produced plasma from their joint overlapping energy distributions measured by means of a retarding field energy analyzer (RFA). The method of extracting charge state specific parameters from the ion signals is described mathematically, and reinforced with experimental results. The absolute charge-state-resolved ion energy distributions are obtained from ns-pulse Nd:YAG-laser-produced microdroplet tin plasmas in a setting relevant for state-of-the-art extreme ultraviolet nanolithography.

3.1 Introduction

Laser-produced plasmas (LPP) are a topic of interest for their ability to efficiently produce extreme ultraviolet (EUV) and soft x-ray radiation. In state-of-the-art LPP nanolithography, the production of 13.5 nm EUV light is carried out by a high-repetition-rate tin plasma, driven by a $\sim 10^{10}$ W/cm^2, 50 kHz pulsed CO_2 laser. Multiply charged tin ions Sn^{8+} – Sn^{14+} are responsible for the EUV emission [8]: those ions display overlapping and narrow unresolved transition arrays (UTAs) around 13.5 nm in singly-, doubly- and triply-excited states [11]. Multilayer mirror optics (MLM) are used to collect and guide the EUV radiation emitted by the plasma. A MLM consisting of a series of alternating thin Mo and Si layers gives rise to a $\sim$70% reflection coefficient at 13.5 nm wavelength in a 2% reflection bandwidth [9, 10]. As the hot and dense LPP expands in the source chamber, the mirrors are subject to a gradual reduction of optical properties when fast tin ions and neutral atoms collide with their surfaces. Various processes such as implantation, sputtering and coating are responsible for the degradation of the overall efficiency of the optics. The type of damage is contingent on the kinetic energy and charge of the ions [15].

For this purpose the ion emission characteristics need to be understood, in particular the charge state, the kinetic energy and angular distribution. The quantification of ion emission is key to establish the energy balance of the different channels through which the energy of the LPP is dissipated.

A wide variety of ion diagnostic tools has been used in the literature, *e.g.*, electrostatic probes [22]; charge-integrated Faraday cups (FC) [13, 14]; charge-resolved retarding field analyzers (RFA) [18, 19]; electrostatic analyzers (ESA) [20, 21, 23, 24, 68]; and Thompson parabolas (TPS) [12]. Recently, the ARCNL ESA was cross-calibrated with a 4-grid FC, in an effort to produce high-accuracy charge-resolved ion spectra [68]. To study the angular dependence of the ion flow, such a spectrometer is not befitting given its dimensions, weight and particulars of its precise alignment to the plasma. This angular dependence can instead be more elegantly obtained using simple, robust and easy-to-align RFAs. Placing RFA detectors at various angles around the LPP allows for the simultaneous measurement of ion spectra, delivering valuable information on the angular dependence of the charge-energy spectra of the emitted ions. The prime shortcoming of the RFA type of detectors is their limited resolution when compared to the ESA. However, as we will show, the energy resolution obtained from commercially available RFAs (see Appendix) is sufficient to discriminate all here relevant charge states.

The present survey aims to develop and demonstrate methods to obtain charge-energy resolved spectra from a 4-grid Kimball Physics FC-73 RFA used to diagnose our tin laser-produced plasma. In these plasmas, a plurality of charge states and kinetic energies are

produced nearly instantaneously by the impact of the 10-ns-long pulses of a Nd:YAG laser onto a tin microdroplet. The experimental setup is first described. Next, the retarding field analysis approach is expounded and illustrated. Finally, a reconstructed charge-resolved RFA spectrum is presented.

3.2 Experimental setup

3.2.1 Laser-produced plasma (LPP)

Our LPP EUV source and auxiliary equipment has been described in detail before [27]. The components most relevant to this work are briefly recalled here, see also Figure 3.1. A tin reservoir is mounted on top of a vacuum chamber (10^{-7} mbar) and is kept at a constant temperature of 260 °C. From the reservoir, a nozzle produces a 22 kHz droplet train of pure, molten tin droplets traveling along the vertical axis of the vacuum chamber. The microdroplets, which have a diameter of 38 µm, first traverse a horizontal light sheet produced from a helium-neon laser. The light scattered off of the Sn droplets is detected by a photo-multiplier tube. The detected signal is frequency down-converted to 10 Hz to enable triggering of the laser system that creates the plasma. This Nd:YAG laser system produces pulses at a wavelength of 1064 nm and a time duration at full-width at half-maximum (FWHM) of approximately 10 ns. The beam is focused to a Gaussian spot (100 µm FWHM) onto the droplets in the center of the chamber. By using a half-wave plate and a thin-film polarizer, the laser pulse energy can be adjusted without affecting the spatial beam profile. In the following, the laser pulse energy was set to 90 mJ.

3.2.2 The retarding field energy analyzer (RFA)

The RFA is placed at a distance $d = 445$ mm from the LPP, at an angle $\alpha = 41.4\,°$ with respect to the direction of the incoming laser light, as depicted schematically in Figure 3.1. The entrance aperture of the RFA has a 5.0 mm diameter leading to a solid angle of $\Delta\Omega = 99$ µsr. The FC in which the ion current is collected, is biased to $U_{\text{bias}} = -30$ V while the suppression grid is held at $U_{\text{supp}} = -100$ V.

The retarding grid bias U_{ret} is varied in steps of 20 V between (set) voltages of 10 and 500 V with actual read voltages used in the analysis (and shown in selected traces in Fig. 3.2) in order to create a potential barrier to reject ions with an energy $E < zeU_{\text{ret}}$, with z the charge state of the incoming Sn^{z+} ion. At the maximum voltage the ion current signal in the FC was found to be fully suppressed. In the time traces of the ion current, the ringing at $t = 0$ in Fig. 3.2 is due to pick-up of the main laser's Q-switch and due to signal accredited to energetic photoelectrons emitted from the Faraday cup. The small noisy feature around 4 µs

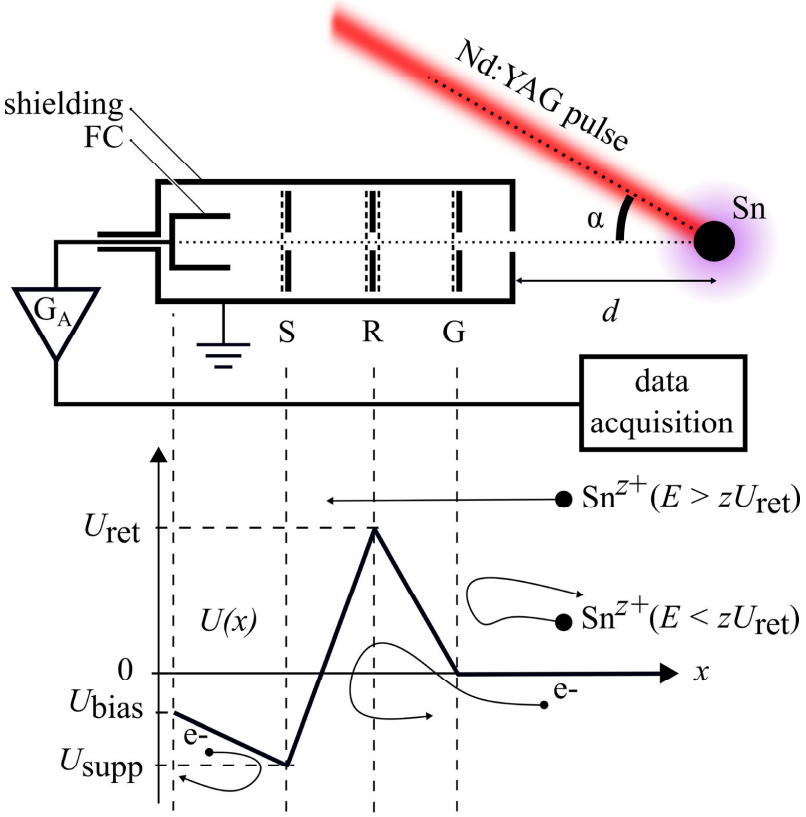

Figure 3.1: A tin droplet is converted to plasma using a 1064 nm, 10 ns-long Nd:YAG laser pulse. An RFA is placed at $d = 445$ mm from the plasma, at an angle $\alpha = 41.4\,^\circ$ with respect to the laser direction. Inside the RFA, the plasma ions traverse four grids: one grounding grid (G), two retarding grids (R) and a suppressor grid (S). The ion current on the FC is amplified by a fast trans-impedance amplifier (G_A). In the bottom panel the corresponding electrostatic potentials are schematically shown (black line). The behaviour of plasma ions, plasma electrons, and secondary electrons is also sketched.

is due to pick-up from the shadowgraphy laser system (see Section 3.3) and will lead to tiny high-energy ($\sim 5 - 8$ keV) features in the later spectra.

Each of the four grids has a geometrical transmission of 83%, as calculated from the pitch and the wire diameter. Assuming an alignment of the grids where the grids are spaced such that they have minimal geometric overlap but the same orientation, the total transmission may be estimated to be 41%. This figure was previously found to be consistent with an ion current comparison between the RFA and a grid-less Faraday cup [68].

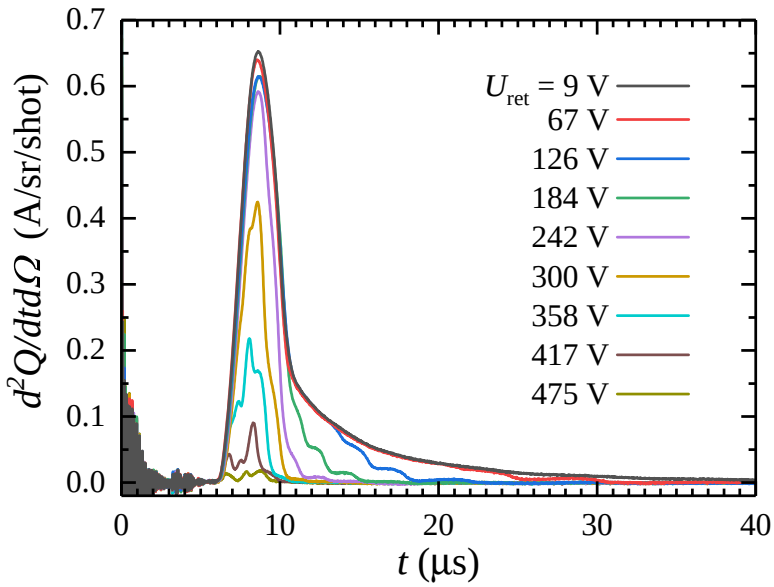

Figure 3.2: Typical ion current traces as recorded by the RFA for different values of retarding voltage. Smooth steps appear in the time-of-flight traces as the retarding voltage is increased.

We convert the RFA time-of-flight (ToF) current traces to a voltage using a trans-impedance amplifier with a gain of 25 kV/A and a bandwidth of 25 MHz. The amplifier consists of two stages. The first, a trans-impedance stage with 5 kV/A gain, is based on a high speed operational amplifier (Texas Instruments OPA847) with a low input current noise of 2.5 pA/$\sqrt{\text{Hz}}$ and a gain bandwidth product of 3 GHz. This stage is followed by a non-inverting output stage (Texas Instruments OPA691) with tenfold amplification. The output impedance of the amplifier is 50 Ω, matched to the load of the amplifier, giving rise to the 25 kV/A gain. Due to the fast response of the amplifier, deconvolution of the measured signal from the measurement electronics is not necessary to accurately reflect the ion current impinging upon the collector.

In a previous experiment [68], we confirmed the gain of the trans-impedance amplifier to be equal to its expected value of 25 kV/A. Measured ion transients have a typical duration on the order of several 10 μs. Our amplifier, providing an amplified capacitive readout of the RFA, was designed accordingly to have a fast current ramp-up (∼ ns) and a particularly slow (negative) charge re-flow (∼ ms).

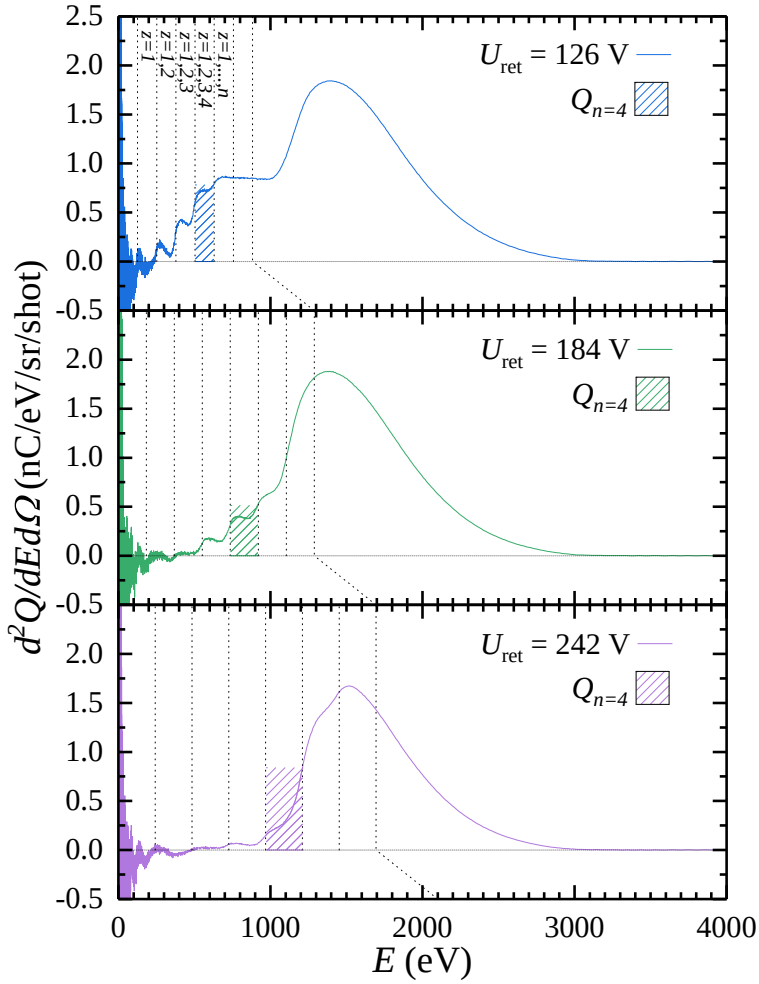

Figure 3.3: Three sample ion current transients for non-consecutive U_{ret} values are presented in the energy-domain. The charge Q_n collected in the n-th energy bin of $d^2Q(E)/dEd\Omega$, spanning the range from $E = neU_{ret}$ to $E = (n+1)\,eU_{ret}$ (dotted vertical lines), is pictured by the hatched area. It contains ions with charge state $z \leq n$.

3.3 Method of data processing

The post-processing of RFA data aims at constructing the charge-resolved ion energy distributions from the ToF current measurements taken at various retarding voltages. First,

average ion currents are calculated for each retarding voltage setting. In the experiments presented here, 200 shots are recorded for each retarding voltage value. Outliers, attributable to limited laser-to-droplet alignment accuracy, are removed before averaging. For this purpose, concurrently recorded shadowgraphic images of the tin target are used. The shadowgraphy imaging setup is described in earlier studies (see, *e.g.* [27, 91]) and enables obtaining the velocity of the plasma-propelled liquid mass. This propulsion velocity is a convenient metric for laser-to-droplet alignment [92]. For each shot, we extract the propulsion speed; in the rest of the analysis we only consider the shots where the propulsion speed is comprised within ±5% of the most likely propulsion speed. For the presented data, about 75% of the shots are sufficiently well aligned.

The baseline of the signal is evaluated at late times (> 100 µs), and is subtracted from each of the average current transient to correct for any potential drift in the baseline. This baseline subtraction also provides a first-order correction for re-flow current due to the capacitive readout (with the re-flow occurring at ∼ ms time scale). The ion current is averaged over the small solid angle defined by the FC aperture and its distance to the plasma.

$$\frac{d^2Q(t)}{dtd\Omega} \approx \frac{dQ(t)}{dt}\frac{1}{\Delta\Omega}. \tag{3.1}$$

We omit the solid angle double differential notation for clarity in the following.

The time domain ion current $dQ(t)/dt$ is next expressed as energy domain current $dQ(E)/dE$, given that the RFA selectively transmits ions based on their charge state and energy E, through

$$\frac{dQ(E)}{dE} = \frac{dQ(t)}{dt}\frac{dt}{dE}. \tag{3.2}$$

For each retardation voltage U_{ret} applied, we split the ion current traces in the energy domain into energy bins of width eU_{ret}. We assign the index n to the energy bin spanning neU_{ret} to $(n+1)\,eU_{\mathrm{ret}}$, centered at $E_n = \left(n+\frac{1}{2}\right)eU_{\mathrm{ret}}$, containing a charge Q_n

$$Q_n(E_n) = \int_{neU_{\mathrm{ret}}}^{(n+1)eU_{\mathrm{ret}}} \frac{dQ\,(E)}{dE}dE. \tag{3.3}$$

The charge contribution to the discretized ion energy distribution $dQ_n(E)/dE$ from the n-th bin is given by

$$\frac{dQ_n(E_n)}{dE} \approx \frac{Q_n(E_n)}{\Delta E} = \frac{Q_n(E_n)}{eU_{\mathrm{ret}}}, \tag{3.4}$$

with the integration region $\Delta E = (n+1)eU_{\mathrm{ret}} - neU_{\mathrm{ret}} = eU_{\mathrm{ret}}$. The discretized ion energy

distribution is constructed considering data from all scanned U_{ret} values and is transformed into a continuous function by linear interpolation.

Each bin n contains contributions from charge states $z = 1$ through $z = n$. Ions in charge state $z = n + 1$ that pass the retardation grid with its voltage U_{ret} will end up in bin $n + 1$ (see Fig. 3.3). Thus,

$$Q_n = \sum_{z \leq n} Q_n^z. \tag{3.5}$$

(We note that the individual ion charge Q_n^z, with superscript z denoting the charge state, is related to ion number N_n^z through $Q_n^z = zeN_n^z$.) The identity Eq. (3.5) enables to iteratively obtain charge-state-resolved energy distributions $dQ^z(E)/dE$. Starting with $z = 1$, we can take directly $dQ^{z=1}/dE = dQ_{n=1}(E)/dE$ as it is the only ion charge contributing to bin $n = 1$. The energy spectrum of the next charge state $z = 2$ is obtained subtracting the now known spectrum of the $z = 1$ charge from the $n = 2$ bin, *et cetera*:

$$\frac{dQ^z(E)}{dE} = \frac{dQ_{n=z}(E)}{dE} - \frac{dQ_{n=z-1}(E)}{dE}. \tag{3.6}$$

The energy spectrum of any ion charge state can thus be obtained from this bottom-up procedure.

Once all of the $dQ^z(E)/dE$ terms are calculated, the charge-integrated spectrum $dQ(E)/dE$ is assembled:

$$\frac{dQ(E)}{dE} = \sum_{z \leq z_{\max}} \frac{dQ^z(E)}{dE} = \frac{dQ_{n=z_{\max}}(E)}{dE}. \tag{3.7}$$

Here the maximum ion charge $z_{\max}$ (and with it, the maximum bin number $n_{\max}$) is introduced to truncate the iterative procedure. Its value should be set to be no larger than the maximum charge state expected to be emitted from the plasma in significant numbers. Setting $z_{\max}$ to a larger value will lead to increased post-processing computational time and the energy distributions of the highest charge-states will in any case be dominated by noise. If the maximum charge state $z_{\max}$ is set right, the charge-integrated spectrum dQ/dE determined through Eq. (3.7) will overlap closely with the corresponding charge-energy spectrum measured without any retarding potential applied (or, equivalently, for the lowest value of U_{ret} applied), transforming the full current via Eq. (3.2).

3.4 RFA spectrum

Next we apply the method to the case at hand. A maximum charge state of $z = 7$ was determined to describe sufficiently well the ion currents for the experiment presented here. Higher

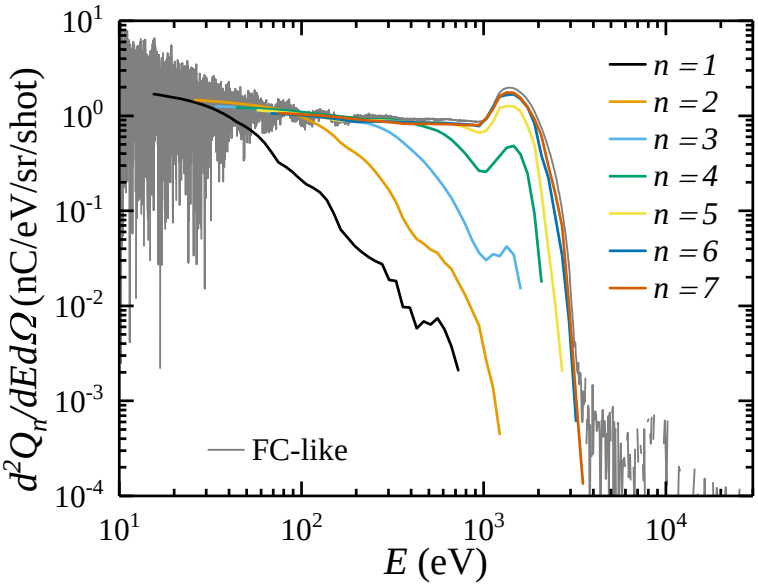

Figure 3.4: Cumulative energy distributions; the n-wise spectra (n =1–7) are shown in different colors. The highest-index cumulative distribution $dQ_{n=7}/dE$ overlaps with the charge-integrated FC-like spectrum (gray line).

charge states are also present in the hot and dense phase of the plasma, as is known from spectroscopy in the extreme ultraviolet range (see *e.g.* Refs.[11, 44, 93]), where spectroscopic features are assigned to Sn^{z+} ions in higher charge states up to $z = 14$. However such higher charge states recombine with plasma electrons close to the laser-matter interaction zone, shifting the charge state distribution down to produce the Sn^{z+} ions in lower charge states as observed here.

Figures 3.4 and 3.5 show the cumulative [Eq. (3.4)] and charge-state-resolved energy distributions [Eq. (3.6)] of Sn^{z+} ions of the current experiment, respectively. In both figures, the gray line corresponds to a charge-integrated, Faraday cup type (FC-like) spectrum calculated from the corresponding time-of-flight trace via Eq. (3.7). Specifically, the FC-like spectrum is derived from the RFA current measured for the lowest retardation grid voltage of $U_{\mathrm{ret}} = 9$ V. Note that the RFA and FC-like data were thus taken with the same device. As there is no significant contribution to the current trace of energies below $eU_{\mathrm{ret}} = 9$ eV, the FC-like signal closely resembles the total current that would be measured from a regular Faraday cup without any retardation voltage.

In Figure 3.5, the dashed gray line indicates the noise level of the FC-like spectrum,

evaluated using the standard deviation of the ion current at late times (typically between 100–200 µs where there are no discernible features in the ToF signal). It can be shown analytically that the noise level scales with $E^{-3/2}$ considering the dt/dE term in Eq. (3.2) ($dE/dt \sim d(1/t^2)/dt \sim 1/t^3 \sim E^{3/2}$) and assuming white noise in the time-of-flight traces with a time-independent noise amplitude.

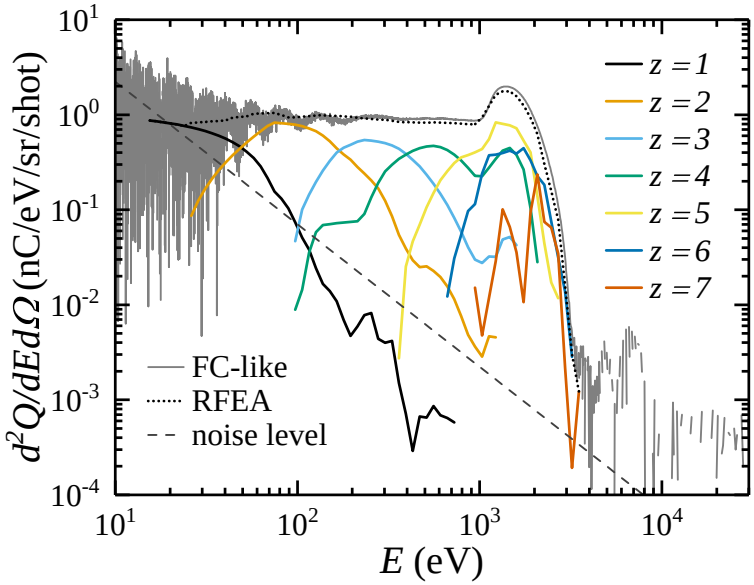

Figure 3.5: Charge-resolved energy distributions; the z-wise spectra (z =1–7) are shown in different colors. The sum of the charge-resolved spectra dQ/dE overlaps with the charge-integrated FC-like spectrum (gray line). The estimated noise level of the FC-like current trace is pictured by the transversal gray dashed line ($\propto E^{-3/2}$).

The FC-like spectrum exhibits a high-energy peak between 1 and 2 keV. This high-energy peak has recently been attributed to a quasi-spherical expanding shell formed at early times in the plasma expansion into which subsequent hotter plasma is bunched - an effect that is characteristic to temporally Gaussian-shaped laser pulses [94].

In Figure 3.5 the charge-integrated spectrum dQ/dE determined through Eq. (3.7) is found to closely match with the corresponding charge-energy spectrum measured without any retarding potential applied (FC-like), supporting the robustness of the method as well as the choice of the largest considered charge state $z_{\max} = 7$. Ions with higher charge may still be present but at negligible quantities. The individual charge-energy spectra follow trends similar to those seen previously using an electrostatic time-of-flight analyzer [68, 94], with in particular the higher charge states bunching up to form the aforementioned high-energy peak.

3.5 Conclusion

A method is presented to interpret data obtained from a retarding field analyzer (RFA). The process enables one to obtain the individual charge-state dependent kinetic-energy distributions of tin ions emanating from a laser-produced plasma from their overlapping energy distributions. Our method uses the fact that ions with the same energy but different charge state are selectively filtered out in the time-of-flight current signal by the applied retarding potential, which is scanned to obtain complete energy distributions. The selective filtering enables obtaining the individual charge state energy spectra in an iterative manner. This so-called "bottom-up" approach starts out from identifying the energy intervals where only a single -the lowest- charge state $z = 1$ contributes. Subsequently, the higher charge states ($z = 2, 3$, *et cetera*) are step-wise identified.

Applying our method to the obtained data from ns-laser-pulse impact on a tin micro-droplet, we find that the individual charge-energy spectra follow trends similar to those seen previously using an electrostatic time-of-flight analyzer, with a characteristic high-energy peak comprising bunched charge states.

The understanding of complete spatial ion emission characteristics is crucial for establishing the momentum and energy balance of the LPP, as well as for designing ion "debris" mitigation schemes in future sources of EUV light for nanolithography. Our bottom-up method will facilitate obtaining angularly resolved charge-energy distributions from RFA measurements, as the robust and compact RFAs can conveniently be arranged around an LPP vacuum vessel.

Acknowledgements

The authors thank Duncan Verheijde for his support in understanding and improving the RFA electronics. They also thank Jorijn Kuster for designing efficient and user-friendly software interfaces for our experimental setups. This work has been carried out at the Advanced Research Center for Nanolithography (ARCNL), a public-private partnership of the University of Amsterdam (UvA), the Vrije Universiteit Amsterdam, the Dutch Research Council (NWO) and the semiconductor equipment manufacturer ASML. This project has received funding from European Research Council (ERC) Starting Grant number 802648. This publication is part of the project New Light for Nanolithography (with project number 15697) of the research programme VIDI which is (partly) financed by the Dutch Research Council.

Appendix : Energy resolution

To assess the energy resolution of an RFA we next analyze the energy-derivative of the dQ/dE traces as obtained from the oscilloscope using Eq. (3.2). This derivative dQ^2/dE^2 exhibits Gaussian peaks originating from the smooth, step wise increment of contributing charge states to the next bin (*cf.* Fig. 3.3) as is clear from Fig. 3.6.a, where $d^2Q(E)/dE^2$ is shown for a retarding voltage of 106 V. The widths of these Gaussian peaks give access to the experimental resolution of the RFA under actual operating conditions. Peaks from $n = 3$ to $n = z_{\max} = 7$ can reliably be fitted with Gaussian functions. The widths are retrieved from the fits, while obvious outliers are removed. Figure 3.6.b presents the thus obtained widths ΔE, defined as the FWHM of the Gaussian peaks. As predicted by Sakai *et al.* [95], we find a constant ratio $\Delta E/E$ here with a value of approximately 8%. Given the design of the aperture and grids of our RFA, Sakai *et al.* predict a smaller resolution of 2% for an idealized 2-grid RFA impinged on by a single-isotope, single-charge state, mono-energetic beam. We attribute the difference between the predicted and experimentally obtained resolution mainly to the presence of a wide range of tin isotopes and charge states, and to effects from the additional grids and their relative alignment.

The energy resolution can also be derived through a separate method which yields a consistent resolution of $\Delta E/E \approx 9\%$. This method is based on taking the difference between traces obtained from consecutive values of the retarding field U_{ret}^{i+1} and U_{ret}^{i}: $S_i(E) = dQ_{i+1}(E)/dE - dQ_i(E)/dE$, where i stands for the index of the U_{ret} increments. S_i also presents peaks centered at energies that are multiple of $E_i = \frac{1}{2}e(U_{\text{ret}}^{i+1} + U_{\text{ret}}^{i})$. In Figure 3.6.c, vertical lines depict multiples of E_i on the energy axis, where contributions from the individual charge states manifest. If the retarding voltage increment $U_{\text{ret}}^{i} - U_{\text{ret}}^{i+1}$ is small with respect to the local value of the resolution ΔE, the convolution of the step size with the energy resolution provides Gaussian peaks. Fitting those peaks enables recovering energy resolution $\Delta E(E)$. In Figure 3.6.b, the widths of the S_i peaks corresponding to $z = 2$ and 3 are shown to be slightly offset (at ~ 20 eV) from the results from the more detailed first method, as was expected given that $U_{\text{ret}}^{i+1} - U_{\text{ret}}^{i} = 20$ V in our scans, and to follow a similar slope $\Delta E/E$ yielding the instrument resolution.

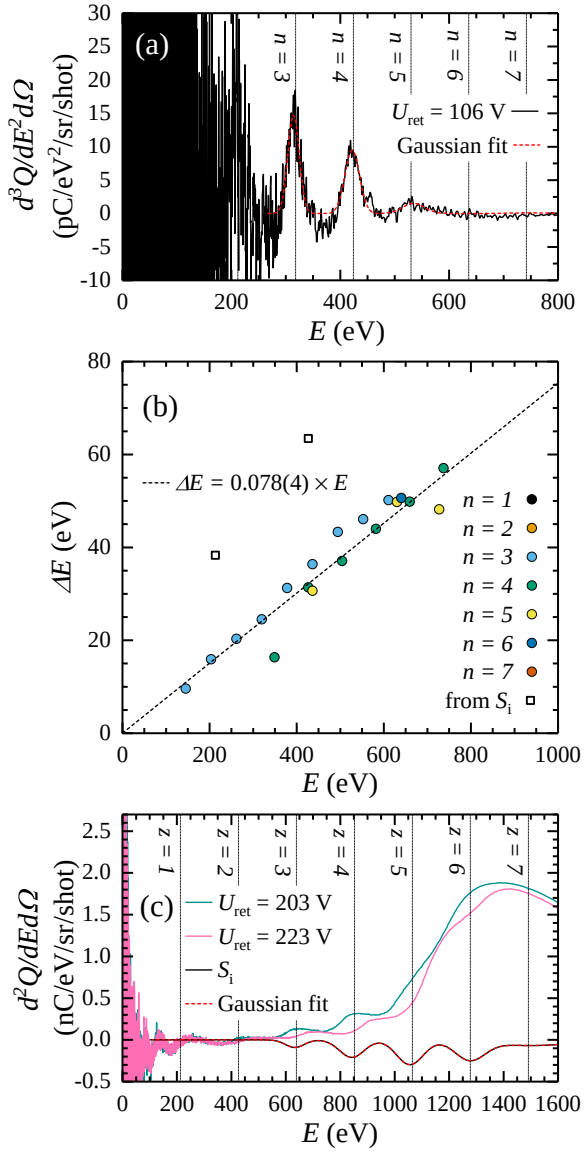

Figure 3.6: In panel (a) the derivative of the energy-domain ion energy distribution (black line) is fitted with Gaussian peaks (red dashed line) centered around energies equal to multiples of the retarding voltage eU_{ret}. The data below 250 eV was not included in the fitting range because of the low signal-to-noise level. The fitted widths of all valid peaks are reported in panel (b) (colored circles), where a linear trend is observed and fitted (dashed black line); the relative energy resolution $\Delta E(E)/E$ is found to be 0.078(4). In panel (c), the differential signal S_i (black line) and its parent ion distributions (teal and pink lines) are represented. S_i shows peaks around multiples of the average retarding voltage E_i. Each differential peak corresponds to a specific charge state z; S_i is also fitted with a 7-Gaussian array (red dashed line). Accurately fitted widths are also reported in panel (b) (black squares).

chapter 4

Strongly anisotropic ion emission in the expansion of Nd:YAG-laser-produced plasma

Lucas Poirier*, Diko J. Hemminga*, Adam Lassise, Luc Assink, Ronnie Hoekstra, John Sheil, and Oscar O. Versolato

Physics of Plasmas **29**, 123102 (2022).

We present results from a combined experimental and numerical simulation study of the expansion of a laser-produced plasma into vacuum. Plasma is generated by Nd:YAG laser pulse impact (laser wavelength $\lambda = 1.064\,\mu m$) onto tin microdroplets under conditions relevant for extreme ultraviolet lithography. Measurements of the ion kinetic energy distributions under a multitude of angles reveal strongly anisotropic emission characteristics, in close agreement with two-dimensional radiation-hydrodynamic simulations. The angle-resolved ion spectral measurements further enable the accurate prediction of the plasma propulsion of the laser-impacted droplet.

* LP and DH contributed equally to this chapter as part of their PhD theses. LP conducted the experimental work and DH the numerical and theoretical work.

4.1 Introduction

State-of-the-art nanolithography relies on 13.5 nm extreme ultraviolet (EUV) light that is generated from laser-produced tin plasma (LPP) [7, 8, 96]. Expansion of the hot and dense tin plasma may hinder EUV source operation in several ways, notably in the form of fast plasma ions that may damage or coat EUV optics [15]. Effective mitigation schemes are required to rid the EUV generation of such adverse processes. These mitigation schemes may, *e.g.*, involve buffer gases aimed to stop and remove the ionic debris, or use strong magnetic fields to guide the tin ions [15, 97]. Designing such mitigation strategies benefits from the understanding of the driving mechanisms of the plasma expansion in the absence of any such mitigation effects.

Analytical models of plasma expansion into the vacuum have previously been developed [3, 98, 99], also were applied to the specific case of tin laser-produced plasma [2, 14]. More recently, two-dimensional radiation-hydrodynamics simulations, using a single-fluid single-temperature approach, were performed with the aim of further clarifying the expansion physics as it was found that the strongly simplified analytical models were unable to fully capture the expansion. The simulations were shown to accurately reproduce the ion energy distributions as obtained from experiments in a single direction: under a 60° angle backwards towards the laser [94]. A prominent peak in the experimental ion energy distribution was attributed to the formation of a quasi-spherical expanding shell at early times in the plasma expansion [94]. The interpretation of the plasma dynamics in terms of a complex interplay between two directional bursts of laser-induced ablation [94], requiring that the plasma expansion and the resulting ion kinetic energy spectra are highly anisotropic.

The importance of a thorough understanding of tin LPP angular ion emission motivated several detailed experimental studies on the topic, using electrostatic probes [100, 101], Faraday cups [12, 65], electrostatic analyzers [21, 65, 102], retarding field analyzers[19], and Thompson parabolas [12]. Many studies observed anisotropy in the charge-integrated [12, 65, 100, 103, 104] and in the charge-resolved ion emission into a buffer gas [21, 102]. Kools *et al.* [103] and others[105, 106] produced analytical expressions for the integral ion current, which were later built upon [107] to derive the angular dependence of the ion charge yield. This angular dependence was found to resemble a cosine power law [65, 107] (also see Qin *et al.* [104]). Brandstatter *et al.* [100], O'Connor *et al.* [108], and Giovannini *et al.* [21] found clear dependencies of the charge-resolved average ion energy and of the average peak velocity on the emission angle, providing important insights. Thus far, however, no combined absolute angle- and charge-state-resolved kinetic energy measurements have been performed on a tin-microdroplet-based plasma freely expanding into the vacuum.

We present a study of angle-, energy-, and charge-resolved absolute ion yields, using compact retarding field analyzers (RFAs) set up under several angles. Our measurements are

compared to single-fluid radiation-hydrodynamics simulations performed using the RALEF-2D code. In the following, first, we briefly describe the experimental setup and methods used as well as the corresponding RALEF-2D simulations. This is followed by a detailed discussion of the ion emission anisotropy and the features and trends observed in the ion spectra comparing the experiments with simulations supported by analytical theory. We define several relevant metrics related to the ion emission (ion number, momentum, energy), and report their value. Lastly, we utilize the measured ion momentum to accurately predict the propulsion speed of the laser-impacted droplets over a wide experimental parameter range.

4.2 Experiments

4.2.1 Experimental setup

The experimental setup is described in detail in earlier work [27]. Here, we recall the main elements. A tin tank is mounted on top of a vacuum chamber ($\sim 10^{-7}$ mbar), and is kept at 260°C — above the melting temperature of tin. The tank is pressurized with argon gas to push the molten tin through a nozzle. Tin droplets with a well-defined diameter of $d_{\mathrm{drop}} = 27\,\mu\mathrm{m}$ are dispensed by the nozzle at kHz frequencies (in Subsection 4.4.3 also $d_{\mathrm{drop}} = 17\,\mu\mathrm{m}$ droplets are discussed). The microdroplets next intersect a horizontal laser sheet produced by a helium-neon laser beam coupled into a cylindrical lens. Light scattered by the droplet when traversing the laser sheet is collected by a photomultiplier tube (PMT). The PMT signal is down-converted to 10 Hz; this down-converted signal is used as trigger to synchronize the impact of a seeded 10 Hz Nd:YAG laser pulse with the droplets. The laser pulses have a wavelength of 1064 nm, a Gaussian spatial profile with a full width at half maximum (FWHM) of 100 µm, and a Gaussian temporal profile with a FWHM of 10 ns. The pulse energy can be tuned using a $\lambda/2$ waveplate in combination with a polarizer.

FC73-A Faraday cups (FCs) from Kimball Physics were used to characterize the charge and energy of the ions emitted from the LPP. FCs record the ion current as a function of the time of flight (ToF). Ion kinetic energies are calculated using the time of flight and the length of flight d of ions, assuming ballistic motion. The time-of-flight ion current is converted to a time-dependent voltage thanks to a trans-impedance amplifier (600 MHz Keysight Infiniium) with a broad bandwidth of 25 MHz ($\mathrm{G_A}$ in Figure 4.1(b)). When the output impedance of our oscilloscope is matched with that of the amplifier (50 Ω), the amplifier gain becomes 25 kV/A. Further information can be found in Poirier *et al.* [109]. The detectors feature four grids, namely a reference grounding grid G, two retarding grids $\mathrm{R_1}$ and $\mathrm{R_2}$, and a suppressing grid S (see Figure 4.1(b)). The suppressing grid is biased negatively ($U_{\mathrm{supp}} = -100\,\mathrm{V}$) in order to repel back into the Faraday cup any secondary electrons produced from the surface

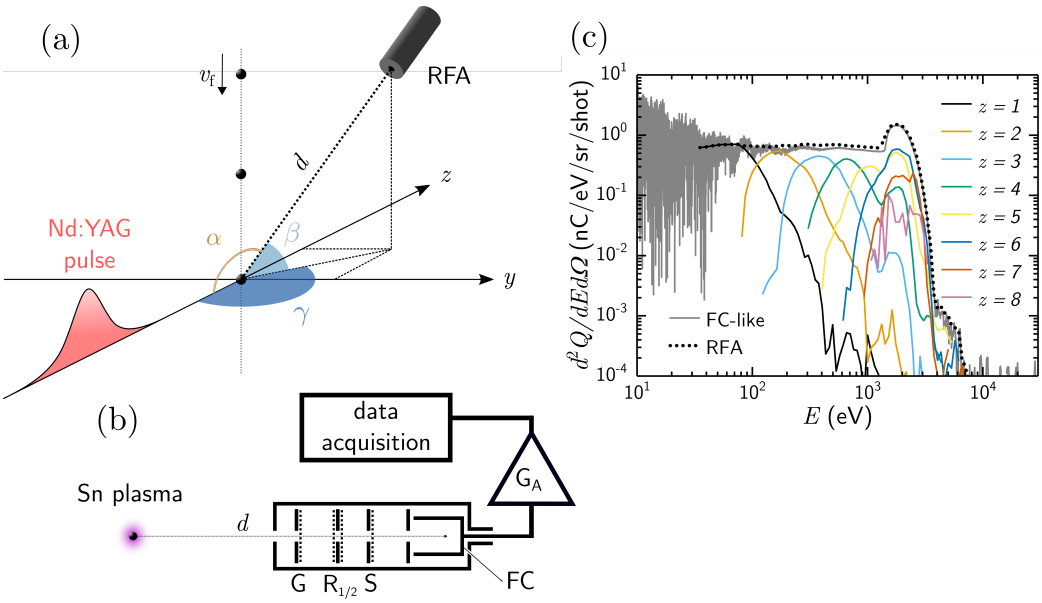

Figure 4.1: Sketch of experimental setup. (a) Droplets travel with velocity v_f until they are illuminated by the Nd:YAG laser pulse. The position of a RFA is defined by its distance to the LPP (d) and the angle (α) between the direction towards the RFA and the negative z-axis, the symmetry axis of the incoming laser pulse. This angle α calculated from the azimuth (γ) and the elevation (β) of the RFA with respect to the laser axis. (b) The main elements of the RFA are shown; four grids (G, R_1, R_2 and S) are located in the path of the tin ions. The ion current in the Faraday cup (FC) is amplified (denoted by G_A) and recorded by an oscilloscope. (c) A sample charge-resolved ion energy spectrum taken with an RFA is presented; the sum of the different charge states (z = 1–8, black dotted line) overlaps with a charge-integrated spectrum (gray line; "FC-like" [109]) taken at the same position as the RFA spectrum.

of the Faraday cup. The cup itself is biased ($U_{\text{bias}} = -30\,\text{V}$) to prevent plasma electrons from entering the cup. The electrostatic field applied to the retarding grids of the device is scanned to unravel the charge state of detected ion, in the so-called "retarding field analysis" (RFA) mode. The two retarding grids share the same positive potential U_{ret} and are separated by a 500 µm gap. Scanning U_{ret} from 0 V up to 1 kV, an increasing amount of positively charged ions with charge ze and energy E emanating from the plasma are repelled when $E < zeU_{\text{ret}}$. An iterative post-processing of the ion currents allows for the unravelling of charge-resolved ion energy spectra. The post-processing scheme was explained in detail in Ref. [109], an earlier study in a very similar context.

Seven RFAs were placed at various angular positions around the plasma. The angular position of the RFAs with respect to the vacuum chamber is described by their elevation (β) and azimuth (γ) with respect to the laser axis, as illustrated in Figure 4.1(a) and listed in Table 4.1 in the Appendix. The cylindrical symmetry of the laser-droplet system enables defining the direction of the RFAs by a single angle α through $\alpha = \cos^{-1}(\cos(\gamma)\cos(\beta))$. The aperture of an RFA has a diameter of 5 mm and is located at a distance d from the point-like plasma, defining the solid angle of the aperture $\Delta\Omega$ (see Table 4.1 in the Appendix). It was shown previously in Ref. [68] that an RFA with four maximally misaligned grids has a transmission of 41%. We later obtained from detailed simulations [110], that the transmission of the four-grid stack intricately depends on the co-alignment of the grids, the energy of the ions, and the electrostatic bias on each grid. From our simulations, stack transmission was found to range between 41% (in case of maximally misaligned grids, consistent with our previous results [68, 109]) and 82% (in case of geometrically overlapping grids with maximum alignment). In the following, we therefore take a representative and average transmission of 60% for all RFAs, with a systematic error of 20% covering the range of possible extreme cases of grid alignment.

4.2.2 Experimental methods

The so-called bottom-up method is used to derive charge-resolved ion spectra from ion time-of-flight current traces via a retarding voltage scan. The process is described in detail by Poirier *et al.* in Ref. [109]. Here, U_{ret} is set to 61 equally spaced values between $U_{\text{ret,min}} = 0\,\text{V}$ and $U_{\text{ret,max}}$, depending on the maximum retarding voltage required to negate the total ion current. Indeed, $U_{\text{ret,max}}$ must be at least equal to $E_{\text{max}}/z_{\text{max}}$, where E_{max} and z_{max} are, respectively, the highest ion energy and charge state detected for a given experiment. In the presented experiment, a maximum retarding voltage of 1 kV was found to be adequate. We record ion currents for several hundred laser shots for each of the retarding voltages and use the average ion current throughout the analysis, as to enhance the signal-to-noise ratio.

Outlying single-shot ion currents are discarded when the velocity of the leftover liquid tin target observed via simultaneous single-shot shadowgraphic imaging falls beyond ±5% of the average observed target velocity (*cf.* Ref [27, 83]).

A typical ion energy distribution measured with the aforementioned experimental parameters is presented in Figure 4.1(c); here the laser energy was set to 99 mJ and the droplet size to 27 µm. The laser transmission of the vacuum chamber input window was measured to be 97%. The charge-state-resolved distributions ($z = 1$–8) of charge $d^2Q_z/dEd\Omega$ are presented and the sum of contributions from all charge states (black dotted line) overlaps with a Faraday-cup-like charge-integrated measurement (gray line) recorded separately, but at the same detection angle α. In the following, we present the total ion energy number distributions $d^2N/dEd\Omega$ — representing the hydrodynamic mass flow — by accounting for the individual charge states Q, using the charge-state-resolved data [94]. A confidence interval is introduced to account for the systematic errors in estimating ion measurements. A first contribution to this confidence interval covers the influence of late-time baseline subtraction, where we follow Ref. [109]. A second contribution accounts for the 20% systematic error on the transmission of the four RFA grids (*cf.* section 4.2.1). In the following, the confidence interval based on these two effects is displayed in figures and taken into account wherever relevant metrics are presented.

4.3 Radiation-hydrodynamics simulations

4.3.1 RALEF-2D

The RALEF-2D code and its application to the case of tin laser-produced plasma was presented in detail in earlier publications on plasma expansion [94] and propulsion of the remaining mass [111]. RALEF (Radiation Arbitrary Lagrangian-Eulerian Fluid dynamics) is a two-dimensional (2D) radiation-hydrodynamics finite element solver fit for the simulation of laser-produced plasmas. The code solves the single-fluid and single-temperature hydrodynamics equations with inclusion of energy transport by thermal conduction and radiation.

The solution of the radiation transport equation is based on spectral absorption coefficients generated with the THERMOS code [87] and the equation-of-state (EOS) of tin used is known as the Frankfurt EOS (FEOS) [89]. In the presented simulations the so-called hybrid model for laser light propagation is employed [112]. It accounts for laser absorption, reflection, and refraction in the corona of the plasma. With this choice we operate a model of laser propagation that is identical to our last work, on droplet propulsion and deformation [111], but one that is more complete when compared to our previous work on plasma expansion [94].

4.3.2 Application of RALEF-2D

The experimental laser-droplet parameters serve as input to the radiation-hydrodynamics simulations with RALEF-2D. The presented simulations are performed using a 1064 nm laser pulse with a Gaussian temporal profile with a FWHM of 10 ns, similar to the simulation presented in Hemminga *et al.* [94]. In this work, the spatial laser profile is modeled by a Gaussian of 100 µm (FHWM) and the droplet diameter is set to 27 µm. In fact, the experimental spatial profile of the laser is an Airy disk, which we approximate to be a Gaussian profile in the simulation; we set the simulated pulse energy to be 90 mJ so that the simulated laser pulse has the same energy within a radius of FWHM/2. The radiation-hydrodynamics simulations are performed on a two-dimensional computational mesh of quadrilateral cells. We chose a domain similar to our previous work [94]: a half-disk geometry with a radius of 10 mm. The cylindrical symmetry axis is defined as reflective, while the curved boundary of the half-disk allows for free-outflow of material. This outflow is used for extraction of the numerical ion energy distributions in this work.

4.3.3 Ion distributions from simulation

The method for extracting ion energy distributions $d^2N/dEd\Omega$ from the simulated hydrodynamic mass flow is based on allocating the outflowing mass to predefined kinetic energy and angle intervals. It has been detailed in Ref. [94]. This allocation is based on the magnitude and direction of the velocity of the outflowing mass, as related to kinetic energy and angle, respectively. In the presented simulations, 360 exponentially scaling energy bins are used over the interval between 1 and 20 keV. In angular space, 180 equally sized bins are used over 180°. The angularly resolved ion kinetic energy distributions are processed in three steps. Supplementing the analysis in our previous work [94], we first take an average over a set of nine simulation runs with identical input parameters. Secondly, similar to our previous work, we average the distributions over an angular range of 10° around the experimental angles, *i.e.f* $\alpha \pm 5°$. We weight the average calculation with the respective solid angles of each bin. The angular distributions are based on these data and have an effective 10° running average applied. Thirdly, we apply a convolution by the experimental energy resolution. The energy resolution used matches that of the RFA detectors and is equal to $\Delta E/E = 8\%$, as determined in an earlier study [109]. The calculation is based on a convolution of the ion kinetic distribution histogram with a Gaussian function with FWHM $= \Delta E$ and an area of unity.

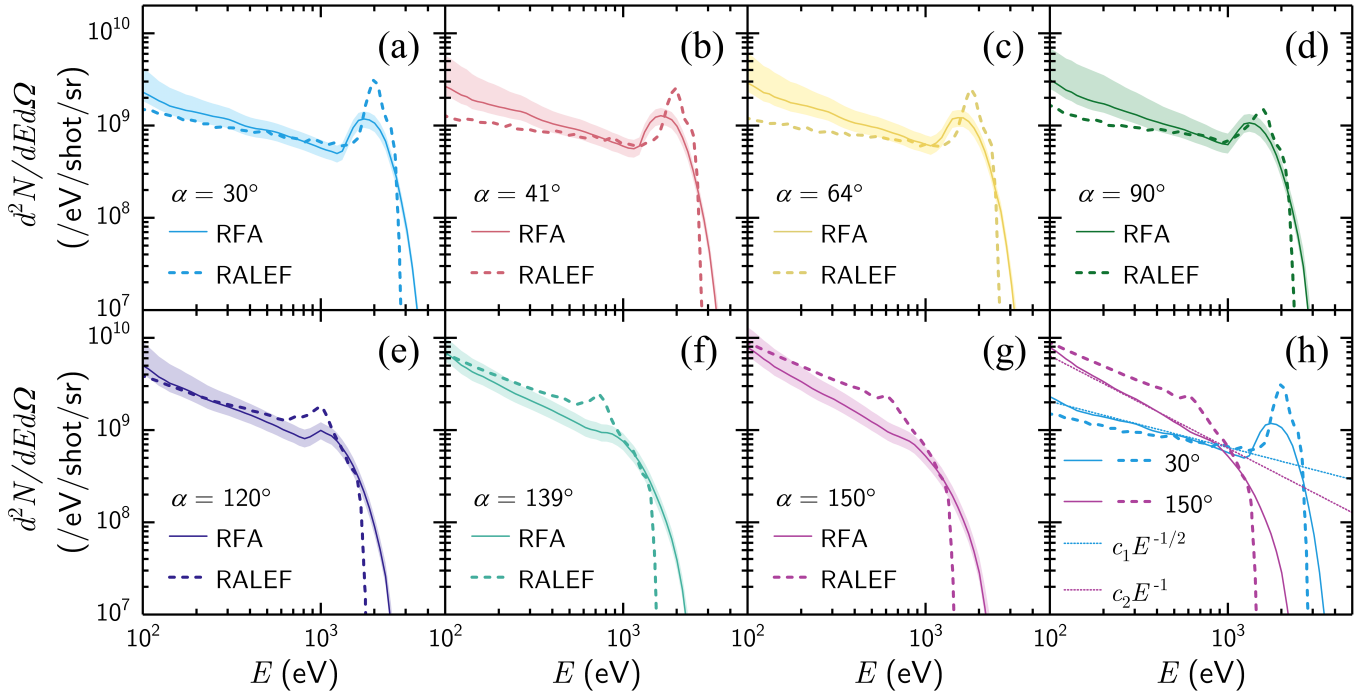

Figure 4.2: Ion energy distributions measured by the RFAs (solid lines), and modeled by RALEF-2D (dashed lines) are separately shown for each of the seven measurement angles (a–g). Error bars discussed in Section 4.2.1 are depicted by the colored shading. In the bottom-right panel (h), the RFA and RALEF-2D spectra are overlapped for a small and large angle to emphasize the shifting spectral features; the dotted lines show power laws for the front ($\alpha = 30°$) and back ($\alpha = 150°$) side (see main text).

Figure 4.3: Two-dimensional profiles of ion speed $|v|$ (upper-half panel) and mass density ρ (lower-half panel) are presented for different time steps throughout the LPP expansion. The fraction of absorbed laser light at each time step is pictured in the bottom-right corner inset. White dotted lines indicate the positions of the seven RFAs.

4.4 Results and discussion

4.4.1 Ion emission anisotropy

Total ion energy distributions $d^2N/dEd\Omega$ by RFAs at seven different angles with respect to the laser axis, are presented in Figure 4.2 (solid lines in (a–g)). First, a high-energy peak can be identified in the experimental distributions in Figure 4.2, as also previously reported [68, 94, 109]. The local maximum of this peak lies between 500 and 1000 eV depending on the detection angle α and is most prominent in the spectra from the front side ($\alpha \leq 90°$). Spectra at the back side ($\alpha > 90°$) do not strongly feature a peak and instead exhibit a near-monotonic decrease of ion number for increasing energy. In relative terms, the front side experiences the emission of a higher number of high-energy ions ($E > 400$ eV) than the back side, which collects a higher number of low-energy ions ($E < 400$ eV). For all angles, the spectra exhibit a power-law type fall-off up to the peak feature.

Results from RALEF-2D simulations are presented in Fig. 4.2 alongside the experimental data. With the results in Figure 4.2 the comparison between experimental and simulated ion energy spectra is extended from 60° in Hemminga *et al.* [94] to a multitude of measurement angles. The resemblance is similar: the general shapes of the experimental front-side spectra are reproduced by the simulations, including the peaked high-energy feature [94]. In addition, the simulated spectra follow a similar angular trend where the position of the high-energy peak shifts to lower energy while reducing in amplitude. The overall agreement between simulations and experiment in Fig. 4.2 validates use of the single-fluid approach [94] for the full 3D expansion.

The spectral shape with a high-energy peak was investigated in Hemminga *et al.* [94] for a single, 60° measurement angle. The peak was associated with a density shell forming during the expansion. In the following we argue, using our simulations, that the observed ion emission anistropy can be explained by the fact that this density shell is intrinsically anisotropic.

In Figure 4.3, we present the ion speed $|v|$ (upper panel) and mass density ρ (lower panel) profiles for three time steps in the simulation. These time stamps (4, 19, and 145 ns) refer to the time since the beginning of the simulation which is chosen 15 ns prior to the occurrence of the laser intensity maximum. As inset in each panel the temporal profile of the laser pulse is sketched; the hatched area represents the portion of laser energy added to the system up to that time. The angular positions of the seven RFAs used in the experiment are indicated by radial white dashed lines.

At $t = 4$ ns, only a small fraction of the Gaussian temporal pulse has illuminated the droplet, as shown in panel (a). The high-density burst close to the droplet surface, for $d < 0.05$ mm, is equivalent to the initial burst of ablation described in our previous work

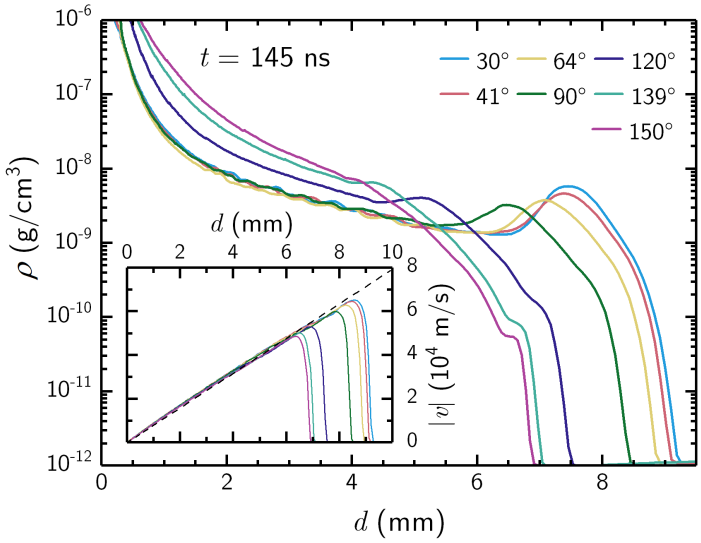

Figure 4.4: Radial lineouts of the ion density profiles calculated by RALEF-2D are shown for the angles at which RFAs were placed in the experiment, 145 ns after the start of the simulation. The inset shows the complementary velocity profiles, exhibiting their characteristic linear behaviour, which is exemplified by a ballistic curve shown as reference by the dashed line.

[94]. We note an angularly directed flow around the droplet. It is the first indication of the continuous flow of laser-ablated material around the droplet. This is the result of the pressure gradient from the laser-produced plasma to the vacuum behind the droplet, and the phenomenon continues for the subsequent expansion.

At $t = 19$ ns, as shown in Figure 4.3(b), the main feature is a high-density shell. As previously described by the authors [94], such a density shell is formed by the interaction of two ablation bursts. The first burst is that of the aforementioned initial ablation, and the second is formed by the hot and dense plasma generated by the laser pulse near peak intensity, producing high speeds. This second ablation burst interacts with material from the initial ablation, and forms a density shell at its front. While the initial ablation burst is expanding radially outwards in all directions, this second ablation is highly direction, mainly expanding towards the $\alpha = 0 - 90°$ half-plane. As a result, the density shell inherits this angular dependence, and becomes *quasi*-spherical. In comparison to the simulation presented in Ref. [94], the current inclusion of laser beam refraction leads to minor spatial fluctuations in the formed plasma ($d < 0.15$ mm), both in speed and density. However, at late time ($t = 145$ ns, panel (c) of Figure 4.3), these fluctuations in the region of the high-speed density shell have faded out and we find convergence to a similar expansion profile as in Ref. [94].

Next, profiles (lineouts) of speed and density are extracted from the two-dimensional simulation data along radial lines towards the seven RFA positions at $t = 145$ ns, as presented in Figure 4.4. The angular dependence of the quasi-spherical density shell is clearly visible: the peak in the density profiles decreases in height and shifts to shorter distances with angle. The linear dependence of the local flow speed on distance (inset Fig. 4.4) follows the relation $v/d = 1/(t - t_0) \approx 7.7 \times 10^6\ \mathrm{s}^{-1}$ (evaluated at $t = 145$ ns with $t_0 = 15$ ns set at the maximum laser intensity).

Combining density and speed profiles enables obtaining, and explaining the ion energy distributions. In particular, we can interpret the power-law type behavior (up to the peak feature) seen in the spectra in Fig. 4.2 in terms of the underlying density profile. Figure 4.2(h) presents power-law fits $d^2N/dEd\Omega \propto E^\eta$ to two selected observation angles. The sole free parameter in the fit is the overall amplitude (offset in log-log representation). For the $\alpha = 30°$ angle a power $\eta = -1/2$ is seen to accurately capture the power-law fall-off, whereas $\eta = -1$ recovers the behavior for $\alpha = 150°$. We note that the distributions at intermediate angles can be described by intermediate powers η.

The origin of these power laws can be understood from an analytical ansatz based on a linear speed profile and an inverse power law density profile in three dimensions: $v \propto r$, $\rho \propto r^{-n}$, with radial coordinate r, and volume $V \propto r^3$. Omitting the explicit solid angle dependence, the expression for the ion energy distribution dN/dE becomes

$$\frac{dN}{dE} \propto \frac{\rho dV}{v dv} = E^{(-n+1)/2}, \tag{4.1}$$

where the relation $r \propto v \propto E^{-1/2}$ is applied. The experimental power laws can be related to analytical density profiles in the following way: $\eta = -1/2$ ($\alpha = 30°$) corresponds to $n = 2$ and $\eta = -1$ ($\alpha = 150°$) to $n = 3$. This suggests that towards $\alpha = 150°$ the tin fluid rarefies according to its increase in volume $\propto r^3$ with time. For purely radial flow described by a linear speed profile (*cf.* inset Fig. 4.4), the density profile $\rho \propto 1/r^3$ is a time-independent solution of the continuity equation, conserving the product $\rho v r^2$. Towards $\alpha = 30°$ the behavior is consistent with that observed in Ref. [81] where $\rho \propto 1/r^2$ is associated with a steady spherical flow for constant v near the critical surface [81].

Finally, we may partially attribute the remaining differences between experiment and simulation to the completeness of the employed simulation model, which cannot fully capture imperfect experimental conditions. The experimental spectra consistently exhibit a more gradual fall off towards higher kinetic energies than is seen in the simulations, which may be caused by high-intensity regions in the laser beam profile or incompleteness of the RALEF-2D physical model. Further study is required to address these points.

4.4.2 Angular distributions of number, momentum, and energy

The overall number of ions, and the total momentum and energy balance of an LPP are important metrics, especially in the industrial context of the production of debris in the EUV light generation process. For the experiment, we use our angular coverage of the axisymmetric LPP to interpolate the captured data, in order to provide an estimate of the total ion emission in 4π sr. For this purpose we work with energy-integrated spectra. In the spectral integration the low-energy integration boundary E_{min} is set to 60 eV to match the lower bound of the simulation. Per unit solid angle, the total ion number, total radial ion momentum, and total ion energy are calculated using

$$\frac{dN_{\text{tot}}}{d\Omega} = \int_{E_{\text{min}}}^{\infty} \frac{d^2N}{dEd\Omega} dE', \tag{4.2}$$

$$\frac{dp_r}{d\Omega} = \int_{E_{\text{min}}}^{\infty} p_r(E') \frac{d^2N}{dEd\Omega} dE', \tag{4.3}$$

$$\frac{dE_{\text{tot}}}{d\Omega} = \int_{E_{\text{min}}}^{\infty} E' \frac{d^2N}{dEd\Omega} dE', \tag{4.4}$$

where $p_r(E) = \sqrt{2mE}$ is the momentum of a single tin particle with mass m, assumed to move only in the radial direction. Since tin has ten stable isotopes, we use the abundance-weighted average mass of 118.71 amu for m.

The angular distributions of N_{tot}, E_{tot}, and the magnitude of the momentum vector, p_r, are shown in Figure 4.5. The gray bands surrounding the RFA data delineate the confidence intervals of the distributions. These confidence intervals are derived from uncertainties in the transmission of the RFA grid configuration and in the choice of the baseline subtraction method. For the numerical counterpart, the values defined in equations (4.2–4.4) are calculated in the same manner, for every 1° α-wise bin. All three distributions underwent a 10° running average, but non-physical features remain visible in the angular distributions. Numerical velocity fluctuations in the vicinity of the droplet – both in magnitude and direction – impact the expansion further radially outwards. At such distances these velocity fluctuations lead to angular density fluctuations. For example, this is visible inside the quasi-spherical density shell visible in Figure 4.3(c). However, the remaining features have little impact on the overall size and shape and we conclude that the numerical distributions are in good agreement with the experimental distributions.

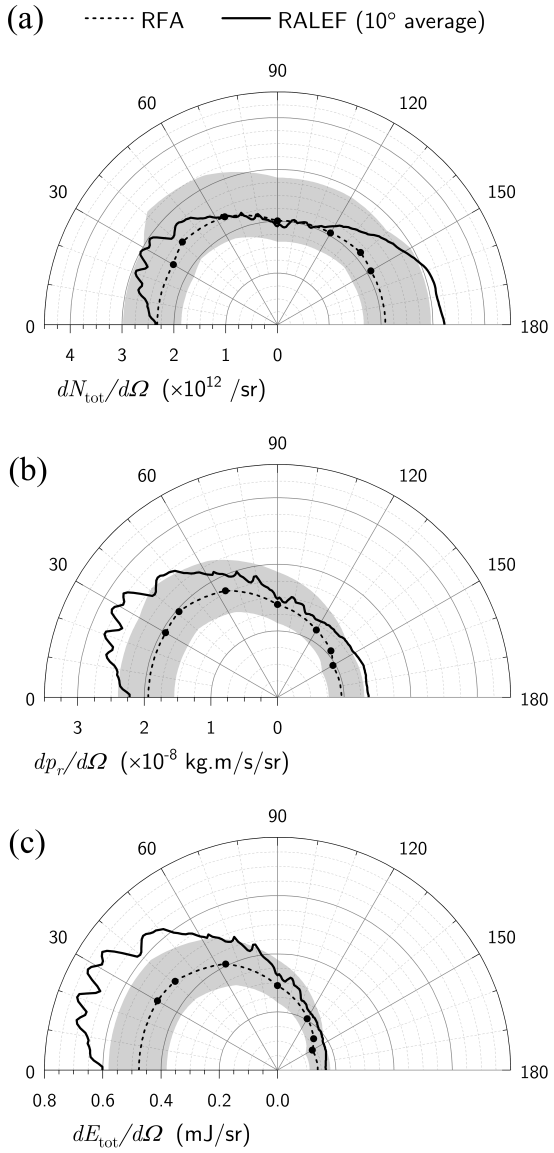

Figure 4.5: Angular distributions of ion (a) number, (b) momentum and (c) total energy, as calculated using the ion energy spectra from RFA measurements (black circles) and from RALEF-2D simulations (solid black line). In the three panels, the seven-point RFA data sets were interpolated and extrapolated as a guide to the eye (black dashed line). The gray bands around the RFA distributions represent the confidence intervals (see Subsection 4.2.1). The RALEF-2D distributions include a 10° running average.

Next, the 4π-integrated metrics are calculated using interpolated data, integrating over the entire sphere exploiting the cylindrical symmetry. The required extrapolation of the distributions below $\alpha = 30°$ and above 150° assumes constant values, equal to the closest measurement entry. For the RFA measurements presented in Figures 4.2 and 4.5, we estimate the total number of ions to be $N_{\mathrm{tot}} \approx 2.7 \times 10^{13}$. The fraction f_N of the measured number of ions to the total number of ion atoms present in the initial droplet is 7.4%. The total energy carried by ions with $E > 60\,\mathrm{eV}$ in the experiment is $E_{\mathrm{tot}} = 3.8\,\mathrm{mJ}$. From the RALEF-2D simulations we find a total ion number of 3.0×10^{13}, that is a fraction $f_N = 8.1\%$ of the total tin atoms, closely matching the experimental value. The total kinetic energy of 4.9 mJ is slightly higher than the experimental value, but well within the uncertainty limits. The momentum imbalance is discussed separately in the following section.

4.4.3 Droplet plasma propulsion

The net momentum imbalance p_z in the ion emission, oriented along the z-axis given the cylindrical symmetry, equals the momentum imparted on the remaining liquid mass noting that the momentum carried by the incident laser photons is only a small fraction of this momentum imbalance [27]. Thus, our ion emission measurements enable the prediction of the plasma propulsion velocity of the liquid drop that was previously studied by Kurilovich *et al.* [27].

For the experiment presented in Figures 4.2 and 4.5, the net projected momentum is $p_z = 2.4 \times 10^{-8}\,\mathrm{kg\,m/s}$. With the estimate of the remaining molten tin mass, using our RFA data to assess the mass loss (thereby implicitly excluding mass loss in the form of neutral atoms), we obtain a propulsion velocity of the target $v_{\mathrm{t,RFA}}$ of 360(70) m/s as inferred from the ion momentum imbalance. Integrating the experimental values to 30 eV instead yields a similar velocity of 348(70) m/s. In the same manner for the numerical modelling, we find a momentum imbalance of $3.3 \times 10^{-8}\,\mathrm{kg\,m/s}$ leading to a propulsion speed of 449 m/s.

The target velocity is also assessed directly by recording a high-resolution single-shot shadowgraphy image of the target a few µs after the laser-droplet impact. The shadowgraphy imaging scheme and methods are outlined in detail in the Refs. [27, 83, 91, 113]. The target propulsion velocity v_{t} is assessed stroboscopically by scanning the delay Δt and obtaining the position of the center of mass, Δx, such that assuming ballistic motion, we find $v_{\mathrm{t}} = \Delta x / \Delta t$ [27, 83]. This technique yields an average propulsion velocity of 337 m/s, in excellent agreement with the ion momentum balance approach.

In the RALEF-2D simulation, the shadowgraphy measurement of velocity is best compared to the center-of-mass (COM) velocity of the tin fluid 300 ns after the start of the simulation. Only mesh cells with a density in excess of the threshold value $\rho_{\mathrm{thr}} = 1\,\mathrm{g/cm^3}$ are taken into account for the COM velocity calculation. This method yields a velocity of

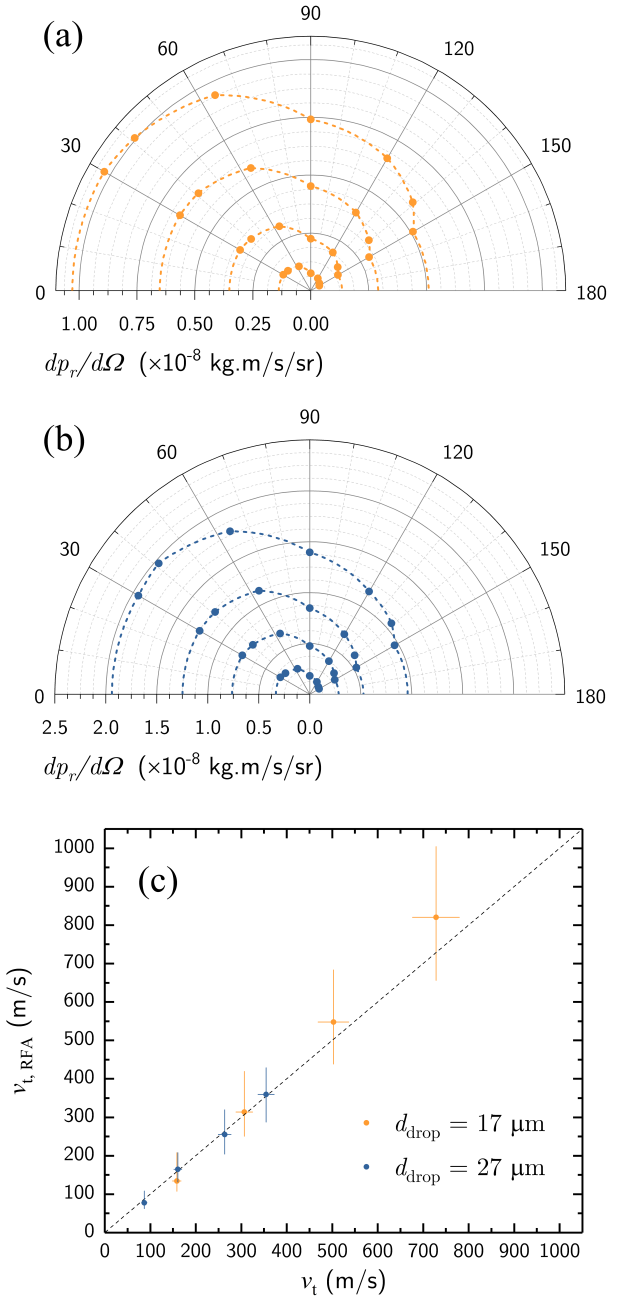

Figure 4.6: Angular dependence of the momentum carried by ions for a small [(a) $d_{\text{drop}} = 17$ µm, orange markers] and a large [(b) $d_{\text{drop}} = 27$ µm, blue markers] droplet. The four data sets correspond, with increasing momentum, to laser pulse energies equal to 8, 26, 60, and 100 mJ. Droplet velocities measured through shadowgraphy (v_t), and calculated using the momentum imbalance ($v_{t,\text{RFA}}$), are compared in panel (c). The dashed diagonal line denotes $v_{t,\text{RFA}} = v_t$.

435 m/s, close to the 449 m/s value from the momentum imbalance approach above. The simulations thus predict a propulsion velocity somewhat larger than found in the experiment (consistent with Refs. [27, 83, 111]). We note that the accuracy of the prediction of the droplet propulsion by simulations using RALEF-2D was validated separately over a large parameter space in previous works [27, 91, 111, 113].

Now that we have established the accuracy of the ion measurements for a single experimental parameter set through the accurate prediction of the propulsion speed of the laser-impacted droplet using momentum conservation we next vary the laser pulse energy and droplet size in the experiments. Specifically, laser pulse energies of 8, 26, 60, and 100 mJ are used to irradiate droplets with sizes $d_{\mathrm{drop}} = 17$ and 27 µm. Figures 4.6(a,b) present the momentum anisotropy for the various laser energies separately for each droplet size case. Figure 4.6(c) compares the results of the propulsion speed inferred from the momentum balance $v_{\mathrm{t,RFA}}$ with the propulsion speed obtained from shadowgraphy v_{t}. We find that the excellent agreement holds over the full probed experimental parameter space, which includes settings directly relevant for the industrial use case. Momentum imbalance measurements may thus be applied to serve as diagnostics for droplet propulsion and, the strongly correlated [111], deformation in state-of-the-art nanolithography tools.

4.5 Conclusion

We presented results from experimental and numerical studies of the anisotropy in the expansion of a tin-microdroplet-based laser-produced plasma into vacuum. Plasma was generated by nanosecond Nd:YAG laser pulse impact (laser wavelength $\lambda = 1.064$ µm) onto tin microdroplets. Measurements of the ion kinetic energy distributions were performed using retarding field analyzers set up under several angles. These measurements revealed strongly anisotropic emission characteristics, in close agreement with two-dimensional radiation-hydrodynamic simulations that we performed using the RALEF-2D code. The ion emission spectrum features a high-energy peaked that was previously explained in terms of a complex interaction between two ablation fronts. In the present work, this interaction was shown to lead to highly anisotropic features. A monotonic decrease visible in the emission spectra right up to the high-energy peak was explained in terms of a power-law drop in density with the radial coordinate, consistent with existing models of rarefaction. The angle-resolved ion spectral measurements were further shown to provide a very precise prediction of the propulsion of the droplet by the plasma generated from laser-pulse impact.

Acknowledgements

The authors thank Duncan Verheijde for his support in understanding and improving the RFA electronics. They also thank Jorijn Kuster for designing efficient and user-friendly software interfaces for our experimental setups and they thank Bo Liu for useful discussions. This work has been carried out at the Advanced Research Center for Nanolithography (ARCNL). ARCNL is public-private partnership with founding partners UvA, VU, NWO-I and ASML, and associate partner RUG. This project has received funding from European Research Council (ERC) Starting Grant number 802648. This publication is part of the project New Light for Nanolithography (with project number 15697) of the research programme VIDI which is (partly) financed by the Dutch Research Council. This work made use of the Dutch national e-infrastructure with the support of the SURF Cooperative using grant no. EINF-2947.

Appendix

The position of and the solid angle covered by the seven RFAs are summarized in Table 4.1 in terms of their elevation (β) and azimuth (γ) with respect to the laser axis (see Fig. 4.1(a)). The cylindrical symmetry of the laser-droplet system defines the angular position of any RFAs by a single angle α (see main text).

Table 4.1: RFA position and coverage. Elevation angle (β) and azimuth (γ) with respect to the laser axis yield the angular position by a single angle α (see main text). RFAs are placed at a distance d from the plasma, and cover a solid angle $\Delta\Omega(d)$.

α (°)	β (°)	γ (°)	d (mm)	$\Delta\Omega$ (µsr)
30	0	30	420	111
41	-30	330	420	111
64	30	60	420	111
90	30	270	420	111
120	0	120	296	224
139	-30	210	296	224
150	30	180	296	224

chapter 5

Laser-intensity dependence of ion emission from Nd:YAG-laser-produced plasma expanding into vacuum

Lucas Poirier, Adam Lassise, Ronnie Hoekstra, John Sheil, and Oscar O. Versolato

Adapted from *Dependence of ion charge-energy emission from Nd:YAG-laser-produced tin plasma as function of laser intensity in the* $0.4 - 40 \times 10^{10}$ *W/cm*^{2} *range*,
Physics of Plasmas **30**, 083505 (2023).

We investigate experimentally the dependence of ion emission from laser-produced plasma on laser intensity. The plasma is generated in vacuum from tin micro-droplets (diameter ranging from 17 to 35 µm) using pulsed Nd:YAG laser light (laser wavelength $\lambda = 1.064\,\mu$m) over a range of intensities ($0.4 - 40 \times 10^{10}$ W/cm^2). We measure charge-state-resolved and integrated ion energy distributions at seven angular positions around the plasma using seven retarding field analyzers. We highlight peak features in both types of spectra and describe the dependence of their energies on laser intensity with power law functions. The obtained scaling laws match analytical scaling laws derived from relevant literature. Surprisingly, the analytical scaling laws exhibit strong isotropy, while the ion energy spectra are highly anisotropic. We also report on an apparent universal scaling of the energy-dependent average charge state.

5.1 Introduction

Extreme ultraviolet (EUV) light is utilized in the lithographic process to produce nanometer-sized features on silicon chips. Industrially, tin laser-produced plasmas (LPP) are now used to produce the EUV light. The density, temperature, and morphology of the LPP are optimized for EUV production. However, ion emission from the LPP is also to be considered, as this adverse process is known to take a toll on EUV output from the source, *e.g.*, by gradually tarnishing the performance of the surrounding EUV transport optics via implantation and sputtering by ions and neutrals on their surface. Furthermore, all the laser energy transferred to ion kinetics is not available for EUV production and can therefore be considered to be wasted.

The parameter space of the LPP experiment is vast (drive laser wavelength, laser pulse morphology and intensity, target volume and morphology, use of multi-laser-pulse schemes, *etc*) and currently systematic exploration is incomplete. Analytical works have produced valuable general insights into plasma expansion [3, 98, 99]. However, analytical work necessarily relies on highly idealized and simplified conditions and needs to be supported by dedicated numerical simulations and experiments. Existing experimental literature examines the energy, charge state, and angular distributions of emitted ions for experimental parameters similar to those of nanolithographic EUV sources, using a variety of ion diagnostic tools. Such tools include electrostatic probes [100, 101], Faraday cups [12, 65], electrostatic analyzers [21, 61, 65, 102], retarding field analyzers[19], and Thompson parabolas [12]. Many studies observed anisotropy in the charge-integrated [12, 65, 100, 103–107] and charge-state-resolved ion emission into a buffer gas [21]. Morris *et al.* [61, 102], O'Connor *et al.* [108] and Brändstatter *et al.* [100] studied angle- and charge-state-resolved ion emission in a solid tin target experiment. They reported increasing ion charge states and increasing average kinetic energies for decreasing angles with respect to the direction of the incoming laser pulse. O'Connor *et al.* [108] additionally measured increasing numbers of ions, average ion energies, and average charge states with increasing laser intensities.

We recently combined absolute angle- and charge-state-resolved kinetic energy measurements on an industrially relevant tin-microdroplet-based plasma, expanding into the vacuum [114]. More specifically, the anisotropy of the ion emission was investigated. The presence of a high-energy peak in the ion energy spectra was found to be more prominent for smaller angles with respect to the direction of the drive laser [114]. Our studies furthermore showed that the experimental ion energy spectra could be reproduced using a numerical single-fluid, single-temperature radiation hydrodynamic approach employing the code RALEF-2D [94, 114]. Given the complexity of ion flow characterization, we previously performed a proof-of-principle experiment for a single laser intensity and focused on the overall hydrodynamic flow, not on the individual charge states. To complement our previous

work [94, 114], as well as that of Morris *et al.* [61, 102] and O'Connor *et al.* [108], we here investigate experimentally the dependence of ion emission, including the individual charge states, on laser intensity — an important parameter for the optimization of EUV light production and for the optimization of tin usage for EUV production and suppression of ion "debris".

Retarding field analyzers (RFAs) are employed to provide information on ion flow, energy, and charge state. Seven RFA detectors placed around the LPP are used to map the angular dependence of the ion emission. First, we recall the experimental setup used for ion detection at ARCNL and describe the explored parameter space. We present charge-state-resolved and charge-integrated ion energy spectra, where we highlight notable spectral features. We investigate said features and describe their variation with increasing laser intensity. In addition, we discuss the universal trend of the energy-dependent ion charge state spectrum obtained for three different droplet sizes recorded under seven different angles with respect to the direction of the laser.

5.2 Experimental methods

5.2.1 Experimental setup

The experimental setup is thoroughly described in previous publications [68, 109, 114]. Here, we briefly summarize the key experimental parameters. The laser used to drive the tin plasma is a 10 Hz pulsed Nd:YAG laser operating at 1064 nm wavelength. The laser pulses have a Gaussian profile in both temporal and spatial coordinates. The spatial full-width-at-half-maximum (FWHM_{xy}) is 100 µm (the spatial profile has cylindrical symmetry), and the temporal full-width-at-half-maximum (FWHM_{t}) is either 8 or 10 ns. The pulse duration is here determined by the Q-switch delay of the laser, with the shorter 8 ns pulse length corresponding to higher available pulse energies. Tin plasmas are generated in a vacuum chamber (maintained at approximately 10^{-7} mbar) from liquid tin droplets having three diameters, namely 17, 27, and 35 µm. For each droplet size, we set the total laser pulse energy to four values ranging from approximately 5 to 100 mJ for the 10 ns pulse length measurements (on 17 and 27 µm-diameter droplets), and from approximately 5 to 350 mJ for the 8 ns case (17 and 35 µm-diameter droplets). Note that the amount of laser light absorbed by the droplet and plasma not only depends on the initial size of the droplet but also on the radial expansion of the tin mass (either in the form of tin liquid or plasma) as the laser pulse is absorbed. Unless stated otherwise, the 27-µm diameter droplets and 10-ns FWHM_{t} pulses are used. For this droplet size the set laser pulse energies in vacuum are 8, 25, 58, and 97 mJ, corresponding to laser intensities of approximately 6, 21, 48, and 80 GW/cm^2.

5.2.2 Ion diagnostics

An array of seven retarding field analyzers gives angle-resolved information on the energy and charge of the ion emission from the LPP. The devices' corresponding post-processing analysis was described in detail in previous studies [109, 114]. The post-processing "bottom-up" analysis [109] constructs charge-integrated ion spectra (dN/dE or dQ/dE) through a summation of the spectra from individual charge states

$$\frac{dN}{dE} = \sum_z \frac{dN_z}{dE}, \tag{5.1}$$

$$\frac{dQ}{dE} = \sum_z \frac{dQ_z}{dE} = \sum_z ze\frac{dN_z}{dE}. \tag{5.2}$$

The seven RFAs are placed at $\alpha = 30$, 41, 64, 90, 120, 139 and 150° with respect to the direction of the incoming laser beam [in the current case of cylindrical symmetry a single angle α suffices to describe the angular position of each RFA — see Ref. [114] and figure 5.2(a)]. The distances from the LPP to the RFAs range from 296 to 420 mm. The distance to the LPP and the aperture size (5 mm in diameter) of the RFAs together define their solid angle of collection, for which the ion signal is corrected. The transmission of the devices is defined by that of the four-grid stack. As discussed in Ref. [114], the full transmission lies between 41 and 83%, corresponding to the extreme cases of minimum and maximum mutual overlap of the grids. In the following, we take a transmission value of 62% *cf.* Ref. [114]. Two of the grids carry the retarding electric potential used for charge state unraveling. The purpose of each of the grids is discussed in detail in Ref. [109].

The raw RFA signal is amplified using a custom-built high-speed, large bandwidth and trans-impedance amplifier with a gain of 25 kV/A [109].

5.3 Results and discussion

We examine the dependence of the ion energy spectra on laser intensity from tin LPPs produced from mass-limited droplet targets. Four laser intensities are set for each selected droplet diameter, ranging 0.4×10^{10} to 40×10^{10} W/cm^2.

5.3.1 Intensity dependence of charge-resolved ion energies

Using our post-processing scheme [109], energy distributions are retrieved for each charge state observed in the LPP.

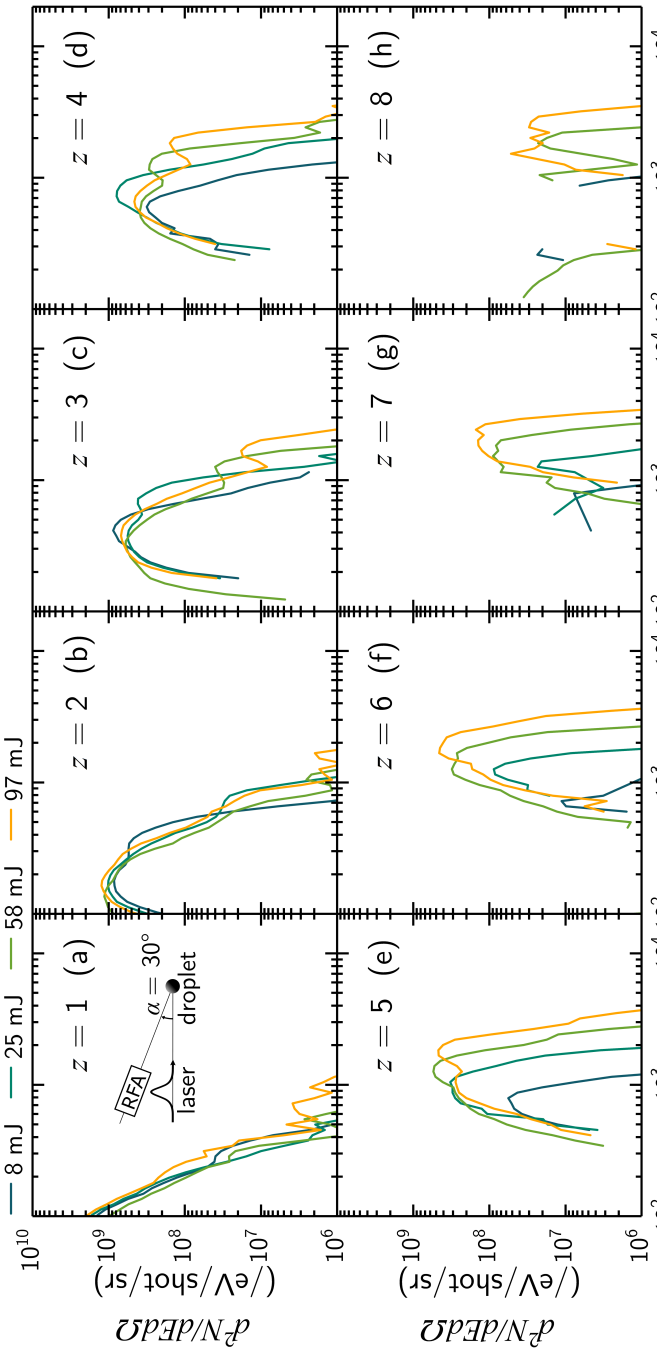

Figure 5.1: (a – h) Charge-specific ion energy spectra for a 27 µm-diameter droplet and four laser pulse energies (E_L = 8, 25, 58 and 97 mJ), measured at 30° with respect to the direction of the laser [see inset in panel (a)].

Charge-resolved ion energy spectra

Figure 5.1 shows the variation of charge-state-resolved spectra with laser intensity at a 30° observation angle for the 27 µm-diameter droplet target. In the following, we restrict the low energy bound to 100 eV for the sake of visual clarity. We calculate the laser intensity using $I = (2\sqrt{2\ln 2/2\pi})^3 E_\mathrm{L}/(\mathrm{FWHM}_{xy}^2 \mathrm{FWHM}_t)$ where E_L is total laser pulse energy, following Schupp *et al.* [115].

First, we note that the (average) kinetic energy of the ions increases with increasing charge state. Similar observations were made in our studies [68, 109] as well as in O'Connor *et al.* [108] and Morris *et al.* [61]. The former study reports a linear increase of the average ion kinetic energy with charge state [108]. The increase in kinetic energy with charge state saturates around a few keV for higher charge states (say, $z > 5$ or 6 for the measurement presented in figure 5.1).

For $z = 1$, we find that increasing laser pulse energy barely affects the energy distributions. At best, it causes a small increase in the spectral intensity of the charge-resolved spectra. All $z = 1$ spectra exhibit a monotonically decreasing yield with increasing kinetic energy, and the distributions most probably peak below 100 eV. For the lowest multiply charged ions ($z = 2 - 4$), we report a clearly peaked distribution, with an asymmetrical widening of the spectra in the direction of larger energies with increasing laser pulse energy. With increasing laser energy an additional high-energy peak emerges in the spectra. With increasing laser pulse energy, the energy corresponding to this second peak increases steadily, and its spectral intensity decreases (see figure 5.1(c)). For higher charge states ($z > 4$), the relative spectral intensity of the second peak with respect to the first peak grows with increasing laser intensity, eventually becoming dominant with respect to the first peak. This can be seen in the spectra shown in figure 5.1(d – e), for $E_\mathrm{L} = 97$ mJ, where the relative spectral intensities of the first and the second peak switches between $z = 4$ and $z = 5$. For a given laser pulse energy, the second peaks have the same energy for all charge states. Moreover, as charge state increases, the energy of the first peak converges to that of the second peak; they eventually merge into a single peak, for instance for $z = 7$, in the case of the 97 mJ pulse in figure 5.1(g).

Energy spectra for $z = 1 - 8$ are displayed in figure 5.2 for all seven observation angles for a 27 µm-diameter droplet illuminated by a 97 mJ laser pulse. A few immediate observations can be made. We note that at the back side ($\alpha > 90°$), one collects about twice the amount of low charge states ($z = 1 - 3$) as at the front side ($\alpha < 90°$) for any pulse energy, while the front side generates a greater amount of high charge states ($z > 3$). Moreover, for high charge states ($z > 3$), spectra captured at small angles ($\alpha \leq 90°$) peak at higher energies than those captured at large angles ($\alpha > 90°$).

Next, we note that the shape of the spectra transforms with decreasing angle and increasing charge state: gradually a shoulder appears on the high-energy side of the distributions. This

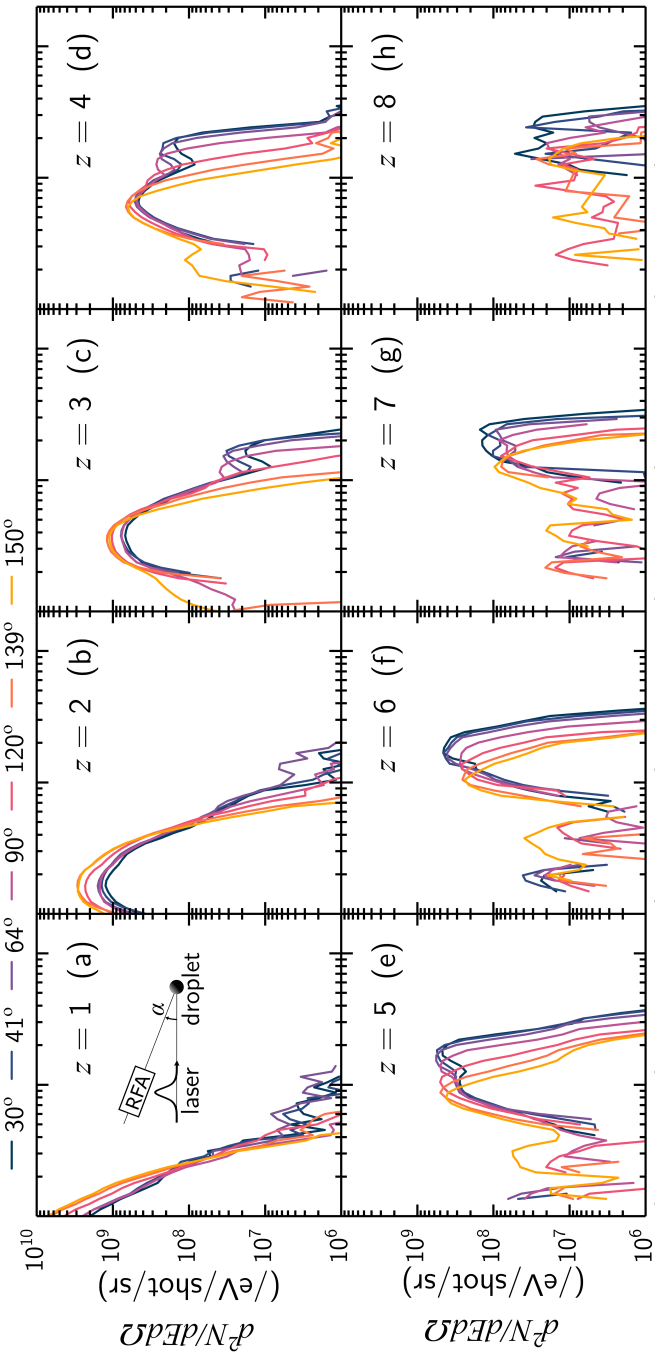

Figure 5.2: (a – h) Charge-specific ion energy spectra measured at seven different angles with respect to the direction of the laser light propagation (30, 41, 64, 90, 120, 139, and 150°) for a 27 µm-diameter droplet, 97 mJ laser pulse. The inset in panel (a) defines the angle α.

effect can be seen clearly in figure 5.2(d), where the spectra peak around 600 – 700 eV, while a second peak feature emerges around 1.5 – 2 keV. The signal intensity of this second peak decreases by three orders of magnitude with increasing detection angle from 30° to 150°.

The second, high energy peaks observed in figures 5.1 and 5.2 correspond to the high-energy features found in charge-integrated distributions dN/dE observed in our previous study [114]. The presence of this peak was explained by a bunching phenomenon: in short, the absorption of the peak intensity of the laser pulse by the plasma generates a fast and dense expansion shell, propagating anisotropically towards small observation angles ($\alpha < 120°$). This shell pushes all the slower material in its front as it expands in vacuum, giving rise to high-energy peaks in charge-integrated spectra. Here, we find that the bunching is made up of different – relatively high – charge state ions. The absence of a second high-energy peak in dN_z/dE at large angles ($\alpha > 120°$) was also observed in charge-integrated spectra [114].

Dependence of peak energies on intensity and charge state

Next, we track the energy of the maxima of the charge-state-resolved ion spectra dN_z/dE as a function of laser intensity for the 27 µm diameter and 10-ns pulse measurement. Where applicable, we track separately the first and second high-energy peaks. For $z > 4$, the two peaks merge into a single one, as seen in figure 5.2. Peak positions are recovered by (i) direct peak finding in dN_z/dE, (ii) finding roots in d^2N_z/dE^2, and (iii) looking for minima in d^3N_z/dE^3 traces. We use a common threshold- and distance-based algorithm from the `scipy` Python library for finding peaks. The first two methods (i-ii) result in similar positions for the first and second peaks, while the second-derivative-based method (iii) is apt for recovering the position of shoulder features. Peaks with signal intensity lower than approximately 3.5 times the local noise level are discarded in order to filter out incorrectly assigned peaks. We report the average value obtained from the three methods for the charge states $z = 2 – 6$ (the maximum for $z = 1$ lies out-of-range below 100 eV and the signal intensity of $z = 7, 8$ was insufficient for reliable application of our peak-finding methods).

Figure 5.3(a – g) shows the positions of the first (full markers) and second peaks (empty markers) as a function of charge state (from $z = 2$ to 6) for seven observation angles and four laser pulse intensities, for the 27 µm diameter droplet. At all angles and laser intensities, the position of the first peak clearly increases with charge state, while that of the second peak shows a much weaker dependence on charge state.

We heuristically model the position of the first peak as a function of charge state as a power law $A_\alpha(z+1)^{B_\alpha}$ (see an example in figure 5.3(a), yellow dashed line). The $z+1$ term in the model is motivated by the scaling of the plasma pressure (which drives the expansion) in the ideal gas picture as $P = (z+1)nT$, with ion density n and temperature T (in eV). Data points corresponding to merged first and second peaks are also used for fitting and are labelled

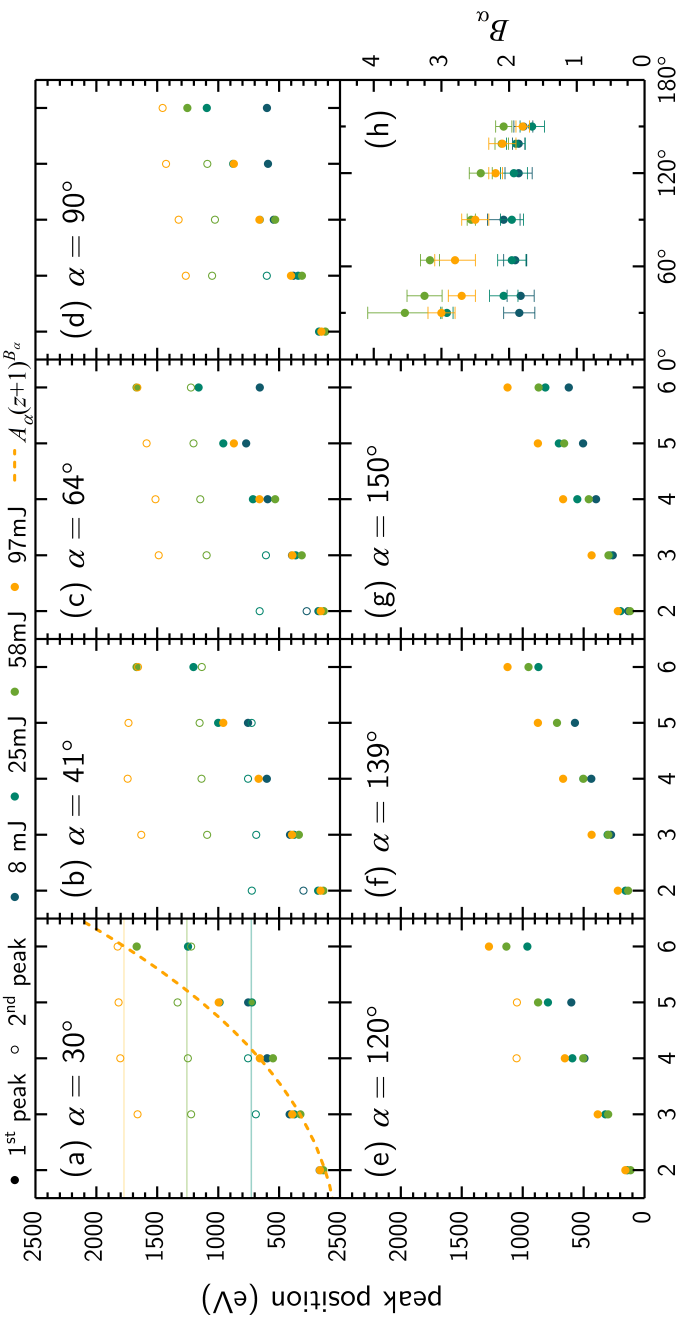

Figure 5.3: (a – g) First (full markers) and second peak (empty markers) positions in charge-state resolved spectra as a function of charge state for seven observation angles α. The horizontal lines in panel (a) are averages of the second peak position. Positions of the first peak are fitted with a power law $A_\alpha(z+1)^{B_\alpha}$ (yellow dotted line in (a)), and the power law exponents B_α are reported in panel (h); symmetrical error bars above and below the value of the exponents are defined as the statistical deviation obtained from the fit.

as pertaining to the second peak category in figure 5.3; this is the case for example for the 97 mJ, $z = 6$ peak found around 1800 eV in figure 5.3(a). The recovered power law exponents are displayed in figure 5.3(h) for each laser intensity. For the lower laser intensities, we find a nearly constant value of the power law exponent of about 2. At higher laser intensity, we find a stronger dependence of the exponent on angle α to converge to the same value at larger angles. The error bars displayed in figure 5.3(h) correspond to the statistical uncertainty of the power law fit. Murakami *et al.* [2] and Mora [3] report that the energy derived from the local characteristic sonic speed of the plasma E scales linearly with local temperature T and charge state z,

$$E \propto Tz. \tag{5.3}$$

The scaling observed experimentally is not linear with charge state, hinting that the detected ions are generated in regions of the tin plasma of different local temperatures T.

Besides the strong scaling of the first peak with charge state, we observe a near-constant value of the energy of the second peak for charge states $z = 2 - 6$. This value however increases strongly with increasing laser intensity. The horizontal lines in figure 5.3(a) show the increasing average position of the second peak (where applicable) with increasing laser intensities.

Next, we study the laser-intensity dependence of the positions of the two peaks. In figure 5.4(a – e), the same spectral maxima are shown for each charge state, now as a function of laser intensity for each of the seven angles at which ion kinetic energies were measured. Overall, the effect of increasing the laser intensity is an increase of the first or merged peak energy. Moreover, as seen in figure 5.2, it is apparent that the first peak energy (full markers) decreases with observation angle α for all intensities and charge states. For a given pulse intensity, the peak kinetic energy increases with charge state, up to 4 or 5, at which point the first peak merges with the higher-energy second peak (empty markers). In all instances of overlapping first and second peaks, there is a systematic bias in the recovery of the peak position due to the overlap of the two peaks of different amplitude and widths, referred to as line pulling. This may generate an overestimation of the first peak position and an underestimation of that of the second peak.

We fit power law models ($A_z I^{B_z}$, dotted black and green lines, respectively) to the positions of the charge-resolved first and second peaks (separately) from figure 5.4(a – e), and report in the inset of figure 5.4(f) the exponents for the first peak ($B_{1,z}$) and second peak ($B_{2,z}$) for each charge state (colored markers). The angle-average values of $B_{1,z}$ and $B_{2,z}$ are calculated for each charge state and shown in figure 5.4(f) (black and green lines and markers, respectively).

The first peak scaling exponent $B_{1,z}$ increases steadily from approximately 0 up to a value of 0.25 from $z = 2$ to 6, at which point the first peak has merged with the high-energy second

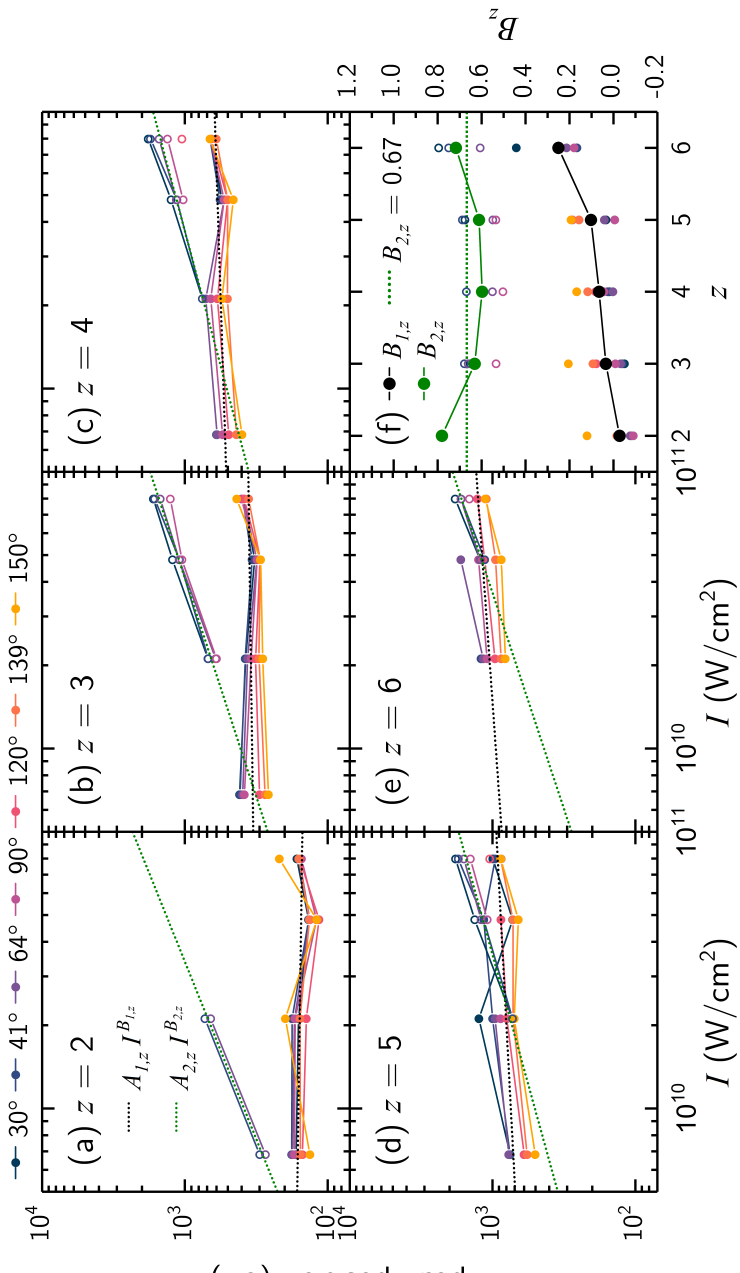

Figure 5.4: (a – e) Positions of the first (full markers) and second (empty markers) ion energy peaks, where applicable, for charge states $z = 2 - 6$, and for seven angles α between 30 and 150°; for each charge state, seven data sets corresponding to the seven observation angles are fitted separately with a power law; the averages of the seven fitted power laws are presented (black and green dotted lines for the first and second peaks, respectively); panel (f) shows the angle-averaged power law exponents B_z as a function of charge state z (black markers for the first peak $B_{1,z}$, green markers for the second peak $B_{2,z}$); fit results for the individual angles are also shown.

peak. The scaling exponent of the second peak positions $B_{2,z}$ varies between 0.5 and 0.8, with an average value of 0.67 (green dotted line).

The scaling exponents $B_{2,z}$ for $z < 6$ take similar values; this is explained by the common bunching behavior of the underlying ions. We also expect those scaling exponents to be similar to that of the peaks found in charge-integrated spectra, which were observed in an earlier study [114]. This point is specifically addressed later in section 5.3.3.

We note that whereas the ion kinetic energy spectra show a very strong dependence on the emission angle, the power law scalings extracted from the spectra show a relatively weak angular dependence. Overall, the same trends were observed in experiments with droplet targets of different diameters. These results hint at a deeper underlying physical law. Further study is required to more comprehensively explain the results for the individual charge states and may involve particle-in-cell (PIC) numerical modeling.

5.3.2 Empirical scaling of $\overline{z}(E)$

In most, if not all captured data, the average ion energy increases with charge state up to a certain energy around which all higher charge states accumulate (*e.g.*, around 1.5 – 2 keV for $z \geq 5$ for the data presented in figure 5.4). This increase is in line with expectations for the behavior *cf.* Eq. 5.3. For the description of a plasma containing several charge states simultaneously, it is convenient to instead consider the behavior of the average charge state $\overline{z}$ [80].

We recover the energy-dependent average ion charge state $\overline{z}(E)$ from charge-resolved ion spectra. The full energy range (for instance from 10 eV to 1 keV) is divided into 100 logarithmically-spaced energy bins, and the average charge state is calculated in each of the bins using

$$\overline{z}(E_i) = \frac{\sum_z z \frac{dN_z(E_i)}{dE}}{\sum_z \frac{dN_z(E_i)}{dE}}, \tag{5.4}$$

where i refers to the energy bin index, E_i is the center kinetic energy of the i-th bin, and $dN_z(E_i)/dE$ is the average value of dN_z/dE in the i-th energy bin. Note that charge-resolved ion spectra dN_z/dE consist of a discrete number of data points; this number is equal – at best – to the number of scanned retarding voltages (see Poirier *et al.* for more detail [109]). The spectra are interpolated numerically in order to calculate $\overline{z}(E)$.

We restrict the high-energy range of $\overline{z}(E)$ to the approximate position of the fast fall-off in dN/dE, beyond which charge state assignment by our post-processing method becomes unreliable due to low signal-to-noise. In the same manner, the low-energy bound of the $\overline{z}(E)$

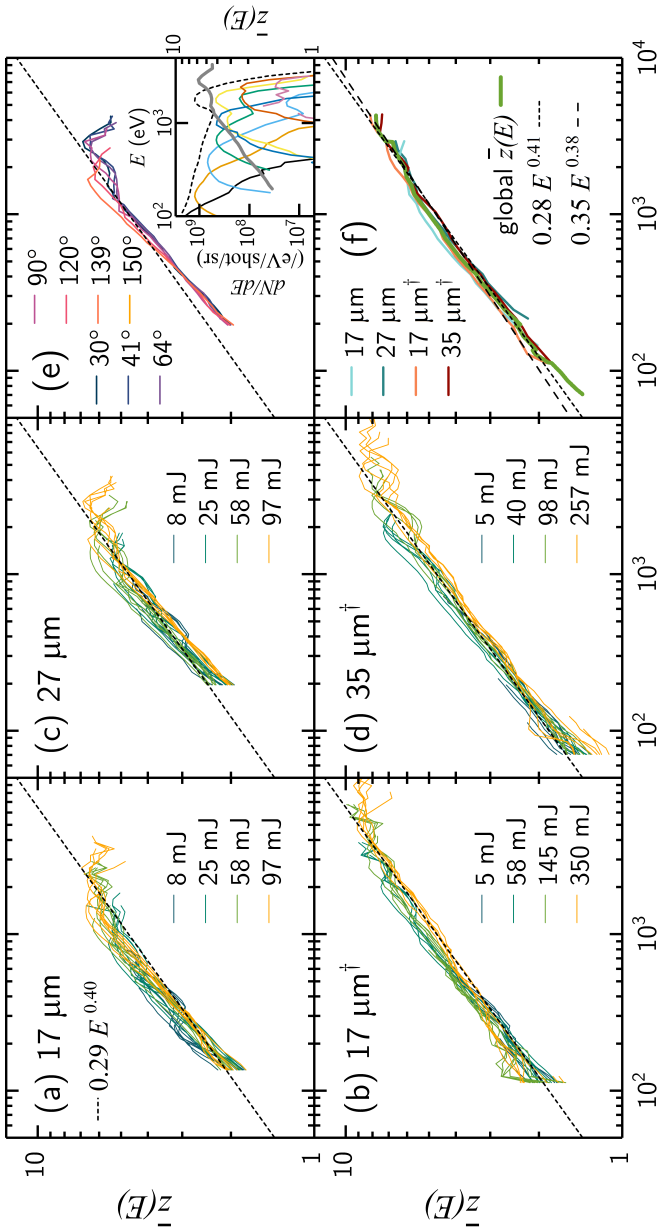

Figure 5.5: (a – d) Average charge state as a function of the kinetic energy for three different droplet diameters and two different laser pulse durations for the 17 µm diameter droplet, and for seven observation angles. The dagger marker † indicates 8 ns long laser pulses, while its absence indicates 10 ns pulses. Panel (e) shows the angular dependence of $\bar{z}(E)$ for the 27 µm diameter droplet and 97 mJ laser pulse. The inset in panel (e) shows $\bar{z}(E)$ (gray line) for the 30°, 97 mJ case, and the corresponding dN/dE (dashed black line) and dN_z/dE (colored lines) distributions. Panel (f) shows the average $\bar{z}(E)$ trend for each droplet diameter and pulse duration; a global average (green line) is displayed. Two power law fits are also shown, either using a fixed exponent taken from the literature (black short-dashed line) or using a free exponent fit (black long-dashed line). The latter is also shown in panels (a – d), as a guide to the eye.

spectra is set to the energy at which all dN_z/dE terms are sufficiently well defined, for all spectra (at all angles α, and for all pulse energies E_{pulse}).

In figure 5.5(a – d) we present the $\overline{z}(E)$ spectra for three droplet diameters, and two different pulse durations for the 17 µm droplet (the two measurements with $\text{FWHM}_t = 8$ ns are labeled with a dagger †). Panels (a – d) show $\overline{z}(E)$ assessed at the seven available angles α, and for four different laser pulse energies.

Figure 5.5(e) shows $\overline{z}(E)$ spectra for seven different angles (dark blue to yellow color gradient), and for a laser pulse energy of 97 mJ. The spectra look similar aside from the high-energy ($E > 10^3$ eV) region. A hump is observed at high-energy, and its position shifts to lower energies with increasing α.

Figure 5.5(f) shows the averaged $\overline{z}(E)$ for three different droplet diameters, and two laser pulse durations for the 17 µm droplet. Four pulse energies and seven observation angles were averaged in each case. A global average of all $\overline{z}(E)$ spectra is shown (green line). A common power-law-type trend with little deviation is seen to hold for all laser intensities, droplet diameters, and observation angles. The trend is especially well-defined in the 10^2 – 10^3 eV range. The optimized free-parameter power-law scaling of the global average $\overline{z}$ is $0.28E^{0.41}$; it is displayed in each panel to guide the eye (black short-dashed line). We can relate this scaling with laser intensity with a few analytical ansatzes. In addition to equation 5.3, Basko *et al.* [80] reported the empirical scaling law

$$\overline{z} \propto T^{0.60}. \tag{5.5}$$

Following Basko *et al.* [80], we derive

$$\left.\begin{aligned} E \propto T^{1+0.60} \implies T \propto E^{1/1.60} \\ \overline{z} \propto T^{0.60} \end{aligned}\right\} \overline{z} \propto E^{0.60/1.60} \implies \overline{z} \propto E^{0.38}. \tag{5.6}$$

This empirical model is shown in figure 5.5(f) (black long-dashed line). The power law prefactor was obtained by fitting the global average data spectrum (green line in figure 5.5(f)). The latter stands below the fitted model at low energy and above it at high energies, and both are close to the free-parameter power law fit (black short-dashed line). We thus find that theory is remarkably well able to explain the observed power law scaling. However, we also know that the above theory description is incomplete, and might not be expected to explain the full expansion process in particular at low densities where charge freezeout may occur [116].

Some systematic deviations from the main trend are observed: for instance, at small angles, many high charge states ions have the same average energy, which pulls the $\overline{z}(E)$ below the high-angle case, where an overlap of different charge state spectra is not seen.

This is illustrated in panel (e), where a plateau in $\overline{z}(E)$ is observed at the position where high-charge-state ions bunch up. The inset of panel (e) illustrates the construction of $\overline{z}(E)$ (gray line) from the 30°, 97 mJ ion energy distributions (colored lines for dN_z/dE and dashed black line for dN/dE). The position of the plateau in $\overline{z}(E)$ matches with that of the high-energy bunching in dN/dE and dN_z/dE. Aside from the high-energy behavior, the $\overline{z}(E)$ spectra taken at different angles are remarkably similar, even though the charge-resolved and charge-integrated spectra differ substantially.

The significance of a common $\overline{z}(E)$ scaling for future application lies in the fact that the average charge state spectrum can be used to convert a current-type distribution (dQ/dE) to a flow-type distribution (dN/dE):

$$\frac{dN(E)}{dE} \approx \frac{dQ(E)}{dE}\frac{1}{e\overline{z}(E)}. \tag{5.7}$$

Thus, given the invariant scaling of $\overline{z}(E)$, the relatively complex RFA-type measurements may no longer be necessary, and instead, single-shot Faraday-cup current traces may suffice to yield the full ion energy spectra.

5.3.3 Intensity dependence of charge-integrated ion energy spectra

The RFA charge-integrated energy distributions dN/dE are obtained by adding up the charge-resolved energy distributions of all charge states present in the experiment. Those distributions are akin to, and can be readily compared with, the flow velocity distributions obtained from hydrodynamic simulations such as the ones generated by the code RALEF-2D, and give access to the momentum and energy of the plasma ions.

Figure 5.6(a – g) shows measured pulse-energy-dependent ion energy spectra for a 27-µm diameter droplet and a 10 ns pulse duration. For ease of comparison, the spectra at minimum, medium, and maximum observation angle α are presented for the pulse energy extrema of 8 and 97 mJ in panel (h). First, we observe a spectral shift to higher energies with increasing laser energy at all angles. Second, at large angles ($\alpha \geq 90°$), we note an increasing number of ions with increasing laser energy. O'Connor *et al.* presented similar findings for the front-side ($\alpha < 90°$) emission using a planar target of solid tin [108]. A high-energy peak is also observed in spectra with an observation angle smaller than 120°. This peak is formed by the accumulation around the same kinetic energy of ions with charge state $z \leq 4$, as seen in section 5.3.1. The peak was reported [68, 109], and its physical origin examined [94, 114]. As the observation angle α increases, the peak loses its prominence and gradually fades into the smooth monotonously decaying background ion signal beyond $\alpha > 120°$.

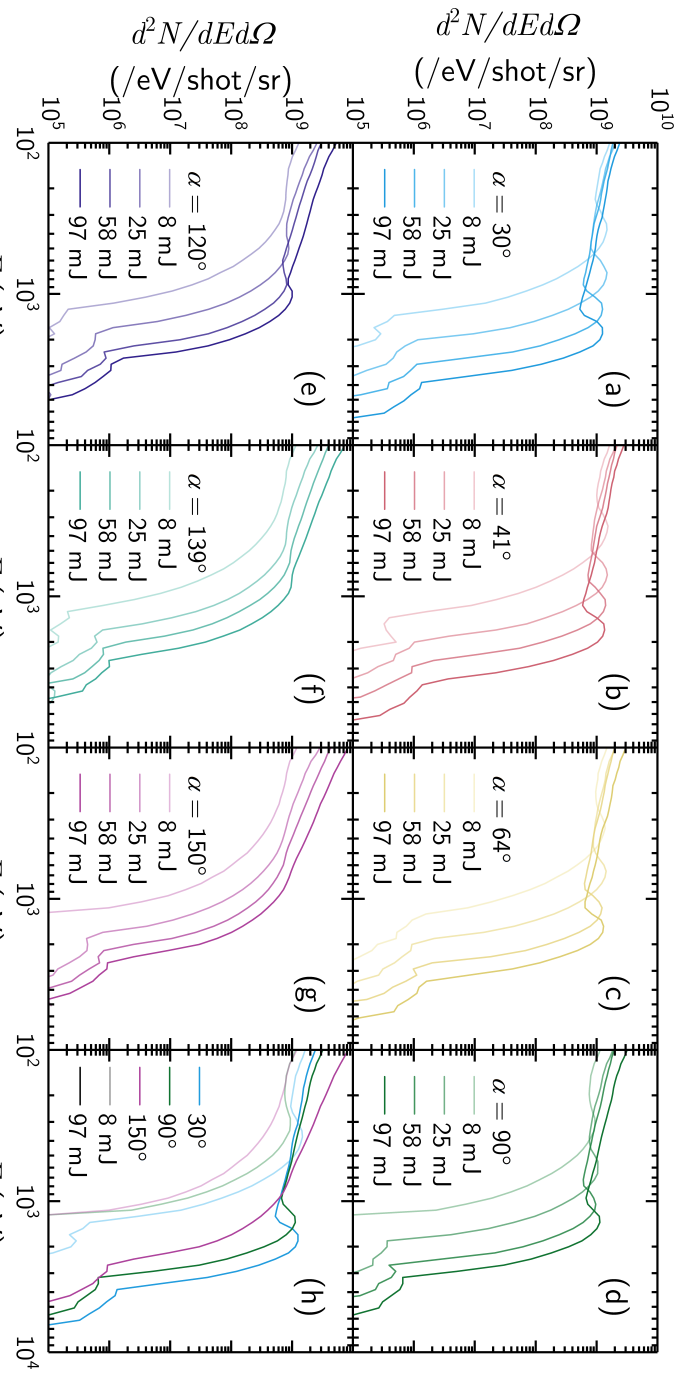

Figure 5.6: Measured ion energy distributions recorded at seven angles (panels (a – g)), for a 27 µm-diameter droplet and four different laser intensities. For comparison, ion spectra from a low (30°), medium (90°), and high angle (120°) are reproduced in panel (h) for lowest and highest laser pulse energies (E_{pulse} = 8 and 97 mJ respectively).

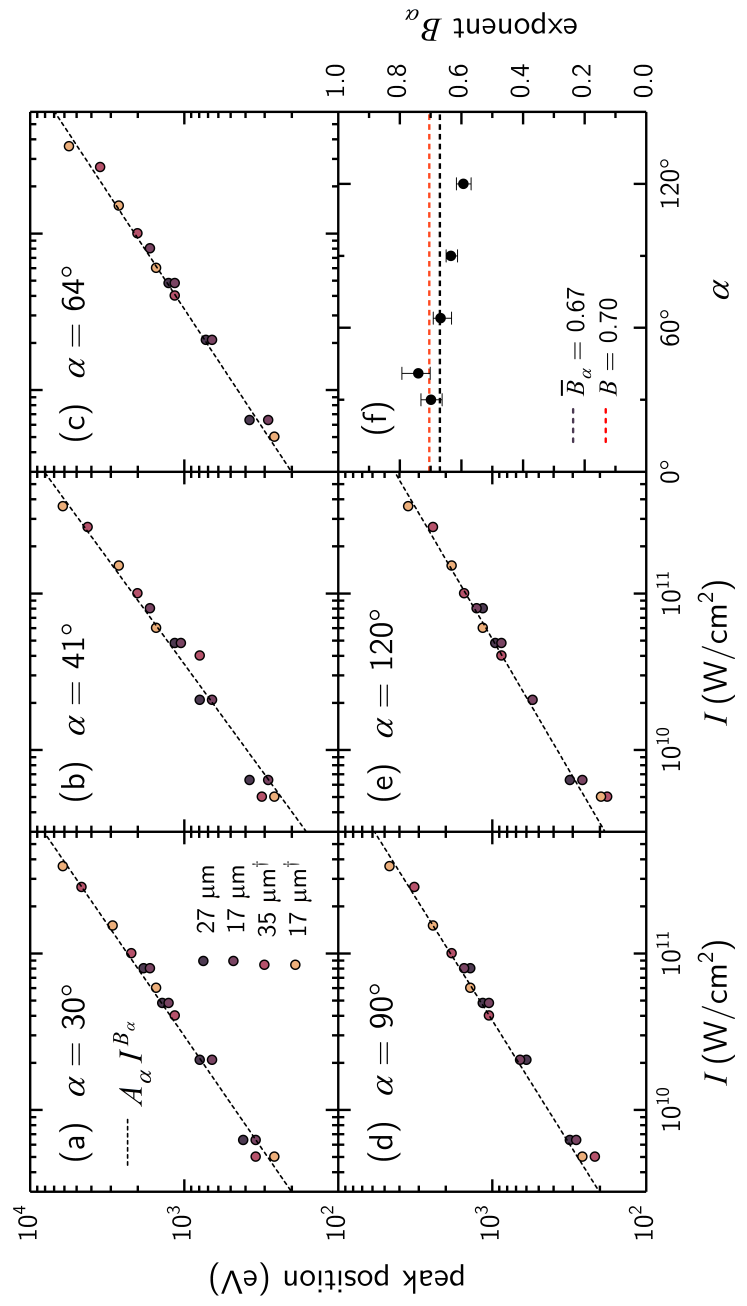

Figure 5.7: (a – e) High-energy peak energy from calculated energy spectra (see figure 5.6) as a function of laser pulse intensity for seven detection angles, three droplet diameters, and two laser pulse durations for the 17-µm diameter case.The collective intensity dependence is optimized with a power law scaling; panel (f) shows the exponent B_α for each angle α, their weighted average of 0.67 (black dashed line); the empirical ansatz (Eq. 5.9) estimate of 0.70 is also shown (red dashed line).

We investigate the frontward high-energy peak, namely its location on the energy axis. We find the position of the peak using a combination of direct numerical peak finding in dN/dE and looking for minima in d^2N/dE^2 (as before, the Python package `scipy` and its threshold-based peak finding routine is used here). The central peak energy shifts with laser intensity, which is shown in figure 5.7(a – e) (colored markers) for the five relevant angles (recall that the peak is observed only for $\alpha \leq 120°$), all four laser pulse energies, and all three droplet diameters of 17, 27 and 35 µm. To probe the influence of pulse duration (related to the Q-switch delay settings, see above), two 17 µm droplet diameter measurements are investigated, one using an 8 ns FWHM$_t$ and the other a longer 10 ns FWHM$_t$ laser pulse.

We observe a consistent power-law-like dependence ($A_\alpha E^{B_\alpha}$) of the high-energy peak position on laser intensity, with little deviation from the fitted power laws (dashed black lines in figure 5.7(a – e)). We find no significant difference between the short and long pulse cases for the 17 µm-diameter droplet. The exponents B_α of the power law fits are shown in figure 5.7(f). For each of the (a – d) panels, we also fit power law functions to data subsets containing three out of the four data sets. For each angle α, the maximum and minimum power law exponents obtained define error bars for B_α. In all spectra, there is a sub-linear dependence of the high-energy peak position with laser intensity, with exponents B_α ranging from 0.55 to 0.75, and an error-weighted average $\overline{B}_\alpha = 0.67(5)$.

Analytical scaling relations are used to establish the dependence of characteristic LPP ion energy E with laser intensity I. In addition to Eqs. 5.3 and 5.5 which yield $E \propto T^{1.6}$, Basko *et al.* [80] finds that

$$T \propto I^{0.44}, \tag{5.8}$$

where I is the laser intensity.

Inserting the relation between T and I in $E \propto T^{1.6}$ implies that E is proportional to $I^{0.7}$.

$$E \propto T^{1+0.60} \propto \left(I^{0.44}\right)^{1.60} \implies E \propto I^{0.70}. \tag{5.9}$$

The expected value of the power law exponent is remarkably close to the average angle-averaged experimental values of 0.67 reported in figure 5.7(f), for three different droplet target diameters. Moreover, the average intensity scaling exponent of the peak in the charge-integrated spectra matches precisely that of the second, high-energy peak in charge-resolved spectra obtained in section 5.3.1. This finding corroborates the formation of the peak in dN/dE through a bunching phenomenon.

Once again, we note that despite the remarkable differences observed in spectra taken at different angles, the power law scaling obtained by tracking features in the ion energy distribution presents a rather constant value over the angles [*cf.* Fig. 5.7(f)]. This observation holds for all studied set droplet sizes.

5.4 Conclusion

The effect of varying laser intensity on the ion emission from a tin LPP was examined. Energy, charge state, and emission angle of the ions are obtained using seven retarding field analyzers. Key spectral features were observed, such as a frontward high-energy peak in the charge-integrated energy distributions dN/dE, as reported previously [114], now seen to be formed by the accumulation of second peaks with fixed positions in the charge-state-resolved spectra. The energy corresponding to the high-energy peak was found to scale at all angles with $I^{0.67}$, in good agreement with empirical scaling laws proposed in literature. A common trend for the average charge state spectrum $\overline{z}(E)$ is seen in all the measurements at hand. Here again, empirical scaling laws appear to agree with the observed universal scaling although these laws cannot be expected to fully capture the relevant physics. Such universality of the scaling relation would be of great relevance, enabling the conversion of current-type ion energy distributions (dQ/dE) to flow-type ones (dN/dE). Moreover, this universal scaling hints at specific phenomena in the underlying physical process. To unravel the origin of the scaling, more work will be conducted on the recombination and charge exchange processes during the expansion of the LPP. The scaling relations of both average charge state and peak kinetic energy exhibit strong isotropy, while the underlying ion energy spectra themselves are highly anisotropic.

Acknowledgements

The authors thank Duncan Verheijde for his support in understanding and improving the RFA electronics. They also thank Jorijn Kuster for the indispensable software support of our experimental setups. This work has been carried out at the Advanced Research Center for Nanolithography (ARCNL). ARCNL is public-private partnership with founding partners UvA, VU, NWO-I and ASML, and associate partner RUG. This project has received funding from European Research Council (ERC) Starting Grant number 802648. This publication is part of the project New Light for Nanolithography (with project number 15697) of the research programme VIDI which is (partly) financed by the Dutch Research Council. This work made use of the Dutch national e-infrastructure with the support of the SURF Cooperative using grant no. EINF-2947.

chapter 6

Evidence of production of keV Sn^+ ions in the H_2 buffer gas surrounding a Sn-plasma EUV source

Subam Rai, Klaas I. Bijlsma, Lucas Poirier*, Emiel de Wit, Luc Assink, Adam Lassise, Ismanuel Rabadán, Luis Méndez, John Sheil, Oscar O. Versolato and Ronnie Hoekstra
Plasma Sources Science and Technology **32**, 035006 (2023).

Charge-state-resolved kinetic energy spectra of Sn ions ejected from a laser-produced plasma (LPP) of Sn have been measured at different densities of the H_2 buffer gas surrounding a micro-droplet LPP. In the absence of H_2, energetic keV Sn ions with charge states ranging from 4+ to 8+ are measured. For the H_2 densities used in the experiments no appreciable stopping or energy loss of the ions is observed. However, electron capture by Sn ions from H_2 results in a rapid shift towards lower charge states. At the highest H_2 pressure of 6×10^{-4} mbar, only Sn^{2+} and Sn^+ ions are measured. The occurrence of Sn^+ ions is remarkable due to the endothermic nature of electron capture by Sn^{2+} ions from H_2. To explain the production of keV Sn^+ ions, it is proposed that their generation is due to electron capture by metastable Sn^{2+*} ions. The gateway role of metastable Sn^{2+*} is underpinned by model simulations using atomic collision cross sections to track the charge states of Sn ions while traversing the H_2 buffer gas.

* LP participated in RFA data recording and analysis, produced the setup figure and took part in discussions.

6.1 Introduction

Sources of extreme ultraviolet (EUV) light are based on laser-produced plasma (LPP) of high temperatures (up to 50 eV) and high free electron densities (10^{19-21} cm^{-3}) in which highly charged ions are produced that are the atomic sources of the EUV radiation [7, 8]. For nanolithographic tools, the EUV wavelength of choice is 13.5 nm, which is dictated by the existence of high reflectivity multilayer optics [9, 10]. The element of choice for plasma generation of 13.5 nm radiation is Sn. Over a broad range of charge states (9+ to 15+), singly, doubly, and triply excited electronic configurations emit around 13.5 nm [11].

Subsequent to the desired production of EUV radiation, the plasma expands and generates energetic Sn ions [94], which if impacting on the EUV collector optics may affect the lifetime of the optics. The energy and charge state distributions of Sn ions coming from the LPP contain information on the expansion dynamics of the plasma itself [2, 12–14, 21]. Moreover, accurate data on the energy distributions facilitate the determination of the fraction of the total energy that is carried by the plasma ions [15].

Typically, the energy spectrum of the emitted Sn ions peaks at a few keV with tails that may extend to tens of keV [14], except for Sn^+ and Sn^{2+} which are barely observed at higher energies above 0.5 keV. When an LPP is embedded in a stopping gas, only low-charged Sn ions are observed at much lower energies, which is a direct signature of charge exchange and collisional stopping, energy transfer from the Sn particles to the stopping gas. In this paper, we address the initial stage of the charge and energy redistribution in which charge exchange is active but the energy loss to the stopping gas is still negligible. This separation can be made if the cross sections for charge exchange are much larger than the ones for significant kinetic-energy transfer. For Sn^{q+} ions with $q \geq 3$ this assumption is not debated but in the case of 1+ and 2+ ions, the charge transfer cross sections for the reactions

$$Sn^{2+} + H_2 \rightarrow Sn^+ + H_2^+, \tag{6.1}$$

and

$$Sn^+ + H_2 \rightarrow Sn + H_2^+, \tag{6.2}$$

are conventionally expected to be negligible because of the low scaled kinetic energies of the Sn ions ($\ll$ 100 eV/u) and the considerable endothermicity of the reactions. The Franck Condon ionization potential of H_2 is 16.1 eV [117, 118], while the ionization potentials of Sn^+ and Sn are 14.6 eV and 7.3 eV [119], respectively. Thus, resonant electron capture by Sn^{2+} is endothermic by 1.5 eV and in the case of Sn^+ by no less than 8.7 eV.

Remarkable enough while indeed no appreciable signs of charge transfer by singly charged Sn ions (Eq. (6.2)) are found we will show an efficient production of Sn^+ ions out of the

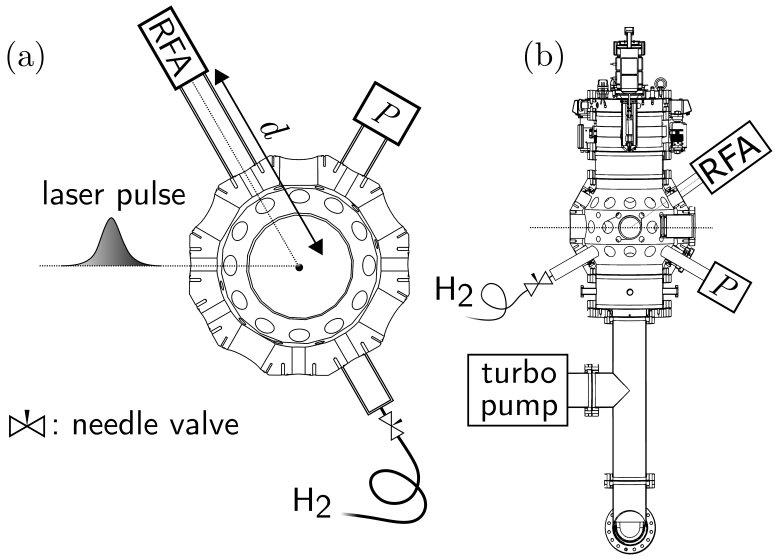

Figure 6.1: Schematic ((a): top view, (b): side view) of the LPP experiment to measure charge-state-specific ion spectra as a function of the pressure of the H_2 buffer gas embedding the LPP plasma. The distance d from plasma to the RFA type ion detector is 68.5 cm.

population of doubly charged Sn ions. Based on all available data the case is made that the Sn^+ ions are produced by electron capture by metastable Sn^{2+*} ions in the excited $[Kr]4d^{10}5s5p$ ^3P_J levels (the ground state of Sn^{2+} is $[Kr]4d^{10}5s^2\ ^1S_0$).

From an EUV source perspective, the actual abundances of singly and doubly charged Sn ions and thus, whether Sn^{2+} ions get converted by electron capture into Sn^+, impacts the Sn ion mitigation because the penetration depth of the Sn ions into the H_2 buffer gas depends on the stopping cross sections. Recent stopping measurements [51] hint at appreciably larger stopping powers for Sn^+ than for Sn^{2+} ions.

This paper is organized as follows. First, the laser-produced plasma source installed at ARCNL is briefly introduced with emphasis on the methods used to measure the charge-state dependent energy distributions of Sn^{q+} ions coming from the expanding LPP plasma. Thereafter the energy distributions as a function of the H_2 buffer gas are presented with a focus on the Sn^+ ions, which present the evidence of the occurrence of charge exchange by Sn^{2+} ions. Finally based on potential-energy curves and Landau-Zener type calculations it is discussed that electron capture from H_2 by metastable $Sn^{2+*}(^3P_J)$ ions is exothermic and likely to happen given the effective production of metastable $Sn^{2+*}(^3P)$ in collisions of Sn^{3+} on H_2.

6.2 Experiment: methodology and data

The LPP EUV source used for the present set of experiments has been described in detail before [27]. The parts and features most relevant to this work are briefly recalled here. A tin reservoir, which is kept at a temperature of 260° C, is mounted on top of a vacuum chamber with a background vacuum of 10^{-7} mbar. In the H_2 buffer gas runs, molecular hydrogen pressures covering the range from 6×10^{-5} to 6×10^{-4} mbar have been used. At a repetition rate of 25 kHz droplets of pure, molten tin are pushed through a nozzle into the vacuum chamber. The stream of microdroplets with a diameter of 27 µm, first traverse a light sheet generated by a He-Ne laser. After frequency down-conversion to 10 Hz, the light scattered off the Sn droplets is used to trigger a 10-Hz Nd:YAG laser which creates the Sn plasma. The Nd:YAG laser system is operated at a wavelength of 1064 nm and produces pulses of approximately 10 ns full-width at half-maximum (FWHM). The spatial beam profile is Gaussian and is focused to a spot size of 100 µm FWHM onto the droplets in the center of the chamber. A laser pulse energy of 200 mJ yielding a power density of 3×10^{11} W/cm^2 has been used in all experimental data presented in the following.

The energy distributions of the Sn^{q+} ions from the LPP are measured with a retarding field analyzer (RFA), more specifically a 4-grid Kimball Physics FC-73 RFA. The RFA is positioned at a distance of 68.5 cm from the LPP and at an angle of 64° with respect to the laser beam as illustrated in figure 6.1. The RFA is absolutely calibrated against an open, grid-less Faraday cup [109] to establish the integral transmission of the four grids. The same "bottom-up" method as introduced by Poirier *et al.* [109] is used to extract the kinetic-energy distributions for each individual charge state of tin ions from their joint overlapping energy distributions.

To interpret the ion energy spectra as a function of the H_2 pressure, one needs to know the relation between the pressure measured at the pressure gauge and the pressure (H_2 density) along the ions' trajectory from the laser-produced plasma to the ion detector. With the Monte-Carlo package MOLFLOW+ [120] developed at CERN, we have calculated the H_2 density within the entire LPP vacuum chamber and all its additional vacuum tubing and equipment. The results of this simulation are shown in figure 6.2. Along the ion path, the average relative H_2 density is seen to be just 3% higher than the density at the position of the pressure gauge and to change by a few percent only over the full distance of 68.5 cm. Therefore, taking a constant density along the ions' trajectory does not introduce significant errors when calculating charge state distributions along those trajectories. The largest uncertainty will stem from the absolute H_2 density calibration of the pressure gauge, which is given by the manufacturer as 30%.

The energy distributions for all eight charge states are presented in figure 6.3 for five

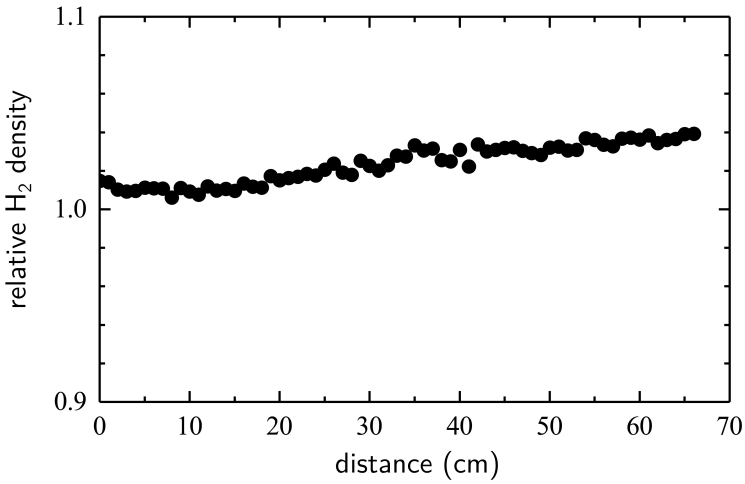

Figure 6.2: MOLFLOW+ Monte Carlo simulation results of the relative H_2 density, with respect to the density at the position of the pressure gauge, along the trajectory of Sn^{q+} ions flying from the laser-produced plasma in the center of the vacuum chamber to the RFA detector, positioned at 68.5 cm from that center.

different H_2 pressures. Sn ions in charge states up to 8+ are observed in the RFA measurements. Note that the results labeled 10^{-6} mbar are the reference measurements with no H_2 gas surrounding the LPP plasma. The main points to be noted are that the spectra of Sn^{8+}, Sn^{7+}, and Sn^{6+} are rather narrow, peak at approximately 2 keV, and disappear with increasing H_2 pressure. In the absence of H_2 gas (grey spectra in figure 6.3) the spectra of Sn^{3+}, Sn^{2+}, and Sn^{+} are seen to extend to maximum kinetic energies of 1 keV for Sn^{3+} and about 0.7 keV for Sn^{2+} and Sn^{+}. With increasing H_2 pressure a peak at 2 keV, similar to the 2-keV peak characterizing the Sn^{8+}, Sn^{7+}, and Sn^{6+} spectra, grows in into the Sn^{3+}, Sn^{2+}, and Sn^{+} spectra. Therefore the keV ions of Sn^{3+}, Sn^{2+}, and Sn^{+} observed in the energy spectra taken with a H_2 stopping gas around the LPP plasma must originate from Sn^{q+} ions with $q \geq 4$ by means of consecutive electron capture reactions. Last but not least, the emergence of energetic ($E \geq 1$ keV) Sn^{+} ions with increasing H_2 pressure is a clear sign that one-electron capture by Sn^{2+} (Eq. 6.1) is not blocked by an anticipated endothermicity of the reaction and moreover even has a significant cross section.

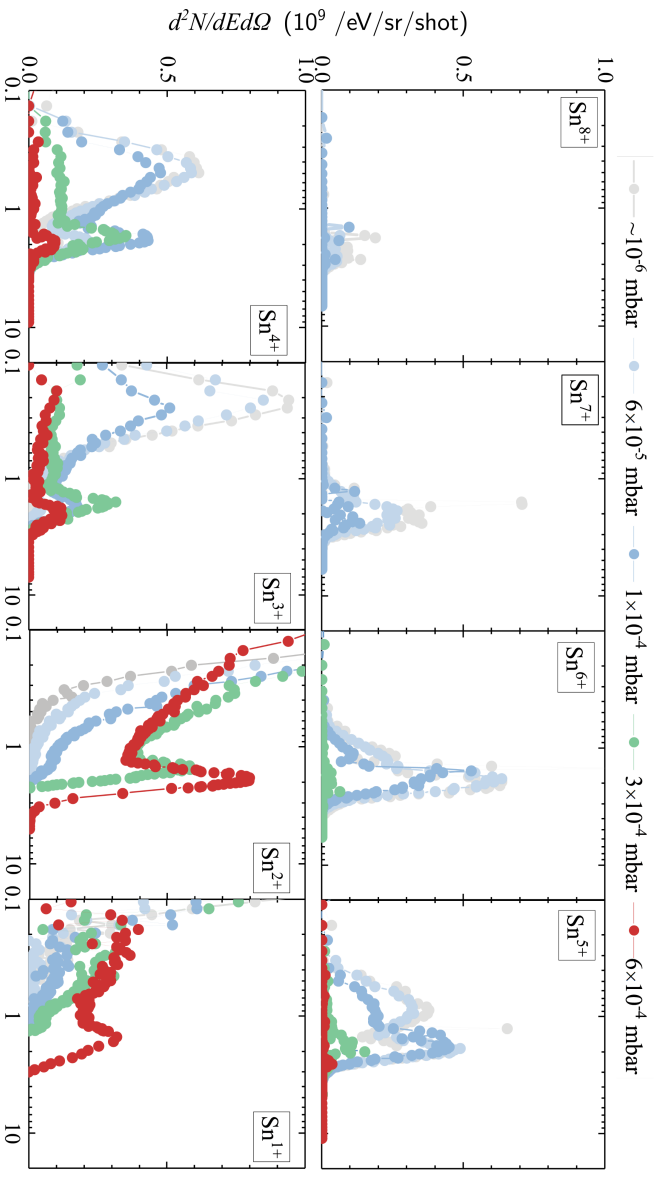

Figure 6.3: The yield of Sn^{q+} ions as a function of their kinetic energy in case of no H_2 gas and for H_2 buffer gas pressures in the range 6×10^{-5} to 6×10^{-4} mbar. The ions' flight path through the buffer gas is 68.5 cm.

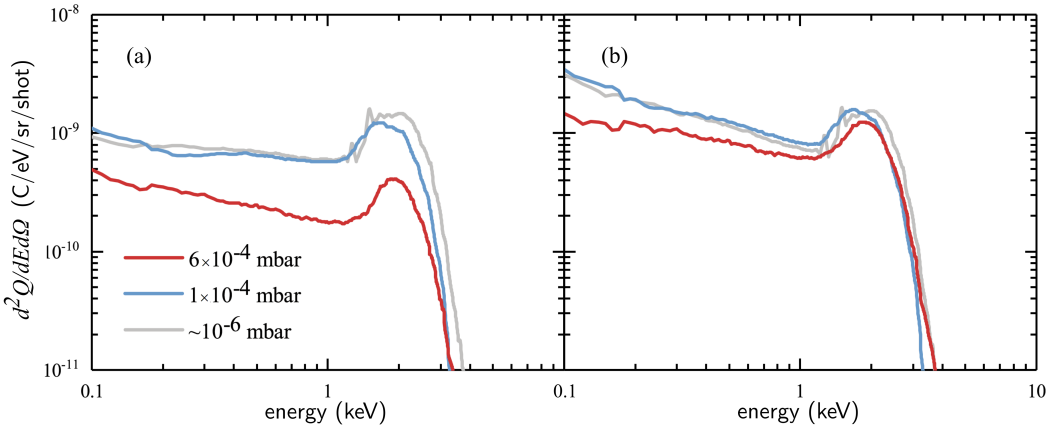

Figure 6.4: Panel (a) Total amount of charge as a function of Sn ion energy. Panel (b) Total number of ions as a function of Sn ion energy. Results are presented for no H_2 buffer gas present (labeled $\sim10^{-6}$ mbar) and buffer gas pressures of 1×10^{-4} and 6×10^{-4} mbar. The path length through the buffer gas is 68.5 cm.

6.3 Discussion

Before addressing the above points, one should realize that from an industrial source perspective, our experiments are performed at pressures representing the initial stages of the trajectories of Sn ions in the H_2 stopping gas after being ejected from the plasma. In this first phase, charge-exchange processes lower the average charge state of the ions rapidly before the ions have undergone appreciable energy loss. The validity of this approximation is implicit in the charge-state dependent energy spectra shown in figure 6.3 where the high energy peak is seen to remain at 2 keV whilst the charge state of the high energy ions decreases.

The reduction of average charge state without significant energy loss is illustrated in figure 6.4. This figure shows in its top panel the cumulative charge as a function of energy, while the bottom panel presents the number of particles as a function of energy. In the peak range (1 – 5 keV) the amount of charge measured at the RFA drops by approximately a factor of 4 when the H_2 pressure is raised to 6×10^{-4} mbar. In contrast to that the number of Sn ions having energies above 1 keV has not changed appreciably. The assumption that initially, charge transfer processes dominate over stopping and determine the changes in the charge-state dependent energy distributions therefore appears valid.

The pressure dependence of the particle-number distributions for all charge states from $q = 8$ down to $q = 1$ can be tracked by a set of eight differential equations of the type:

$$\frac{dN^{q+}}{dl} = n\sigma_{q+1\to q}N^{(q+1)+} - n\sigma_{q\to q-1}N^{q+}, \tag{6.3}$$

with N^{q+} the number of Sn ions in charge state $q+$, n the H_2 target density, $\sigma_{q\to q-1}$ the cross section for charge exchange from charge state $q+$ to $(q-1)+$, and l the position along the ion's trajectory. With the exception of Sn^{3+} [121], no charge exchange data is available for Sn^{q+} ions colliding on H_2. Therefore we decided to use the classical over-the-barrier model [122–124] to calculate estimates for $\sigma_{q\to q-1}$ cross sections for charge states $q \geq 4$ and which are found to be 62, 76, 88, 100, and 112 ($\times 10^{-16}$ cm^2) for 4+, 5+, 6+, 7+, and 8+ Sn ions, respectively. Cross sections obtained with the over-the-barrier model present typically an upper-limit cross section as the model assumes that for impact parameters smaller than a specific distance capture happens with 100% probability. For endothermic charge-transfer reactions cross sections are very small at low energies [125, 126], typically much smaller than 10^{-16} cm^2. To illustrate the contribution of a non-zero cross section for Sn^{2+} ions a cross section of 0.1×10^{-16} cm^2 has been used in the simulations. The results of a particle-number simulation are shown in figure 6.5. In line with the experimental data for energetic Sn ions ($E \geq 1$ keV) (see figure 6.3) the charge-state fractions of energetic Sn ions swap from $q \geq 4$ to $q < 3$ over the pressure range of 10^{-4} to 10^{-3} mbar. In contrast to the experimental data, which show a considerable (20%) fraction of 1+ ions at a pressure of 6×10^{-4} mbar, barely any Sn^+ ions are predicted. To obtain large Sn^+ populations matching the experimental data, a much larger cross section of order 10^{-15} cm^2 is required.

For an electron-capture reaction to have a large cross-section, the potential energy curves of the initial and final channels are required to cross one another at an internuclear distance between the ion and the target particle on the order of 10 a.u. A simplified picture, including only the Coulomb repulsion in the $Sn^+ - H_2^+$ exit channel, of the most relevant potential energy curves for $Sn^{2+} - H_2$ collisions is shown in figure 6.6.

In figure 6.6, the electronic potential energy of ground state $Sn^{2+}(5s^2\ ^1S)$ and H_2 is taken as reference for all other channels. As mentioned in the introduction the electron-capture channel $Sn^+(5s^2 5p\ ^2P) + H_2^+$ is endothermic by 1.5 eV at infinite internuclear distance between the particles. At shorter distances, due to the Coulomb repulsion between Sn^+ and H_2^+ the difference between both curves increases, and thus both potential energy curves do not cross underpinning the original idea of resonant electron capture from H_2 by ground state $Sn^{2+}(5s^2\ ^1S)$ not being possible.

For metastable $Sn^{2+}(5s5p\ ^3P)$ ions (Sn^{2+*}) the situation is very different. The $5s5p\ ^3P$ term lies about 7 eV (weighted average of the excitation energies of the $J = 0$, 1, and 2 levels of 6.64, 6.84, 7.34 eV, respectively [119]) above the ground state. Therefore at an internuclear distance R_c, there exists a curve crossing with the electron capture channel near 6 a.u., *cf.* figure 6.6. Using this distance, one might estimate using the "absorbing sphere"

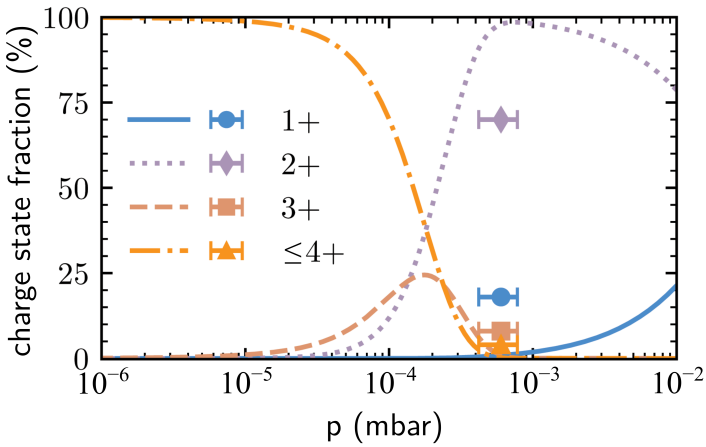

Figure 6.5: Simulated charge state fractions of energetic Sn^{q+} ions detected at a distance of 68.5 cm from the LPP plasma as a function of H_2 buffer pressure. For $q \geq 4$ the actual q specific fractions as measured at $p = 10^{-6}$ mbar (see figure 6.3) were used as input in solving the set of differential equations (equation 6.3). Solid points show the experimental LPP data.

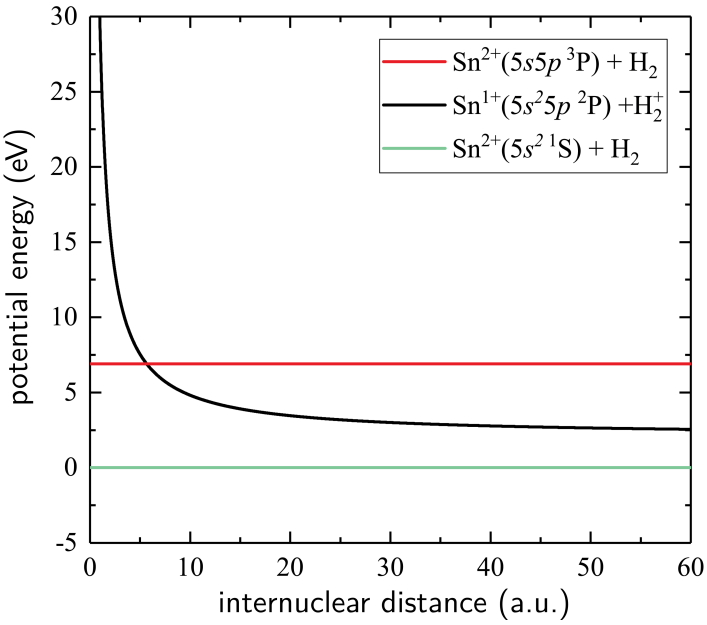

Figure 6.6: Schematic potential energy curves of relevant electronic channels in $Sn^{2+} - H_2$ collisions as a function of internuclear distance.

approximation [127, 128] a maximum cross section of 1.4×10^{-15} cm^2 ($= 0.45\pi R_c^2$). This cross section is of similar order of magnitude as the one for Sn^{3+} - H_2 collisions [121], which indicates that one-electron capture by metastable Sn^{2+} ions is a potential gateway to produce singly charged Sn^+ ions.

Metastable Sn^{2+*} ions as a source for the production of Sn^+ ions by means of electron capture obviously requires large abundances of metastable Sn^{2+*} ions. In keV collisions of Sn^{3+} ions on H_2 electron capture populates directly and at energies of a few keV almost solely ($\gg 95\%$) the metastable $Sn^{2+}(5s5p\ ^3P)$ term [121]. The latter point of the very high state selectivity of charge transfer in 1 to 10 keV Sn^{3+} on H_2 collisions was not explicitly discussed by Rai *et al.* [121] since in our earlier paper we focused on 10 to 100 keV collision energies. As shown above, all keV Sn ions of high charge state get rapidly converted to Sn^{3+} ions and which, by subsequent charge transfer, create metastable Sn^{2+*} ions. Metastable Sn^{2+*} are therefore abundantly produced in the stopping gas.

Transitions from the populated metastable $5s5p\ ^3P_{0,1,2}$ levels to the ground state $5s^2\ ^1S$ are spin forbidden. However, how long are their lifetimes with respect to the time between subsequent collisions? For $J = 0$ and $J = 2$, the transitions are also symmetry forbidden and thus the levels are expected to be very long-lived. While $J = 0$ to $J' = 0$ are truly forbidden, $J = 2$ to $J' = 0$ transitions still exhibit small transition probabilities [129]. To get an order of magnitude estimate of the lifetime of the $Sn^{2+}5s5p\ ^3P_2$ level, we performed a basic FAC (Flexible Atomic Code [130]) calculation. The calculation predicts a lifetime of the order of 10 – 100 s. This lifetime is very long compared to typical flight times in the experiment which are in the range of a few to a few tens of µs. For a heavy species such as Sn where the spin-orbit coupling is very significant, the $J = 1$ level is expected to have by far the shortest lifetime of the three levels of the ^3P term as it can decay via a $\Delta J = 1$ transition to the ground state. For the $^3P_1$ theoretical lifetimes are reported of approximately 100 [131], 150 [132] and 200 ns [133]. In a beam foil experiment, [134] the decay was not observed indicating that the lifetime is much longer than 45 ns, consistent with the theoretical values.

During a period of one lifetime of 150 ns (average of the reported values), a 2 keV Sn particle travels a distance of approximately 0.8 cm. For a first estimation of the role of $J = 1$ metastables, we take three times the lifetime, a period after which 95% of the $J = 1$ metastables has decayed to the ground state. The associated flight path of the 2 keV Sn particle is 2 cm. This path length should be compared to the mean free path (λ_F) of the particles which is equal to $(n\sigma_{21})^{-1}$. For the highest pressure used here of 6×10^{-4} mbar (1.5×10^{13} H_2 molecules per cm^3) and a σ_{21} of 10×10^{-16} cm^2 (discussed in the next paragraphs) one finds $\lambda_F \approx 67$ cm. Therefore only a very small fraction of the originally $J = 1$ metastables will undergo a collision with a H_2 molecule before having decayed to the ground state. Thus, in the experiments presented here the $J = 1$ metastables do not play an important role. Industrial sources operate at orders of magnitude higher H_2 pressures. For illustration, a

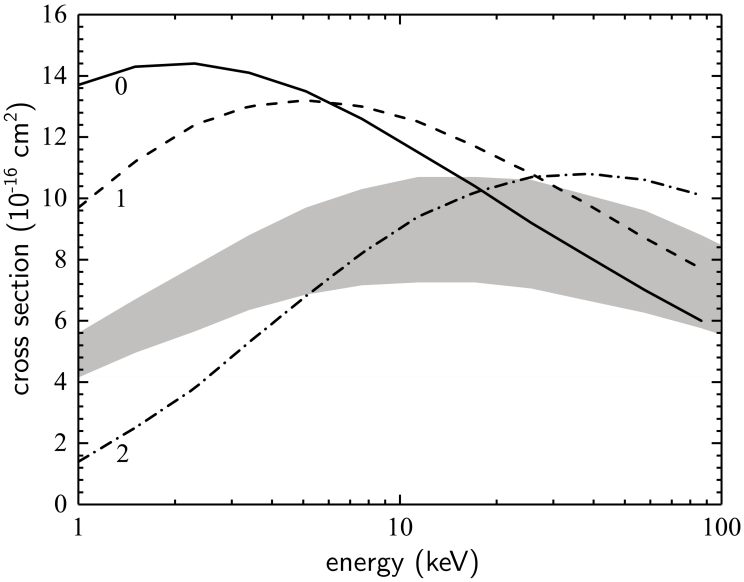

Figure 6.7: Cross sections for one-electron capture in 1 to 100 keV $Sn^{2+}(5s5p\ ^3P_J)$ collisions with H_2 according to our Landau-Zener model calculations. The solid, dashed, and dashed-dotted lines correspond to the J levels, with J is 0, 1, and 2, respectively. The grey band represents $(2J+1)$ weighted average cross sections, with the upper limits of the band assuming the $J = 1$ level fully contributing, and the lower limits of the band are defined by assuming no contribution by $J = 1$.

pressure of say 1 mbar corresponds to a mean free path λ_F of about 0.04 cm and therefore the opposite situation occurs where barely any of the $J = 1$ metastables have decayed.

For each of the three J levels we performed a basic 2-state Landau-Zener model calculation [135] to obtain J-dependent cross sections for electron capture by metastable Sn^{2+*} ions. For the coupling matrix element the generic form of the expression derived for atomic hydrogen targets [127] was used. However instead of the prefactor of 9.41 we used a prefactor of 5.48 as proposed by Kimura *et al.* [128] after optimization of Landau-Zener model calculations to their low-energy electron capture experiments on He. The J-dependent cross section results are summarized in figure 6.7.

To solve the set of differential equations, equation 6.3, the Sn^{2+*} population needs to be divided over its three J level populations. The J dependent populations are available from the theoretical studies in our earlier work [121]. As that data was not explicitly shown in our earlier work, it is presented here in figure 6.8. From the figure it is seen that the population is not statistical, only at the lowest collision energies the distribution tends towards a statistical one. For the simulations, an average energy of the Sn^{3+} ions of 2 keV is used, for which

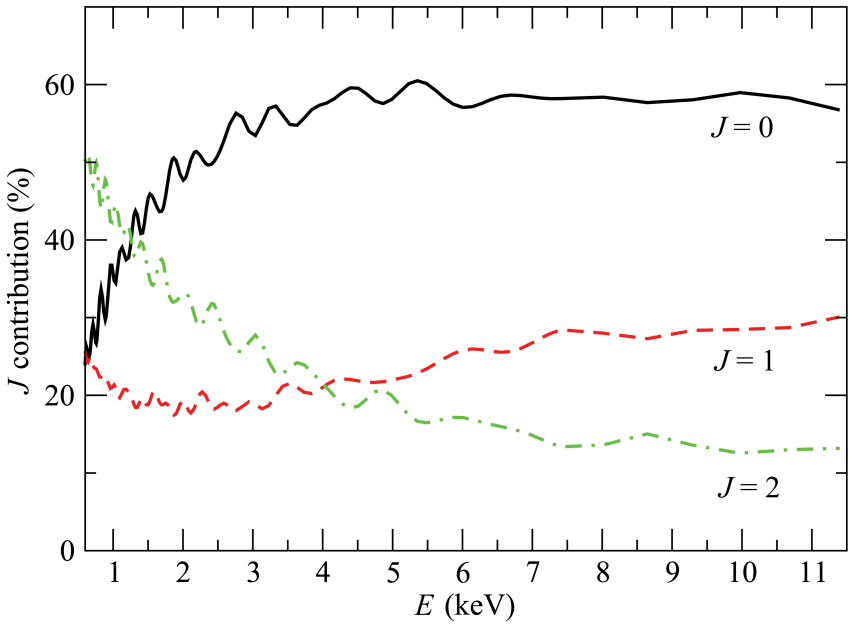

Figure 6.8: Calculated [121] J-dependent population fractions of the metastable $Sn^{2+*}(5s5p\ ^3P_J)$ levels produced by one-electron capture in Sn^{3+} collisions on H_2.

according to Fig. 6.8 the population fractions of J=0, 1, and 2 are 45%, 20%, and 35%.

In addition, for the $J = 1$ level it is assumed that it decays to the ground state before a next charge-changing collision occurs, thus with this $J = 1$ level we associate the Sn^{2+} ground state capture cross section. For $J = 0$ and 2 the calculated cross sections depicted in figure 6.7 are used. Figure 6.9 shows the results of the simulations which now explicitly include metastable Sn^{2+*} ions. As can be seen from the figure, a rapid increase of the fraction of Sn^{+} is predicted. Now with the inclusion of Sn^{2+*} metastables the charge state fractions at 6×10^{-4} mbar are in line with the experimental data. The simulations appear to indicate that the singly charged Sn ions get produced at pressures somewhat lower than seen in the experiment. However, this is likely a result of the fact that we have used upper limits for the electron capture cross sections for Sn ions in charge states of $q \geq 4$. Smaller cross sections will shift the curves in figure 6.9 to the right to higher pressures for as equation 6.3 indicates it is the product of target density and cross section that factors into the differential equations. For an optimal comparison between experiment and simulation, charge exchange cross sections for Sn^{q+} ions in charge states of $q \geq 4$ are called for. Nevertheless, the present simulations clearly highlight the key role of metastable Sn^{2+*} ions in the production of energetic keV Sn^{+} ions by means of consecutive charge exchange starting from energetic highly charged Sn^{q+} ions with charge states of $q \geq 4$ ejected from the laser-produced plasma into the surrounding H_2 buffer gas.

6.4 Conclusion

We have investigated the evolution of charge-state-resolved kinetic energy spectra of Sn ions ejected from a LPP of Sn as a function of the density of the H_2 buffer gas surrounding the plasma. Without H_2 being present, energetic 1 to 5 keV Sn ions in charge states of 4+ to 8+ are detected. Sn ions in lower charge states are absent at energies above 1 keV. However, at the highest H_2 pressure of 6×10^{-4} mbar, no highly charged Sn ions are measured anymore at energies above 1 keV, only Sn^{2+} and Sn^{+} ions are observed. The low-charged energetic Sn ions are produced by a series of consecutive electron capture processes. Therefore, in particular, the presence of Sn^{+} ions is remarkable because electron capture by Sn^{2+} ions from H_2 is endothermic and thus very unlikely to happen at keV energies, which from an atomic collision perspective are very low-energies. To explain the production of keV Sn^{+} ions, electron capture by metastable Sn^{2+*} ions is inferred. Previous work on Sn^{3+} - H_2 collisions [121] indicates that one-electron capture by Sn^{3+} ions populates primarily Sn^{2+} ions in metastable states. Using 2-state Landau Zener model cross sections for capture by the metastables, the key role of metastable Sn^{2+} is highlighted by model simulations using

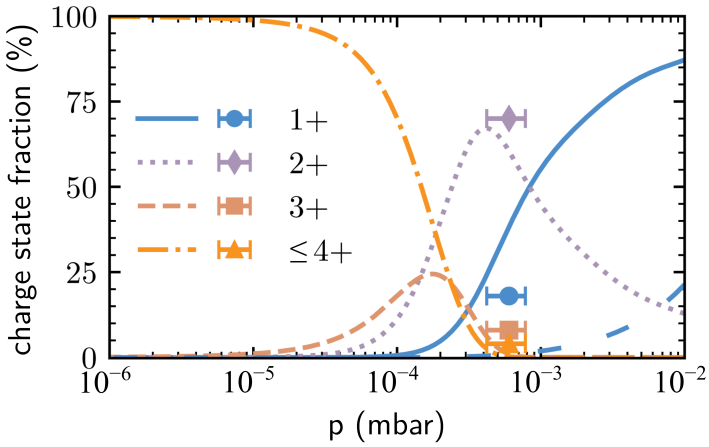

Figure 6.9: Simulated charge state distributions of energetic Sn^{q+} ions detected at a distance of 68.5 cm from the LPP plasma as a function of H_2 buffer pressures, assuming that all Sn^{2+} ions are produced in the metastable $5s5p\ ^3P$ term with a distribution over its J levels as shown in figure 6.8. For $q \geq 4$ the actual q specific fractions as measured at $p = 10^{-6}$ mbar (see figure 6.3) were used as input in solving the set of differential equations. For ease of comparison, the dashed blue line shows the Sn^+ ion fraction if no metastables are included (taken from figure 6.5). Solid points show the experimental LPP data.

atomic collision cross sections to track the charge states of Sn ions while traversing the H_2 buffer gas.

The production of Sn^+ ions in the buffer gas is of relevance from an industrial EUV source perspective. It shifts the charge state balance away from Sn^{2+} towards Sn^+. As Sn^+ ions have a larger stopping cross section than Sn^{2+} ions [51], the production of Sn^+ ions is beneficial to stopping Sn ions escaping from an LPP plasma in a high charge state.

Acknowledgements

This work is part of the research portfolio of the Advanced Research Center for Nanolithography (ARCNL), a public-private partnership between the University of Amsterdam (UvA), the Vrije Universiteit Amsterdam (VU), the University of Groningen (RuG), the Netherlands Organization for Scientific Research (NWO), and the semiconductor equipment manufacturer ASML. The project is co-financed by Holland High Tech with PPS allowance for research and development in the top sector HTSM. The theoretical work of IR and LM was partially supported by Ministerio de Economía and Competitividad (Spain), Project No. FIS2017-84684-R. The computational support by the Centro de Computación Científica of UAM is also acknowledged.

conclusion & outlook

In this Thesis, we developed diagnostics and related methods to characterize the ionic emission from laser-produced plasma. These diagnostic tools were subsequently applied in experimental campaigns. The results of these campaigns were compared to radiation-hydrodynamics modeling and analytical theory, leading to new insights about the expansion of plasma into the vacuum - and also into a buffer gas. In the following, the main conclusions from the individual chapters are first separately formulated, then synthesized into overarching findings and outlooks. A detailed discussion is presented on the topic of the scaling relation coupling the average charge state to kinetic energy.

In Chapters 1 and 3 we presented diagnostic tools to characterize plasma expansion. Chapter 1 introduced a charge- and energy-resolved spectrum of Sn ions produced by laser-driven microdroplet-tin plasma, using a time-of-flight mode calibrated electrostatic analyzer. The complete and successful calibration of the detector was described in detail. In Chapter 3, we described the full calibration of a retarding field analyzer for the characterization of tin LPPs. We outlined a post-processing method employed to produce charge-resolved ion spectra. The spectra were found to be in agreement with those produced previously using an electrostatic analyzer (of Chapter **??**), as well as with the charge-integrated spectra produced by an absolutely calibrated Faraday cup detector. We determined the retarding field analyzer to be more suitable than the electrostatic analyzer for assessing charge-resolved ion energy spectra: retarding field analyzers are less prone to misalignment and more convenient for angular characterization of the emission. Further developments of the RFA apparatus and

analysis method would benefit the interpretation of measurements, such as obtaining a more complete understanding of the complex transmission function of the four-grid stack and optimizing the charge and energy resolution of the device by adapting the RFA design.

The ion diagnostics were next applied in Chapters 2, 4, 5, and 6. In Chapter 2 we presented a first combined experimental and numerical study of an expanding tin laser-produced plasma. The ion kinetic energy spectrum produced by the single-fluid code RALEF-2D closely matches that produced by an electrostatic analyzer. The physical origins of a high-energy peak in the ion kinetic energy spectrum were explained using the numerical simulations: this high-energy feature is caused by the plowing of faster and denser plasma into slow plasma that was created at an earlier time. Having obtained new insight into the origins of the ion kinetic energy spectrum for a single emission angle, we next employed the retarding field analyzers and analysis method in Chapter 4 to probe ion kinetic energy spectra at seven observation angles around a tin LPP. A strong anisotropy of the ion emission was revealed, and a high-energy peak feature was observed in the spectra for small to medium observation angles. Measured ion energy spectra are in good agreement with those produced by the RALEF-2D code at all observation angles. Angular characterization of ion momentum yielded a front-back momentum imbalance, giving rise to a net velocity of the leftover liquid tin target. The velocities estimated from the momentum imbalance closely match those measured directly using shadowgraphy imaging of the target. Next, we examined the influence of drive laser intensity I on the ion kinetic energy spectra in Chapter 5. Charge-resolved and charge-integrated ion kinetic energy spectra were examined, revealing several scaling laws. Notably, the energy of the spectral peak feature previously reported was found to scale with $I^{0.7}$, in agreement with pre-existing analytical work. More importantly, we reported a constant scaling of the average charge state $\overline{z}(E)$ with kinetic energy, irrespective of laser intensity or observation angle. This finding is specifically addressed in a separate part of the Conclusions. Now that the plasma expansion into the vacuum was better understood from our work presented in the aforementioned Chapters, we turned to the study of the interaction of the expanding plasma ions with H_2 buffer gas that is present during the operation of an industrial plasma light source. Specifically, in Chapter 6 we studied the charge exchange interaction between tin ions, originating from an LPP, with a hydrogen buffer gas, with pressures between 1×10^{-6} and 6×10^{-4} mbar. Charge-resolved ion kinetic energy spectra were recorded using a retarding field analyzer. We reported a decreasing ion charge and constant total ion flow and total ion energy upon increasing the buffer gas pressure. The observation was attributed to the charge exchange process. No significant reduction of ion kinetic energy was observed for the probed buffer gas pressure regime. At the highest buffer gas pressures, only Sn^{2+} and Sn^{+} ions were detected. The occurrence of the singly charged Sn^{+} species here is surprising given that electron capture into the Sn^{2+} ground state is endothermic. The role of a metastable state in Sn^{2+} was found to be crucial for explaining our findings. These surprising results highlight

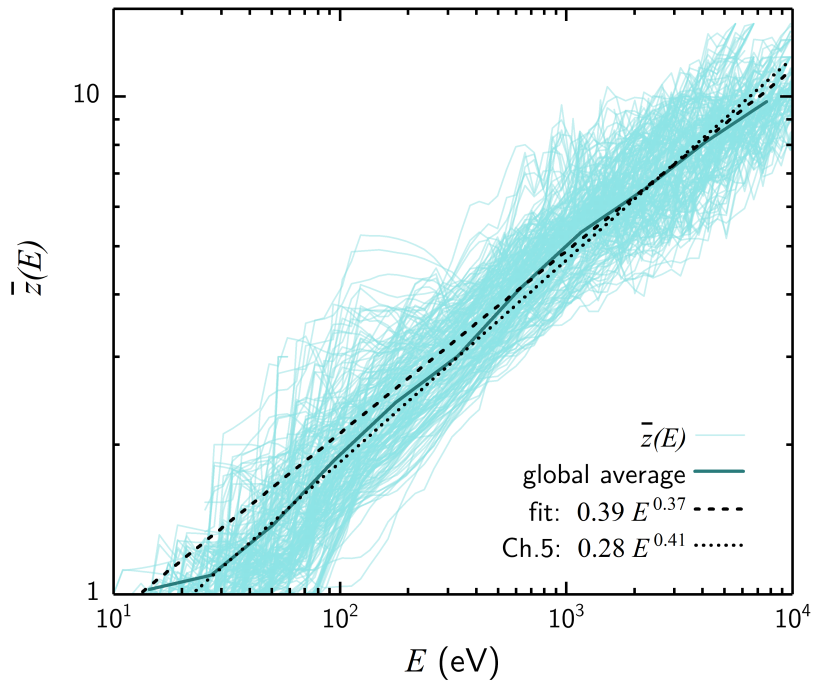

Figure 6.10: 225 $\bar{z}(E)$ traces corresponding to a vast parameter space (described in the text) are presented on the same graph. The global average $\bar{z}(E)$ is shown (dark blue line) as well as a power law fit of the global average trace (dashed black line). The dotted black line line is the power law fit of the $\bar{z}(E)$ presented in Chapter 5.

the need for a thorough and complete understanding of the physical mechanisms underlying charge exchange and collisions, in order to be able to accurately predict the stopping process that is key for the industry.

Outlook: the invariant $\bar{z}(E)$ scaling

An important observation was highlighted in Chapter 5: we found that a single power law was able to accurately capture the dependence of the average charge state $\bar{z}(E)$ on kinetic energy E. This scaling law was applicable for drive laser intensities ranging 0.4×10^{10} from to 40×10^{10} W/cm^2. Furthermore, the scaling law remained unchanged for seven observation angles ranging from 30° to 150°, despite the strong differences in the underlying ion kinetic energy spectra. In the following, we expand our look at $\bar{z}(E)$ to charge-resolved ion emission measurements over a much larger parameter space.

In figure 6.10, we show 225 $\overline{z}(E)$ traces (light blue lines) accounting for (i) one to seven observation angles ranging from 30° to 150°, (ii) drive laser wavelength of 1 and 2 µm, (iii) Gaussian and flat-top laser pulse temporal profile, (iv) laser pulse duration ranging from 6 to 13 ns (FWHM) for the Gaussian temporal profiles pulse, and 10 to 30 ns for the flat-top temporal profile pulse, (v) Gaussian and flat-top-like laser pulse spatial profile, (vi) laser spatial profile width from approximately 60 to 100 µm (FWHM) for the Gaussian spatial profiles pulse, and 85 to 110 µm for the flat-top spatial profile pulse, (vii) presence or absence of a 1 µm wavelength pre-pulse prior to the main drive pulse, meant to deform the tin droplet into a flat target, and (viii) droplet diameters ranging from approximately 17 to 85 µm. The $\overline{z}(E)$ traces were selected based on a single criterion: the charge-integrated spectrum dQ/dE constructed by adding up the charge-resolved dQ_z/dE distributions obtained via the bottom-up method (see Chapter 3) should match the dQ/dE distribution obtained via a Faraday-cup-like charge-integrated measurement, all across the kinetic energy spectrum, to sufficient accuracy. We also calculate the average $\overline{z}(E)$ spectrum (dark blue line) by binning the energy spectrum and calculating the average value of $\overline{z}(E)$ in each bin. An upward global trend with little deviation across the energy spectrum stands out. We empirically fit the global average with a power law function: the dashed black line represents the resulting $0.39E^{0.37}$ scaling. The global average matches closely the fitted power law over an energy range of almost two orders in magnitude, from 100 eV to a few keV. The fitted power law is quite similar to the one reported in Chapter 5 ($\overline{z}(E) = 0.28E^{0.41}$), also shown in figure 6.10 (dotted black line), further supporting the case for a universal scaling law.

A possible explanation for the observed universal scaling would be a "great equalizer" process, whereby the average ion charge of the expanding LPP decreases up to a freezing point, beyond which the average charge state spectrum remains in a steady state. As LPP expands in the vacuum, the average charge and energy of the ions are first set by a local temperature. Next, the ionic charge gradually decreases due to recombination processes while the velocity remains largely unaltered. When electron density drops during the expansion, recombination channels get quenched, and the average ionic charge stops decreasing. The main channels of recombination are three-body recombination, radiative recombination, and dielectric recombination. More work is needed to fully understand these channels and their respective rates, to elucidate the freezing of charges in expanding LPPs. Recombination dynamics are crucial for understanding the observed $\overline{z}(E)$ scaling.

The significance of a universal $\overline{z}(E)$ scaling is two-fold. First, we saw above that $\overline{z}(E)$ conceals precious information on the recombination dynamics of the expanding LPP. Second, we noted in Chapter 5 that $\overline{z}(E)$ is key to converting current-type ion energy distributions dQ/dE into flow-type ion energy distributions dN/dE, from which are derived total ion flow, ion momentum, and ion energy (see Chapter 4). A universal scaling would give access to this information in a very convenient manner, circumventing the measurement and post-processing

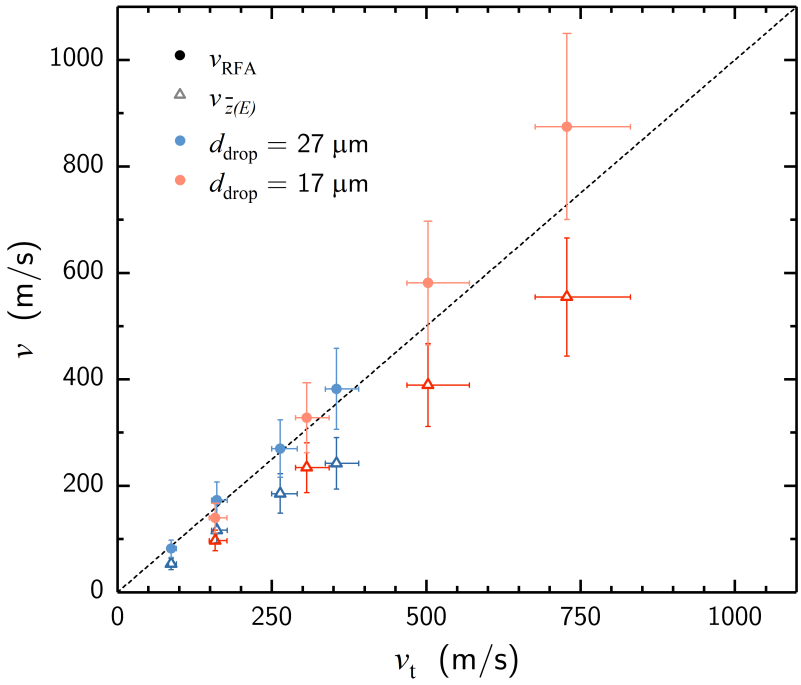

Figure 6.11: Tin target velocities measured through shadowgraphy (v_t), and calculated using the momentum imbalance derived from the RFA bottom-up method (light circles) and from current-type measurement and $\bar{z}(E)$ (empty dark triangles), for two droplet diameters. The dashed diagonal line denotes $v = v_t$.

methods described throughout the first part of the Thesis.

To support this point, we show in figure 6.11 the target velocities calculated using the method described in Chapter 4, using ion flow energy distributions calculated via the bottom-up method (dark circles), as well as those calculated using ion flow energy distributions calculated using an ion current measurement and the fitted universal scaling of $\bar{z}(E)$ (empty light triangles). Both calculated velocities are represented as a function of the velocities observed directly using a shadowgraphy imaging setup, as in Chapter 4. Measurements shown in figure 6.11 correspond to those presented in the figure 4.6 (see Chapter 4). We report that the two methods are in agreement, within the systematic uncertainties, even if the $\bar{z}(E)$ method in its first application appears to underestimate the actual velocity systematically somewhat. Thus, we find that we indeed may use simple Faraday Cup measurements (in tandem with the scaling law) to obtain the total ion momentum — and with it the speed of

the propelled droplet.

More work is needed to establish a possible universality of $\overline{z}(E)$ with physical arguments, starting with a more comprehensive understanding of the different ion recombination channels during the LPP expansion.

Opening with, and overcoming the challenge of accurate charged particle detection, this Thesis made its way to the description of beautiful and complex physical phenomena related to the expansion of laser-produced plasma. With due diligence, we calibrated ion detectors used for extensive laser-produced plasma experiment diagnostic, and elucidated the origin of the observed spectral features using radiative hydrodynamics simulations. The influence of laser intensity on ion emission was investigated, providing insight into the manipulation and shaping of ion energy spectra. The angle-resolved ion energy measurements enabled obtaining the full energy partitioning of LPPs over the dominant channels: (EUV) radiation and ion kinetics. Such measurements are now the standard of the ARCNL experiments towards next-generation LPP EUV sources. Additional important observations were enabled by the developed methods. They allowed for the discovery of an elegant relation between the kinetic energy and the average charge state of LPP ions. Also, our methodology raised and unraveled the enigma of the presence of energetic Sn^+ ions in the expansion of plasma in a buffer gas. With these results, we have found answers to the main research question: *What physical processes and what experimental parameters give structure to the kinetic energy and charge state distributions of the emitted ions?* The results presented in this Thesis furthermore will contribute to the development of future LPP-based light sources, and provide methodological ground for further investigations, enabling answering the corollary research question: *How can the ion emission be tailored for optimal EUV source performance and long-term fidelity?*

bibliography

[1]L. Wareham, U. Bubenheimer, and H. Lähnemann, *Passional of Christ and Antichrist: Antithesis of the Life of Christ and Antichrist in Pictures*, Treasures of the Taylorian Series One: Reformation Pamphlets (Taylor Institution Library, 2021).

[2]M. Murakami, Y.-G. Kang, K. Nishihara, S. Fujioka, and H. Nishimura, *Ion energy spectrum of expanding laser-plasma with limited mass*, Phys. Plasmas **12**, 062706 (2005).

[3]P. Mora, *Plasma expansion into a vacuum*, Phys. Rev. Lett. **90**, 185002 (2003).

[4]Y. Zel'dovich and Y. Raizer, *Physics of Shock Waves and High-Temperature Hydrodynamic Phenomena*, 2nd ed. (Academic Press, 1966).

[5]W. Li, X. Li, X. Li, Z. Hao, Y. Lu, and X. Zeng, *A review of remote laser-induced breakdown spectroscopy*, Appl. Spectrosc. Rev. **55**, 1–25 (2018).

[6]V. Malka, *Laser plasma accelerators*, Phys. Plasmas **19**, 055501 (2012).

[7]O. O. Versolato, *Physics of laser-driven tin plasma sources of EUV radiation for nanolithography*, Plasma Sources Sci. Tech. **28**, 083001 (2019).

[8]G. O'Sullivan, B. Li, R. D'Arcy, P. Dunne, P. Hayden, D. Kilbane, T. McCormack, H. Ohashi, F. O'Reilly, P. Sheridan, E. Sokell, C. Suzuki, and T. Higashiguchi, *Spectroscopy of highly charged ions and its relevance to EUV and soft x-ray source development*, J. Phys. B: At. Mol. Opt. Phys. **48**, 144025 (2015).

[9]S. Bajt, J. B. Alameda, T. W. Barbee Jr., W. M. Clift, J. A. Folta, B. Kaufmann, and E. A. Spiller, *Improved reflectance and stability of Mo-Si multilayers*, Opt. Eng. **41**, 1797–1804 (2002).

[10]Q. Huang, V. Medvedev, R. van de Kruijs, A. Yakshin, E. Louis, and F. Bijkerk, *Spectral tailoring of nanoscale EUV and soft x-ray multilayer optics*, Appl. Phys. Rev. **4**, 011104 (2017).

[11]F. Torretti, J. Sheil, R. Schupp, M. Basko, M. Bayraktar, R. Meijer, S. Witte, W. Ubachs, R. Hoekstra, O. O. Versolato, A. J. Neukirch, and J. Colgan, *Prominent radiative contributions from multiply-excited states in laser-produced tin plasma for nanolithography*, Nat. Commun. **11**, 2334 (2020).

[12]S. Fujioka, H. Nishimura, K. Nishihara, M. Murakami, Y.-G. Kang, Q. Gu, K. Nagai, T. Norimatsu, N. Miyanaga, Y. Izawa, K. Mima, Y. Shimada, A. Sunahara, and H. Furukawa, *Properties of ion debris emitted from laser-produced mass-limited tin plasmas for extreme ultraviolet light source applications*, Appl. Phys. Lett. **87**, 241503 (2005).

[13]M. J. Deuzeman, A. S. Stodolna, E. E. B. Leerssen, A. Antoncecchi, N. Spook, T. Kleijntjens, J. Versluis, S. Witte, K. S. E. Eikema, W. Ubachs, R. Hoekstra, and O. O. Versolato, *Ion distribution and ablation depth measurements of a fs-ps laser-irradiated solid tin target*, J. Appl. Phys. **121**, 103301 (2017).

[14]A. Bayerle, M. J. Deuzeman, S. van der Heijden, D. Kurilovich, T. de Faria Pinto, A. Stodolna, S. Witte, K. S. E. Eikema, W. Ubachs, R. Hoekstra, and O. O. Versolato, *Sn ion energy distributions of ns- and ps-laser produced plasmas*, Plasma Sources Sci. Technol. **27**, 045001 (2018).

[15]V. Bakshi, ed., *EUV Lithography*, 2nd ed. (SPIE Press, 2018).

[16]R. Dinger, K. Rohr, and H. Weber, *Ion distribution in laser produced plasma on tantalum surfaces at low irradiances*, J. Phys. B **13**, 2301 (1980).

[17]W. Demtröder and W. Jantz, *Investigation of laser-produced plasmas from metal-surfaces*, Plasma Phys. **12**, 691 (1970).

[18]I. V. Fomenkov, D. C. Brandt, A. N. Bykanov, A. I. Ershov, W. N. Partlo, D. W. Myers, N. R. Böwering, N. R. Farrar, G. O. Vaschenko, O. V. Khodykin, J. R. Hoffman, C. P. Chrobak, S. N. Srivastava, D. J. Golich, D. A. Vidusek, S. D. Dea, and R. R. Hou, *Laser-produced plasma light source for EUVL*, in Alternative Lithographic Technologies, Vol. 7271 (International Society for Optics and Photonics, Mar. 2009), pp. 852 –863.

[19]P. Yeates, C. Fallon, E. T. Kennedy, and J. T. Costello, *Charge resolved electrostatic diagnostic of colliding copper laser plasma plumes*, Phys. Plasmas **18**, 103104 (2011).

[20]R. A. Burdt, S. Yuspeh, K. L. Sequoia, Y. Tao, M. S. Tillack, and F. Najmabadi, *Experimental scaling law for mass ablation rate from a Sn plasma generated by a 1064 nm laser*, J. Appl. Phys. **106**, 033310 (2009).

[21]A. Z. Giovannini, N. Gambino, B. Rollinger, and R. S. Abhari, *Angular ion species distribution in droplet-based laser-produced plasmas*, J. Appl. Phys. **117**, 033302 (2015).

[22]M. Brandstätter, M. Weber, and R. Abhari, *Non-axisymmetric droplet irradiation effects on ion and extreme ultraviolet light emission of laser-produced plasma light sources*, J. Appl. Phys. **129**, 233306 (2021).

[23]O. Morris, A. O'Connor, E. Sokell, and P. Dunne, *Angular distribution of the ion emission from a tin-based laser-produced plasma extreme ultraviolet source*, Plasma Sources Sci. Technol. **19**, 025007 (2010).

[24]A. O'Connor, O. Morris, and E. Sokell, *Angular and energy distribution of Sn ion debris ejected from a laser-produced plasma source, for laser power densities in the range suitable for extreme ultraviolet lithography*, J. Appl. Phys. **109**, 073301–073301 (2011).

[25]J. Oberheide, P. Wilhelms, and M. Zimmer, *New results on the absolute ion detection efficiencies of a microchannel plate*, Meas. Sci. and Technol. **8**, 351–354 (1997).

[26]M. Krems, J. Zirbel, M. Thomason, and R. D. DuBois, *Channel electron multiplier and channelplate efficiencies for detecting positive ions*, Rev. Sci. Instrum. **76**, 093305 (2005).

[27]D. Kurilovich, A. L. Klein, F. Torretti, A. Lassise, R. Hoekstra, W. Ubachs, H. Gelderblom, and O. O. Versolato, *Plasma propulsion of a metallic microdroplet and its deformation upon laser impact*, Phys. Rev. Appl. **6**, 014018 (2016).

[28]E. H. A. Granneman and M. J. van der Wiel, "Transport, dispersion and detection of electrons, ions and neutrals", in *Handbook on synchrotron radiation*, edited by E. E. Koch (North-Holland, 1983) Chap. 6, pp. 368–462.

[29]J. W. Müller, *Dead-time problems*, Nucl. Instrum. Meth. **112**, 47–57 (1973).

[30]J. W. Müller, *Generalized dead times*, Nucl. Instrum. Meth. Phys. Res. A. **301**, 543–551 (1991).

[31]D. F. Yu and J. A. Fessler, *Mean and variance of single photon counting with deadtime*, Phys. Med. Biol. **45**, 2043–2056 (2000).

[32]J. Lee, I. Kim, and H. Choi, *On the dead time problem of a GM counter*, Appl. Radiat. Isot. **67**, 1094–1098 (2009).

[33]L. Abbene and G. Gerardi, *High-rate dead-time corrections in a general purpose digital pulse processing system*, J. Synchrotron Radiat. **22**, 1190–1201 (2015).

[34]S. H. Lee and R. P. Gardner, *A new G-M counter dead time model*, Appl. Radiat. and Isot. **53**, 731–737 (2000).

[35]R. A. Baragiola, E. V. Alonso, and A. O. Florio, *Electron emission from clean metal surfaces induced by low-energy light ions*, Phys. Rev. B **19**, 121–129 (1979).

[36]N. Takahashi, Y. Adachi, M. Saito, and Y. Haruyama, *Absolute detection efficiencies for keV energy atoms incident on a microchannel plate detector*, Nucl. Instr. and Meth. Phys. Res. B **315**, 51–54 (2013).

[37]H. D. Hagstrum, *Theory of Auger Ejection of Electrons from Metals by Ions*, Phys. Rev. **96**, 336–365 (1954).

[38]A. Arnau, F. Aumayr, P. Echenique, M. Grether, W. Heiland, J. Limburg, R. Morgenstern, P. Roncin, S. Schippers, R. Schuch, N. Stolterfoht, P. Varga, T. Zouros, and H. Winter, *Interaction of slow multicharged ions with solid surfaces*, Surface Science Reports **27**, 113–239 (1997).

[39]T. Schlathölter, R. Hoekstra, and R. Morgenstern, *Collisions of O^{q+} with neutral C_{60}: charge transfer and fragmentation*, J. Phys. B **31**, 1321 (1998).

[40]I. Fomenkov, D. Brandt, A. Ershov, A. Schafgans, Y. Tao, G. Vaschenko, S. Rokitski, M. Kats, M. Vargas, M. Purvis, R. Rafac, B. La Fontaine, S. De Dea, A. LaForge, J. Stewart, S. Chang, M. Graham, D. Riggs, T. Taylor, M. Abraham, and D. Brown, *Light sources for high-volume manufacturing euv lithography: technology, performance, and power scaling*, Adv. Opt. Techn. **6**, 173–186 (2017).

[41]D. C. Brandt, I. Fomenkov, and J. Stewart, *Progress in availably of NXE:3400B EUVL sources in the field and power scaling towards 500W (Conference Presentation)*, in Extreme Ultraviolet (EUV) Lithography XI, Vol. 11323, edited by N. M. Felix and A. Lio (International Society for Optics and Photonics, 2020).

[42]W. Svendsen and G. O'Sullivan, *Statistics and characteristics of XUV transition arrays from laser-produced plasmas of the elements tin through iodine*, Phys. Rev. A **50**, 3710–3718 (1994).

[43]P. Hayden, A. Cummings, N. Murphy, G. O'Sullivan, P. Sheridan, J. White, and P. Dunne, *13.5 nm extreme ultraviolet emission from tin based laser produced plasma sources*, J. Appl. Phys. **99**, 093302 (2006).

[44]R. Schupp, F. Torretti, R. Meijer, M. Bayraktar, J. Scheers, D. Kurilovich, A. Bayerle, K. Eikema, S. Witte, W. Ubachs, R. Hoekstra, and O. O. Versolato, *Efficient Generation of Extreme Ultraviolet Light From Nd:YAG-Driven Microdroplet-Tin Plasma*, Phys. Rev. Appl. **12**, 014010 (2019).

[45]A. Sasaki, A. Sunahara, H. Furukawa, K. Nishihara, S. Fujioka, T. Nishikawa, F. Koike, H. Ohashi, and H. Tanuma, *Modeling of radiative properties of Sn plasmas for extreme-ultraviolet source*, J. Appl. Phys. **107**, 113303 (2010).

[46]A. N. Ryabtsev and E. Y. Kononov, *Resonance transitions in the Pd VII spectrum*, Phys. Scr. **85**, 025301 (2012).

[47]J. Colgan, D. Kilcrease, J. Abdallah, M. Sherrill, C. Fontes, P. Hakel, and G. Armstrong, *Atomic structure considerations for the low-temperature opacity of Sn*, High Energy Density Phys. **23**, 133 –137 (2017).

[48]J. Scheers, C. Shah, A. Ryabtsev, H. Bekker, F. Torretti, J. Sheil, D. A. Czapski, J. C. Berengut, W. Ubachs, J. R. C. López-Urrutia, R. Hoekstra, and O. O. Versolato, *EUV spectroscopy of highly charged* Sn^{13+} – Sn^{15+} *ions in an electron-beam ion trap*, Phys. Rev. A **101**, 062511 (2020).

[49]K. Nishihara, A. Sunahara, A. Sasaki, M. Nunami, H. Tanuma, S. Fujioka, Y. Shimada, K. Fujima, H. Furukawa, T. Kato, F. Koike, R. More, M. Murakami, T. Nishikawa, V. Zhakhovskii, K. Gamata, A. Takata, H. Ueda, H. Nishimura, Y. Izawa, N. Miyanaga, and K. Mima, *Plasma physics and radiation hydrodynamics in developing an extreme ultraviolet light source for lithography*, Phys. Plasmas **15**, 056708 (2008).

[50]D. Nakamura, K. Tamaru, Y. Hashimoto, T. Okada, H. Tanaka, and A. Takahashi, *Mitigation of fast ions generated from laser-produced Sn plasma for extreme ultraviolet light source by H2 gas*, J. Appl. Phys. **102**, 123310 (2007).

[51]D. B. Abramenko, M. V. Spiridonov, P. V. Krainov, V. M. Krivtsun, D. I. Astakhov, V. V. Medvedev, M. van Kampen, D. Smeets, and K. N. Koshelev, *Measurements of hydrogen gas stopping efficiency for tin ions from laser-produced plasma*, Appl. Phys. Lett. **112**, 164102 (2018).

[52]S. S. Harilal, B. O'Shay, and M. S. Tillack, *Debris mitigation in a laser-produced tin plume using a magnetic field*, J. Appl. Phys. **98**, 036102 (2005).

[53]Y. Ueno, G. Soumagne, A. Sumitani, A. Endo, T. Higashiguchi, and N. Yugami, *Reduction of debris of a* CO_2 *laser-produced Sn plasma extreme ultraviolet source using a magnetic field*, Appl. Phys. Lett. **92**, 211503 (2008).

[54]H. Mizoguchi, H. Nakarai, T. Abe, H. Tanaka, Y. Watanabe, T. Hori, Y. Shiraishi, T. Yanagida, G. Soumagne, T. Yamada, and T. Saitou, *Challenge of >300W high power LPP-EUV source with long collector mirror lifetime for semiconductor HVM*, in Extreme Ultraviolet (EUV) Lithography XI, Vol. 11323, edited by N. M. Felix and A. Lio (International Society for Optics and Photonics, 2020), pp. 225 –238.

[55]A. S. Stodolna, T. de Faria Pinto, F. Ali, A. Bayerle, D. Kurilovich, J. Mathijssen, R. Hoekstra, O. O. Versolato, K. S. E. Eikema, and S. Witte, *Controlling ion kinetic energy distributions in laser produced plasma sources by means of a picosecond pulse pair*, J. Appl. Phys. **124**, 053303 (2018).

[56]A. Roy, S. S. Harilal, M. P. Polek, S. M. Hassan, A. Endo, and A. Hassanein, *Influence of laser pulse duration on extreme ultraviolet and ion emission features from tin plasmas*, Phys. Plasmas **21**, 033109 (2014).

[57]R. A. Burdt, Y. Tao, M. S. Tillack, S. Yuspeh, N. M. Shaikh, E. Flaxer, and F. Najmabadi, *Laser wavelength effects on the charge state resolved ion energy distributions from laser-produced Sn plasma*, J. App. Phys. **107**, 043303 (2010).

[58]D. Campos, S. S. Harilal, and A. Hassanein, *The effect of laser wavelength on emission and particle dynamics of Sn plasma*, J. Appl. Phys. **108**, 113305 (2010).

[59]T. Higashiguchi, C. Rajyaguru, N. Dojyo, Y. Taniguchi, K. Sakita, S. Kubodera, and W. Sasaki, *Debris characteristics of a laser-produced tin plasma for extreme ultraviolet source*, Rev. Sci. Instrum. **76**, 126102 (2005).

[60]O. Morris, F. O'Reilly, P. Dunne, and P. Hayden, *Angular emission and self-absorption studies of a tin laser produced plasma extreme ultraviolet source between 10 and 18 nm*, Appl. Phys. Lett. **92**, 2006–2009 (2008).

[61]O. Morris, A. O'Connor, E. Sokell, and P. Dunne, *Angular distribution of the ion emission from a tin-based laser-produced plasma extreme ultraviolet source*, Plasma Sources Sci. Tech. **19**, 025007 (2010).

[62]A. O'Connor, O. Morris, and E. Sokell, *Angular and energy distribution of Sn ion debris ejected from a laser-produced plasma source, for laser power densities in the range suitable for extreme ultraviolet lithography*, J. Appl. Phys. **109**, 073301 (2011).

[63]Y. Tao and M. S. Tillack, *Mitigation of fast ions from laser-produced Sn plasma for an extreme ultraviolet lithography source*, Appl. Phys. Lett. **89**, 111502 (2006).

[64]Y. Tao, M. S. Tillack, S. S. Harilal, K. L. Sequoia, and F. Najmabadi, *Investigation of the interaction of a laser pulse with a preformed gaussian Sn plume for an extreme ultraviolet lithography source*, J. Appl. Phys. **101**, 023305 (2007).

[65]R. A. Burdt, Y. Ueno, Y. Tao, S. Yuspeh, M. S. Tillack, and F. Najmabadi, *Recombination effects during expansion into vacuum in laser produced Sn plasma*, App. Phys. Lett. **97**, 041502 (2010).

[66]R. Schupp, F. Torretti, R. A. Meijer, M. Bayraktar, J. Sheil, J. Scheers, D. Kurilovich, A. Bayerle, A. A. Schafgans, M. Purvis, K. S. E. Eikema, S. Witte, W. Ubachs, R. Hoekstra, and O. O. Versolato, *Radiation transport and scaling of optical depth in Nd:YAG laser-produced microdroplet-tin plasma*, Appl. Phys. Lett. **115**, 124101 (2019).

[67]L. Behnke, R. Schupp, Z. Bouza, M. Bayraktar, Z. Mazzotta, R. Meijer, J. Sheil, S. Witte, W. Ubachs, R. Hoekstra, and O. O. Versolato, *Extreme ultraviolet light from a tin plasma driven by a 2-μm-wavelength laser*, Opt. Express **29**, 4475–4487 (2021).

[68]L. Poirier, A. Bayerle, A. Lassise, F. Torretti, R. Schupp, L. Behnke, Y. Mostafa, W. Ubachs, O. O. Versolato, and R. Hoekstra, *Cross-calibration of a combined electrostatic and time-of-flight analyzer for energy- and charge-state-resolved spectrometry of tin laser-produced plasma*, Appl. Phys. B **128**, 39 (2021).

[69]M. Murakami, S. Fujioka, H. Nishimura, T. Ando, N. Ueda, Y. Shimada, and M. Yamaura, *Conversion efficiency of extreme ultraviolet radiation in laser-produced plasmas*, Phys. Plasmas **13**, 033107 (2006).

[70]A. Sunahara and K. Tanaka, *Atomic number Z dependence of dynamics of laser-ablated materials*, Fusion Engineering and Design **85**, 935–939 (2010).

[71]A. Sunahara, A. Sasaki, and K. Nishihara, *Two dimensional radiation hydrodynamic simulation for extreme ultra-violet emission from laser-produced tin plasmas*, J. Phys.: Conf. Ser. **112**, 042048 (2008).

[72]K. Koshelev, V. Ivanov, V. Medvedev, V. M. Krivtsun, V. G. Novikov, and A. S. Grushin, *Return-to-zero line code modeling of distributed tin targets for laser-produced plasma sources of extreme ultraviolet radiation*, J. Micro. Nanolithogr. MEMS MOEMS **11**, 1–7 (2012).

[73]V. Sizyuk, A. Hassanein, and T. Sizyuk, *Three-dimensional simulation of laser-produced plasma for extreme ultraviolet lithography applications*, J. App. Phys. **100**, 103106 (2006).

[74]A. Sunahara, private communication (2021).

[75]R. Hockney and J. Eastwood, *Computer Simulations Using Particles* (McGraw-Hill, 1981).

[76]C. K. Birdsall and A. B. Langdon, *Plasma Physics via Computer Simulation, Series in Plasma Physics* (Taylor and Francis, 1991).

[77]K. Germaschewski, W. Fox, S. Abbott, N. Ahmadi, K. Maynard, L. Wang, H. Ruhl, and A. Bhattacharjee, *The plasma simulation code: a modern particle-in-cell code with patch-based load-balancing*, J. Comp. Phys. **318**, 305–326 (2016).

[78]A. Tauschwitz, M. Basko, A. Frank, V. Novikov, A. Grushin, A. Blazevic, M. Roth, and J. Maruhn, *2D radiation-hydrodynamics modeling of laser-plasma targets for ion stopping measurements*, High Energy Density Phys. **9**, 158–166 (2013).

[79]S. Faik, A. Tauschwitz, M. M. Basko, J. A. Maruhn, O. Rosmej, T. Rienecker, V. G. Novikov, and A. S. Grushin, *Creation of a homogeneous plasma column by means of hohlraum radiation for ion-stopping measurements*, High Energy Density Phys. **10**, 47–55 (2014).

[80]M. M. Basko, V. G. Novikov, and A. S. Grushin, *On the structure of quasi-stationary laser ablation fronts in strongly radiating plasmas*, Phys. Plasmas **22**, 053111 (2015).

[81]M. Basko, *On the maximum conversion efficiency into the 13.5-nm extreme ultraviolet emission under a steady-state laser ablation of tin microspheres*, Phys. Plasmas **23**, 083114 (2016).

[82]M. M. Basko, M. S. Krivokorytov, A. Y. Vinokhodov, Y. V. Sidelnikov, V. M. Krivtsun, V. V. Medvedev, D. A. Kim, V. O. Kompanets, A. A. Lash, and K. N. Koshelev, *Fragmentation dynamics of liquid–metal droplets under ultra-short laser pulses*, Laser. Phys. Lett. **14**, 036001 (2017).

[83]D. Kurilovich, M. M. Basko, D. A. Kim, F. Torretti, R. Schupp, J. C. Visschers, J. Scheers, R. Hoekstra, W. Ubachs, and O. O. Versolato, *Power-law scaling of plasma pressure on laser-ablated tin microdroplets*, Phys. Plasmas **25**, 012709 (2018).

[84]J. K. Dukowicz, M. C. Cline, and F. L. Addessio, *A general topology Godunov method*, J. Comp. Phys. **82**, 29–63 (1989).

[85]F. L. Addessio, J. R. Baumgardner, J. K. Dukowicz, N. L. Johnson, B. A. Kashiwa, R. M. Rauenzahn, and C. Zemach, *CAVEAT: A computer code for fluid dynamics problems with large distortion and internal slip*, May Report No. LA-10613-MS-Rev. 1, UC-32, Los Alamos National Laboratory, 1992.

[86]E. Livne and A. Glasner, *A finite difference scheme for the heat conduction equation*, J. Comp. Phys. **58**, 59–66 (1985).

[87]A. F. Nikiforov, V. G. Novikov, and V. B. Uvarov, *Quantum-Statistical Models of Hot Dense Matter: Methods for Computation Opacity and Equation of State (Progress in Mathematical Physics)* (Birkhauser, 2005).

[88]V. G. Novikov, V. V. Ivanov, K. N. Koshelev, V. M. Krivtsun, and A. D. Solomyannaya, *Calculation of tin emission spectra in discharge plasma: the influence of reabsorption in spectral lines*, High Energy Density Phys. **3**, 198–203 (2007).

[89]S. Faik, A. Tauschwitz, and I. Iosilevskiy, *The equation of state package FEOS for high energy density matter*, Comp. Phys. Comm. **227**, 117–125 (2018).

[90]M. M. Basko, *A model for the conversion of ion-beam energy into thermal radiation*, Phys. Fluids B **4**, 3753–3763 (1992).

[91]B. Liu, R. Meijer, J. Hernandez-Rueda, D. Kurilovich, Z. Mazzotta, S. Witte, and O. O. Versolato, *Laser-induced vaporization of a stretching sheet of liquid tin*, English, J. Appl. Phys. **129**, 1–6 (2021).

[92]S. Reijers, D. Kurilovich, F. Torretti, H. Gelderblom, and O. O. Versolato, *Laser-to-droplet alignment sensitivity relevant for laser-produced plasma sources of extreme ultraviolet light*, J. App. Phys. **124**, 013102 (2018).

[93]F. Torretti, F. Liu, M. Bayraktar, J. Scheers, Z. Bouza, W Ubachs, R Hoekstra, and O. Versolato, *Spectral characterization of an industrial EUV light source for nanolithography*, J. Phys. D Appl. Phys. **53**, 055204 (2019).

[94]D. J. Hemminga, L. Poirier, M. Basko, R. Hoekstra, W. Ubachs, O. O. Versolato, and J. Sheil, *High-energy ions from Nd:YAG laser ablation of tin microdroplets: comparison between experiment and a single-fluid hydrodynamic model*, Plasma Sources Sci. Technol. **30**, 105006 (2021).

[95]Y. Sakai and I. Katsumata, *An energy resolution formula of a three plane grids retarding field energy analyzer*, Jpn. J. Appl. Phys. **24**, 337–341 (1985).

[96]O. O. Versolato, J. Sheil, S. Witte, W. Ubachs, and R. Hoekstra, *Microdroplet-tin plasma sources of EUV radiation driven by solid-state-lasers (topical review)*, J. Opt. **24**, 054014 (2022).

[97]Y. Kawasuji, K. M. Nowak, T. Hori, T. Okamoto, H. Tanaka, Y. Watanabe, T. Abe, T. Kodama, Y. Shiraishi, H. Nakarai, et al., *Key components technology update of the 250w high-power lpp-euv light source*, in Spie advanced lithography, Vol. 10143 (International Society for Optics and Photonics, 2017), 101432G–101432G.

[98]M. Murakami and M. M. Basko, *Self-similar expansion of finite-size non-quasi-neutral plasmas into vacuum: relation to the problem of ion acceleration*, Phys. Plasmas **12**, 012105 (2006).

[99]A. V. Gurevich, L. V. Pariĭskaya, and L. P. Pitaevskiĭ, *Self-similar Motion of Rarefied Plasma*, J. Exp. Theor. Phys. **22**, 449 (1966).

[100]M. Brandstätter, N. Gambino, and R. S. Abhari, *Temporally and spatially resolved ion dynamics of droplet-based laser-produced tin plasmas in lateral expansion direction*, J. Appl. Phys. **123**, 043308 (2018).

[101]N. Gambino, M. Brandstätter, B. Rollinger, and R. Abhari, *A hemispherical langmuir probe array detector for angular resolved measurements on droplet-based laser-produced plasmas*, Rev. Sci. Instrum. **85**, 093302 (2014).

[102]O. Morris, P. Hayden, P. Dunne, F. O'Reilly, G. O'Sullivan, E. L. Antonsen, S. N. Srivastava, K. C. Thompson, and D. N. Ruzic, *Determination of charge state, energy and angular distributions of tin ions emitted from laser produced plasma based EUV sources*, J. Phys. Conf. Ser. **58**, 391–394 (2007).

[103]J. C. S. Kools, T. S. Baller, S. T. De Zwart, and J. Dieleman, *Gas flow dynamics in laser ablation deposition*, J. Appl. Phys. **71**, 4547–4556 (1992).

[104]Q. Qin, M. Zhou, and D. Mao, *Time-of-flight mass spectrometric study on UV laser ablation of silver chloride*, Applied Surface Science **119**, 321–329 (1997).

[105]R. Kelly and R. Dreyfus, *Reconsidering the mechanisms of laser sputtering with Knudsen-layer formation taken into account*, Nucl. Instrum. Methods Phys. Res. B: Beam Interact. Mater. At. **32**, 341–348 (1988).

[106]P. Hess, R. Bailey, A. Boccara, and G. Physikzentrum (Bad Honnef, *Photoacoustic, Photothermal, and Photochemical Processes at Surfaces and in Thin Films*, Topics in current physics (Springer-Verlag, 1989).

[107]Z. Chen, X. Wang, D. Zuo, and J. Wang, *Investigation of ion characteristics in CO_2 laser irradiating predeformed tin-droplet plasma*, Laser Part. Beams **34**, 552–561 (2016).

[108]A. O'Connor, O. Morris, and E. Sokell, *Angular and energy distribution of Sn ion debris ejected from a laser-produced plasma source, for laser power densities in the range suitable for extreme ultraviolet lithography*, J. Appl. Phys. **109**, 073301–073301 (2011).

[109]L. Poirier, A. Lassise, Y. Mostafa, L. Behnke, N. Braaksma, L. Assink, O. Versolato, and R. Hoekstra, *Energy- and charge-state-resolved spectrometry of tin-laser-produced plasma using a retarding field analyzer*, Appl. Phys. B **128**, 135 (2022).

[110]L. Assink and *et al*, *In preparation*,

[111]J. Hernandez-Rueda, B. Liu, D. J. Hemminga, Y. Mostafa, R. A. Meijer, D. Kurilovich, M. Basko, H. Gelderblom, J. Sheil, and O. O. Versolato, *Early-time hydrodynamic response of a tin droplet driven by laser-produced plasma*, Phys. Rev. Research **4**, 013142 (2022).

[112]M. M. Basko and I. P. Tsygvintsev, *A hybrid model of laser energy deposition for multi-dimensional simulations of plasmas and metals*, Comput. Phys. Commun. **214**, 59–70 (2017).

[113]R. A. Meijer, D. Kurilovich, K. S. E. Eikema, O. O. Versolato, and S. Witte, *The transition from short- to long-timescale pre-pulses: laser-pulse impact on tin microdroplets*, J. Appl. Phys. **131**, 105905 (2022).

[114]L. Poirier, D. J. Hemminga, A. Lassise, L. Assink, O. O. Versolato, and R. Hoekstra, *Strongly anisotropic ion emission in the expansion of Nd:YAG-laser-produced plasma*, Phys. Plasmas **29**, 123102 (2022).

[115]R. Schupp, L. Behnke, Z. Bouza, Z. Mazzotta, Y. Mostafa, A. Lassise, L. Poirier, J. Sheil, M. Bayraktar, W. Ubachs, R. Hoekstra, and O. O. Versolato, *Characterization of angularly resolved EUV emission from 2-μm-wavelength laser-driven Sn plasmas using preformed liquid disk targets*, Journal of Physics D: Applied Physics **54**, 365103 (2021).

[116]I. Roudskoy, *General features of highly charged ion generation in laser-produced plasmas*, Laser and Particle Beams **14**, 369–384 (1996).

[117]T. E. Sharp, *Potential-energy curves for molecular hydrogen and its ions*, At. Data Nucl. Data Tables **2**, 119–169 (1971).

[118]M. Wacks, *Franck-Condon factors for ionization of H_2, HD and D_2*, J. Res. Natl. Bur. Stand. A Phys. Chem. **68**, 631 (1964).

[119]A. Kramida, Y. Ralchenko, J. Reader, and and NIST ASD Team, NIST Atomic Spectra Database (ver. 5.3), [Online]. [2016, February 2]. National Institute of Standards and Technology, Gaithersburg, MD. 2015.

[120]R. Kersevan and M. Ady, *Recent developments of Monte-Carlo codes MolFlow+ and SynRad+*, in Proc. 10th Int. Particle Accelerator Conf. (IPAC'19), Melbourne, Australia (2019).

[121]S. Rai, K. I. Bijlsma, I. Rabadán, L. Méndez, P. A. J. Wolff, M. Salverda, O. O. Versolato, and R. Hoekstra, *Charge exchange in collisions of 1–100-keV Sn^{3+} ions with H_2 and D_2*, Phys. Rev. A **106**, 012804 (2022).

[122]R. Mann, F. Folkmann, and H. F. Beyer, *Selective electron capture into highly stripped Ne and N target atoms after heavy-ion impact*, J. Phys. B: At. Mol. Phys. **14**, 1161 (1981).

[123]H. Ryufuku, K. Sasaki, and T. Watanabe, *Oscillatory behavior of charge transfer cross sections as a function of the charge of projectiles in low-energy collisions*, Phys. Rev. A **21**, 745 (1980).

[124]N. A, *A classical model for multiple-electron capture in slow collisions of highly charged ions with atoms*, J. Phys. B: At. Mol. Phys., 2925–2937 (1986).

[125]M. Imai, Y. Iriki, and A. Itoh, *Target Dependence of Single-Electron-Capture Cross Sections for Slow Be, B, C, Fe, Ni, and W Ions Colliding with Atomic and Molecular Targets*, Fusion. Sci. Tech. **63**, 392 (2013).

[126]R. Lomsadze, M. Gochitashvili, and R. Kezerashvili, *Inelastic processes in Na^+-Ne, Na^+-Ar, Ne^+-Na, and Ar^+-Na collisions in the energy range 0.5-14 keV*, Phys. Rev. A.. **92**, 062703 (2015).

[127]R. E. Olson and A. Salop, *Kimura ions and neutral species*, Phys. Rev. A **14**, 579 (1976).

[128]M. Kimura, T. Iwai, Y. Kaneko, N. Kobayashi, A. Matsumoto, S. Ohtani, K. Okuno, S. Takagi, H. Tawara, and S. Tsurubuchi, *Landau-Zener model calculations of one-electron capture from He atoms by highly stripped ions at low energies*, J. Phys. Soc. Jpn. **53**, 2224 (1984).

[129]I. I. Sobelman, *Atomic spectra and radiative transitions* (Springer-Verlag, Berlin Heidelberg New York, 1979).

[130]M. F. Gu, *The flexible atomic code*, Can. J. Phys. **86**, 675–689 (2008).

[131]K. Haris and A. Tauheed, *Revised and extended analysis of doubly ionized tin: Sn III*, Phys. Scr. **85**, 055301 (2012).

[132]L. J. Curtis, R. Matulioniene, G. Ellis, and C. Froese Fischer, *Predictive data-based exposition of* $5s5p\ ^{1,3}P_1$ *lifetimes in the Cd isoelectronic sequence*, Phys. Rev. A **62**, 052513 (2000).

[133]C. Colón and A. Alonso-Medina, *Calculation of oscillator strengths, transition probabilities and radiative lifetimes of levels in Sn III*, J. Phys. B: At. Mol. Opt. Phys. **43**, 165001 (2010).

[134]J. A. Kernahan, E. H. Pinnington, W. Ansbacher, and J. L. Bahr, *Experimental mean lives for levels in Sn III and Sn IV*, Nucl. Instr. Meth. Phys. Res. B **9**, 616 (1985).

[135]R. K. Janev and H. Winter, *State-selective electron capture in atom-highly charged ion collisions*, Phys. Rep. **117**, 265 (1985).

list of publications

CHAPTER 1

L. Poirier, A. Bayerle, A. Lassise, F. Torretti, R. Schupp, L. Behnke, Y. Mostafa, W. Ubachs, O. O. Versolato, and R. Hoekstra, *Absolute cross-calibration of a combined electrostatic and time-of-flight analyzer for energy- and charge-state-resolved spectrometry of tin laser-produced plasma*, App. Phys. B **128** (2022).

CHAPTER 2

D. J. Hemminga, L. Poirier, M. Basko, W. Ubachs, R. Hoekstra, O. O. Versolato, and J. Sheil, *High-energy ions from Nd:YAG laser ablation of tin microdroplets: Comparison between experiment and a single-fluid hydrodynamic model*, Plasma Sci. Technol. **30** (2021).

CHAPTER 3

L. Poirier, A. Lassise, Y. Mostafa, L. Behnke, N. Braaksma, L. Assink, R. Hoekstra, and O. O. Versolato, *Energy- and charge-state-resolved spectrometry of tin laser-produced plasma using a retarding field energy analyzer*, App. Phys. B **128** (2022).

CHAPTER 4

L. Poirier, D. J. Hemminga, A. Lassise, L. Assink, R. Hoekstra, J. Sheil, and O. O. Versolato, *Strongly anisotropic ion emission in the expansion of Nd:YAG-laser-produced plasma*, Phys. Plasmas **29** (2022).

CHAPTER 5

L. Poirier, A. Lassise, R. Hoekstra, J. Sheil, and O. O. Versolato, *Dependence of ion charge-energy emission from Nd:YAG-laser-produced tin plasma as function of laser intensity in the* $0.4 - 40 \times 10^{10}$ *W/cm*^{2} *range*, Phys. Plasmas **30** (2023) .

CHAPTER 6

S. Rai, K. I. Bijlsma, L. Poirier, E. de Wit, L. Assink, A. Lassise, I. Rabadán, L. Méndez, J. Sheil, O. O. Versolato and R. Hoekstra, *Evidence of production of keV* Sn^+ *ions in the* H_2 *buffer gas surrounding an Sn-plasma EUV source*, Plasma Sci. Technol. **32** (2023).

The author has also contributed to the following publication:

R. Schupp, L. Benhke, Z. Bouza, Z. Mazzotta, Y. Mostafa, A. Lassise, L. Poirier, J. Sheil, M. Bayraktar and W. Ubachs, *Characterization of angularly resolved EUV emission from 2-µm-wavelength laser-driven Sn plasmas using preformed liquid disk targets*, J. Phys. D **54** (2021).

acknowledgements

A little more than fifteen hundred days after its inception, it is time for my doctoral odyssey to come to a close. I ought to acknowledge those who contributed to making the four year-long journey a fruitful and a pleasant one.

Oscar, I am proud to have been part of your research team. You provided me with more than enough drive and guidance throughout my PhD, and in the end it has been a pleasure being under your supervision. Thank you for giving me the opportunity to depart on the journey, and for trusting my clumsy hands along the way. Your availability and straightforward communication style are things I came to appreciate and am grateful for. Same goes for your sense of humor, although some of our jokes -reciprocally- got lost in translation and crash-landed somewhere between France and the Netherlands. To you and to your research group, I wish nothing but success.

Ronnie, Groningen lies are far away but your train rides and our zoom calls helped bridge the gap, granting me access your precious expertise on ion interactions. Although the campaign to calibrate the Thomson parabola concluded in a flop, my experience working with your group (and with the antediluvian ion beamline at the Zernike Institute) and my trips up North are dear to my memory. Of all whom reviewed the papers we put together, you were perhaps the most scrupulous one: thanks to you I now leave with a sharper scientific eye.

John, it has been a pleasure to work at your side during the last few years, both as a postdoc and a group leader. Many great experiences, many learnings and many laughs were had along the way, most of which you were involved in. I wish you the best for your career,

though it seems like nothing will stop you from thriving in academia. Godspeed! Let 2023 be the year when we return to Saariselkä to feel alive once again.

Wim U., although the path I took did not lead me to precision spectroscopy, I did find my way into the group thanks to you; for this, for your scientific insight and for your cheerful demeanor I am grateful for.

Laurent, un grand merci de m'avoir aidé à trouver un groupe de recherche où accomplir ma thèse (même si elle ne porte finalement pas sur la spectroscopie de pointe, il est vrai).

To the members of the EUV plasma processes group and to my peers over in Groningen, thank you all for making the experience a fun and a pleasant one. From the snowboarding masterclass in Westerpark, the bowling prowess of "person #6" at AMO Egmond, the long-winded sessions at Foeders on an empty (or peanut-filled) stomach, the drunken late nights in Veldhoven, to the paddling and swimming the Groningen canals... oh, and the beautiful physics as well... so many great memories I will forever cherish. To Ruben, Joris, Alex, Randy, Adam, Bo, Subam, Lars B., Diko, Zoi, Yahia, Javi, Klaas, Mart, Karl, Luc, Dion, Jane, Stan, Jorge, Mikheil, Edcel, Youssef, Hugo and to Irish Kevin — to Mardou, Sander, Bowie, Sjoukje, Emiel, Robbert, Boris, and to all interns who worked at our side, thank you all for the great atmosphere, for the help, the smiles, and the laughs. I will miss you all in my next life chapter. In the meantime I wish you all the best and look forward to see you at the defence.

Laurens, thank you for being so resourceful and patient with me. I like to say that I make all possible mistakes once so I can avoid them the next time; hopefully you did not lose too much of your time on fixing said mistakes. Best of luck for the TPS calibration!

To the "ion team" postdocs, Alex and Adam: together we conducted beautiful research projects which we can be proud of. Fortunately for me, you were more interested in roaming the dark corners of the labs than to claim first-authorship on the manuscripts we wrote; that certainly made it easier for me in the long run. Thank you both very much for the hard work, the patience and the good company!

To my paranymphs Yahia and Luc who will be by my side for the final stretch before my promotion, a heartfelt thank you for helping me setting things up and taking weight off of my back in the process. Lars B., we were born of the same PhD student litter and you were my #1, but California is calling out for you and I should not stand in your way. I wish you all the best for your new life in the US of A.

Wim vd Z., I first met you early in my PhD as the ASML liaison we should try to impress, but got to know you better as a director of ARCNL. After almost a year under your rule, I have to praise you for your proximity to ARCNL employees which make us feel appreciated. Thank you for the interest you express toward our research and for your hearty attitude.

Marjan, thank you for making sure that ARCNL employees can experience both good working conditions and a good social atmosphere. Thank you also for helping organize great seasonal events at ARCNL.

A big thank you to the past and present members of the secretariat, for being helpful and for bearing with my reluctance to do things on time. All the best for you, be it at ARCNL or far beyond its gates.

An equally big thank you to the support staff without which none of the research presented in this thesis could have been brought to fruition. Jorijn, Duncan, Pepijn, Ilya and Henk-Jan: your contribution transpires from each chapter of this thesis, and I cannot thank you enough for it.

Reinout, I am taking good care of the *compostwormen* you trusted me with, and through them my memory of you lives on.

Over the years, ARCNL grew into a home to me, with all its familiar faces, legends and traditions. Thank you to all the good people without whom the academic experience would surely be stale and lifeless. I will miss you all as well as the great liveliness of the institute. Thank you to past and present members of the PV whom — through blood, sweat and tears — contributed greatly to this liveliness. Besides, long live the ARCNL band, the healthy wrap lunch club and the bouldering crew; I do hope to somehow remain involved with these formidable ventures in my post-ARCNL life.

I am also grateful to the members of the late Optoelectronics research group of the University of Amsterdam, with whom I discovered Amsterdam and academic research as a whole. Chris, Marco, Leyre, Arnon, Yingying, Bart, Elinore and the rest of the TGG crew: I wish you the very best!

Tom, my Dutch journey started under your wing as a member Optoelectronics research group at the University of Amsterdam. I had a great time under your wing, and I will always admire your scientific intuition and ever-lasting liveliness. You made me feel cared for, you and your wife were generous to me and you made it easier to call Amsterdam my home. May you rest in peace.

Maaike, vier jaar geleden hoopte ik dat ik nu vloeiend Nederlands zou spreken. De reis naar dit doel is nog niet voorbij, maar de ervaring was gezellig; dankjewel voor jouw geweldige lessen en voor jouw eeuwige glimlach!

Léa and Lars L., my favourite ducklings with whom the COVID lockdown became easier to go through, I keep many great memories of our time together. Swimming in the canals, sharing drinks late in the evening, discussing L2-type regression schemes, and waking up late in the tiny house sofa to the smell of coffee and spirulina-based energy balls... I am looking forward to visiting you again in Jena.

À mes amis du pays natal, de Maisons-Alfort, de la Fac et d'ailleurs: du boulot on ne parle pas des masses, et c'est sûrement mieux ainsi. C'est aussi un peu grâce à ça que j'ai pu

garder la tête hors de l'eau pendant ces quatre dernières années. J'aurais aimé pouvoir passer plus de temps à vos côtés, et même si je prétends que "j'aime plus Paris", je suis toujours un peu chagrin quand je prends le bus retour pour mon plat pays. Dans mon cœur et sur mon canapé-lit, il y a pour chacun de vous une place de choix!

Lucie, tu as été et restes, comme l'a chanté Brassens "[ma] compagne de voyage, dont les yeux, charmant paysage, font paraître court le chemin". Mon chemin de thèse, si j'avais à le faire à nouveau, ce serait derechef à tes côtés. Quant à toi, je te vois aujourd'hui épanouie dans ta carrière post-doctorale; j'espère pouvoir partager ce bonheur avec toi très bientôt. Merci pour ton soutien, ta tendresse et pour notre grande complicité.

Maman, Papa, Gabriel, ça a toujours été un plaisir de rentrer en France passer des (trop brefs) week-ends ou des vacances avec vous. Promis, un jour je m'offrirai le Thalys pour de bon et je rentrerai plus souvent ! Mille mercis pour l'intérêt que vous avez porté pour ma thèse et pour votre soutien inconditionnel.

Mes grands-parents, vous qui m'avez transmis l'amour de la Science, de l'Histoire, de la cuisine, de la montagne et de la lecture (Sand, Giono et Genevois — mes fidèles compagnons de lecture dans l'Oosterpark), je vous dédie ma thèse.